

**Characterizing Ash and Substrate Properties in Sintered Metal Fiber  
Diesel Particulate Filters Using an Advanced Diagnostic Approach**

by

Paul Folino

B.S., Naval Architecture & Marine Engineering  
United States Coast Guard Academy, 2010

Submitted to the Department of Mechanical Engineering in Partial Fulfillment of the  
Requirements for the Degrees of

MASTER OF SCIENCE IN MECHANICAL ENGINEERING

AND

MASTER OF SCIENCE IN NAVAL ARCHITECTURE & MARINE ENGINEERING

AT THE

MASSACHUSETTS INSTITUTE OF TECHNOLOGY

June 2015

© 2015 Massachusetts Institute of Technology  
All rights reserved.



**Signature redacted**

Signature of Author: \_\_\_\_\_

Department of Mechanical Engineering  
May 8, 2015

**Signature redacted**

Certified by: \_\_\_\_\_

Principal Research Scientist and Lecturer in Mechanical Engineering  
Thesis Supervisor  
Victor W. Wong

**Signature redacted**

Accepted by: \_\_\_\_\_

David Hardt  
Chairman, Department Committee on Graduate Students

(This page intentionally left blank)

# **Characterizing Ash and Substrate Properties in Sintered Metal Fiber Diesel Particulate Filters Using an Advanced Diagnostic Approach**

by

Paul Folino

Submitted to the Department of Mechanical Engineering on May 8, 2015 in Partial Fulfillment of the Requirements for the Degree of

MASTER OF SCIENCE IN MECHANICAL ENGINEERING

AND

MASTER OF SCIENCE IN NAVAL ARCHITECTURE & MARINE ENGINEERING

## **ABSTRACT**

In order to comply with strict air emissions regulations, applicable diesel engines are required to have an installed after-treatment device. A diesel particulate filter (DPF) is one of these after-treatment devices, and it is used to capture hazardous particulate matter (PM) from the engine exhaust stream. Over the lifetime of the DPF, incombustible materials like ash are deposited within the DPF. The presence of ash inhibits the exhaust flow and thus causes flow restriction throughout the filter. This increase in the flow restriction due to ash accumulation has an adverse effect on engine performance, primarily a reduction in fuel economy.

While the global effects of ash on engine performance are well researched and understood, the fundamental mechanisms of ash phenomenology in the DPF require further understanding. Current experimental data mainly addresses how ash porosity and permeability influence pressure drop across the filter, but an investigation of these properties reveals how other key sub-parameters, such as ash particle size and distribution and filter oxidation level, significantly contribute to an increase in pressure drop as well.

The focus of this work is to understand the behavior of ash particles in a sintered metal fiber (SMF) filter substrate and recognize the resultant effect on DPF pressure drop using an advanced diagnostic approach. Much of the work relies on the use of sophisticated imaging and software tools to quantify properties such as particle size, particle distribution, filter porosity, and permeability among others. Additionally, this research introduces and demonstrates the capabilities of these cutting-edge tools and how they can best be utilized to provide filter performance data to qualify existing and future experimental data for SMF or cordierite filters. An analysis of the data reveals a statistically significant dependence between pressure drop and the aforementioned sub-parameters.

Thesis Supervisor: Victor W. Wong  
Title: Principal Research Scientist and Lecturer in Mechanical Engineering

**(This page intentionally left blank)**

# ACKNOWLEDGMENTS

Attending MIT has been a very memorable experience that undoubtedly would not have happened had it not been for all of those who supported me in this endeavor. My past two years have been challenging, yet rewarding, and I owe an immense debt of gratitude to the faculty and students I have met for their devotion to teaching and researching.

I would first like to thank my thesis advisor, Dr. Victor Wong, for providing me with the opportunity to conduct research on an interesting topic. Aside from giving me latitude in researching where my interests were, Dr. Wong served as a great mentor, always challenging me intellectually and teaching me how to conduct research. I can confidently say that I have a more coherent and methodical approach to problem solving, and I am eternally grateful for that.

My research project would not have been possible without the generous support of the MIT Consortium to Optimize Lubricant and Diesel Engines for Robust Emission Aftertreatment Systems. I would like to thank all the members for financial support as well as professional and academic encouragement; the candid discussions occurring at the consortium meetings every few months were critical to completing my research. A very special thanks goes to the staff at Rypos for their technical expertise in sintered metal fiber DPFs.

Also, I would like to thank Dr. Carl Justin Kamp for his support on this project. Dr. Kamp's vast knowledge of advanced diagnostic techniques was an invaluable resource to have. I am fortunate to have worked with someone with such intellectual curiosity, and I appreciate all the late nights he worked to bolster the research effort.

A great deal of gratitude is in order for the faculty and staff at the Center for Materials Science and Engineering (CMSE), especially Patrick Boisvert and Dr. Chen. Also Dr. Kosar, Monica Zugravu, and Greg Lin at Harvard's Center for Nanoscale Systems, deserve much appreciation.

Next I want to thank my lab mates, James Jorgensen, Tim Murray, Nick Custer, Greg Monahan, and Michael Arnold, for their endless support and guidance. Without question, some of the most valuable insight I received on my project stemmed from the various impromptu conversations we shared in the office. It has been a true pleasure working with such a dedicated group, and I am thankful for the opportunity.

Also, I would like to thank CAPT Thomas, CAPT Harbour, CDR Gray, CDR Ketcham, and my classmates of the 2N program, as well as the US Coast Guard for allowing me to pursue graduate studies in engineering.

I would like to thank the rest of the Sloan Automotive Laboratory personnel including Janet Maslow, Thane Dewitt, Dr. Sappok, Dr. Wang, and all of the graduate students. Without them, the lab simply would not run, and I deeply appreciate their dedication to facilitating research.

Finally, I would like to thank my loving family for always being my biggest fan. Had it not been for their unconditional love and support, I never would have dreamed of being given the opportunity to attend MIT.

(This page intentionally left blank)

# TABLE OF CONTENTS

ABSTRACT.....	3
ACKNOWLEDGMENTS .....	5
LIST OF FIGURES .....	9
LIST OF TABLES.....	11
NOMENCLATURE .....	13
1 INTRODUCTION .....	17
1.1 Diesel Engine Fundamentals.....	18
1.2 Diesel Engine Advantages .....	20
1.3 Diesel Engine Applications.....	22
1.4 Diesel Engine Disadvantages.....	23
1.5 Diesel Emissions Regulations.....	26
1.6 After-treatment Devices.....	29
2 DIESEL PARTICULATE FILTERS.....	35
2.1 Wall-Flow Monolith Characteristics.....	36
2.1.1 Soot and Ash Accumulation in Wall-Flow Monolith DPFs .....	37
2.1.2 Backpressure and Fuel Economy .....	38
2.1.3 Governing Equations .....	40
2.2 SMF DPF Characteristics .....	41
2.2.1 Soot and Ash Accumulation in SMF DPFs .....	44
2.2.2 SMF DPF Governing Equations .....	45
3 ADVANCED DIAGNOSTIC APPROACH .....	47
3.1 Scanning Electron Microscopy (SEM) .....	48
3.2 ESEM Image Processing.....	51
3.3 Energy Dispersive X-Ray Spectroscopy (EDX).....	52
3.4 X-Ray Fluorescence (XRF) .....	57
3.5 Focused Ion Beam (FIB).....	58
3.6 X-Ray Computed Tomography (X-Ray CT).....	59
3.7 X-Ray Post-Processing .....	62
4 EXPERIMENTAL PROCEDURES .....	65
4.1 Sample History.....	65

4.2	Experimental Methodology .....	66
4.2.1	Fiber Diameter Determination .....	66
4.2.2	Surface Composition of Fibers .....	67
4.2.3	Porosity and Ash Bridging in SMF Pores.....	68
4.2.4	Ash Particle Size and Agglomerate Structure.....	70
4.2.5	Spatial Distribution of Ash .....	72
4.3	Statistical Procedures .....	73
4.3.1	Statistical Techniques .....	73
4.3.2	Parameter Screening .....	75
5	RESULTS AND ANALYSIS.....	77
5.1	Fiber Diameter Determination Results .....	77
5.2	Surface Composition of Fibers Results.....	81
5.3	Ash Particle Size and Agglomerate Structure Results.....	85
5.4	Spatial Distribution of Ash Results .....	92
5.5	Porosity and Ash Bridging in SMF Pores Results .....	94
5.6	Statistical Analysis Results.....	96
6	CONCLUSIONS AND RECOMMENDATIONS .....	101
6.1	Advanced Diagnostic Methods.....	101
6.2	Summary of Results.....	103
6.3	Recommendations.....	107
7	REFERENCES .....	109

# LIST OF FIGURES

<b>Figure 1.1.</b> 4-Stroke Engine Operating Cycle and Pressure vs. Crank Angle Plot.....	18
<b>Figure 1.2.</b> 2-Stroke Engine Scavenging Arrangements.....	19
<b>Figure 1.3.</b> Breakdown of Constituent PM Fractions .....	25
<b>Figure 1.4.</b> Reductions of PM and NO <sub>x</sub> in Heavy-Duty Diesel Engines.....	28
<b>Figure 1.5.</b> Reductions of PM and NO <sub>x</sub> in Nonroad Diesel Engines .....	29
<b>Figure 1.6.</b> Increase in TPM Due to High Sulfur Fuel .....	31
<b>Figure 1.7.</b> Common Arrangement of Diesel After-treatment Devices .....	32
<b>Figure 2.1.</b> Wall-flow Monolith Structure .....	36
<b>Figure 2.2.</b> Effect of Soot and Ash Loading on Pressure Drop Across the DPF .....	38
<b>Figure 2.3.</b> Ash and Soot Transport Mechanism in Wall-flow Monolith DPF .....	38
<b>Figure 2.4.</b> Effect of Exhaust Backpressure on Specific Fuel Consumption .....	39
<b>Figure 2.5.</b> Top View of Large Fibers and Cross Section View of SMF DPF .....	43
<b>Figure 2.6.</b> Complete SMF DPF Assembly .....	43
<b>Figure 2.7.</b> Ash Deposition Differences between Porous Ceramic DPFs and SMF DPFs .....	44
<b>Figure 3.1.</b> Fundamental Principles of SEM and ESEM Used at MIT’s CMSE .....	48
<b>Figure 3.2.</b> ESEM Image Quality Differences.....	50
<b>Figure 3.3.</b> Ash Particle Identification Process with ImageJ.....	52
<b>Figure 3.4.</b> Excitation Potential vs. Atomic Number and Atomic Orbital Shells .....	53
<b>Figure 3.5.</b> Image of SMF DPF Fibers and EDX Elemental Mapping Analysis.....	55
<b>Figure 3.6.</b> EDX Point Analysis and Resulting Spectrogram.....	56
<b>Figure 3.7.</b> XRF Output Spectrogram and Constituent Elements .....	58
<b>Figure 3.8.</b> Fundamental Principles of FIB and Milled Cross Section of SMF DPF .....	59
<b>Figure 3.9.</b> Fundamental Principles of X-Ray CT and Harvard’s MicroCT .....	60
<b>Figure 3.10.</b> Reduction in X-Ray CT ROI and Resulting Reduction in File Size .....	61
<b>Figure 3.11.</b> Histogram Adjustment Effect on SMF DPF Porosity .....	62
<b>Figure 3.12.</b> VG Studio Max Output Porosity .....	62
<b>Figure 3.13.</b> Rendered CAD Mesh of SMF DPF Sample Scanned Using X-Ray CT.....	63
<b>Figure 4.1.</b> Wall Thickness Module and Histogram.....	67
<b>Figure 4.2.</b> Oxide Layer Detachment of Fiber.....	68
<b>Figure 4.3.</b> Pore Structure in Cordierite DPF vs. SMF DPF.....	69

<b>Figure 4.4.</b> Core samples of SMF DPF and Resultant Porosity .....	70
<b>Figure 4.5.</b> Despeckle Filter Working Principles .....	71
<b>Figure 4.6.</b> Determination of Extreme Outliers in Normal Quantile Plot.....	74
<b>Figure 5.1.</b> % Fiber Growth (ESEM) vs. Filter Depth Location .....	77
<b>Figure 5.2.</b> % Fiber Growth (Wall Thickness Module) vs. Filter Depth Location .....	79
<b>Figure 5.3.</b> % Al vs. Filter Depth Location .....	81
<b>Figure 5.4.</b> % Ca vs. Filter Depth Location .....	83
<b>Figure 5.5.</b> % Zn vs. Filter Depth Location .....	84
<b>Figure 5.6.</b> Average Ash Particle Diameter vs. Filter Depth Location .....	86
<b>Figure 5.7.</b> % Na vs. Filter Depth Location .....	88
<b>Figure 5.8.</b> Number of Particles vs. Filter Depth Location .....	89
<b>Figure 5.9.</b> Average Agglomerate Area vs. Filter Depth Location .....	90
<b>Figure 5.10.</b> Number of Agglomerates vs. Filter Depth Location .....	91
<b>Figure 5.11.</b> XRF Counts of Ca vs. Filter Depth Location .....	92
<b>Figure 5.12.</b> XRF Counts of Zn vs. Filter Depth Location .....	93
<b>Figure 5.13.</b> Porosity vs. Filter Depth Location .....	95
<b>Figure 5.14.</b> P-values for Regression Variables .....	97
<b>Figure 5.15.</b> Adjusted P-values after removing % Ca .....	98
<b>Figure 5.16.</b> Summary of Fit and ANOVA of Statistical Model .....	99

# LIST OF TABLES

<b>Table 1.1.</b> Range of Particle Sizes Classified as PM .....	26
<b>Table 1.2.</b> Diesel After-treatment Devices and Respective Emission Reductions .....	30
<b>Table 2.1.</b> Material Differences Between Cordierite and SiC DPF Substrates .....	37
<b>Table 3.1.</b> Experimental Settings Used for ESEM and EDX.....	49
<b>Table 4.1.</b> Compilation of Ash Particle Sizes from Various Sources .....	72
<b>Table 5.1.</b> Response and Regressor Variables for Statistical Analysis .....	96

(This page intentionally left blank)

# NOMENCLATURE

.IGES	Initial Graphics Exchange Specification
.STEP	Standard for the Exchange of Product Model Data
.STL	Stereolithography
AFR	Air to Fuel Ratio
Ag	Silver
Al	Aluminum
ANOVA	Analysis of Variance
BDC	Bottom Dead Center
BSE	Backscatter Electrons
BSFC	Brake Specific Fuel Consumption
Ca	Calcium
CAD	Computer Aided Design
CARB	California Air Resources Board
CFD	Computational Fluid Dynamics
CFR	Code of Federal Regulations
CH <sub>4</sub>	Methane
CI	Compression Ignition
CMSE	Center for Materials Science and Engineering
CNS	Center for Nanoscale Systems
CO	Carbon Monoxide
CO(NH <sub>2</sub> ) <sub>2</sub>	Urea
CO <sub>2</sub>	Carbon Dioxide
CPSI	Cells Per Square Inch
DOC	Diesel Oxidation Catalyst
DPF	Diesel Particulate Filter
EDX	Energy Dispersive X-Ray Spectroscopy
EPA	Environmental Protection Agency
ESEM	Environmental Scanning Electron Microscope
EU	European Union
FCP	Fuel Consumption Penalty
Fe	Iron
FIB	Focused Ion Beam
FR	Federal Register
FTP	Transient Federal Test Procedure
Ga <sup>+</sup>	Gallium Ion
GB	Gigabyte
GVWR	Gross Vehicle Weight Rating
H <sub>2</sub> O	Water
H <sub>2</sub> SO <sub>4</sub>	Sulfuric Acid
HC	Hydrocarbons
HEPA	High-Efficiency Particulate Air
IC	Internal Combustion
Mg	Magnesium

MIT	Massachusetts Institute of Technology
MSHA	Mine Safety and Health Administration
N <sub>2</sub>	Nitrogen (Gaseous)
NH <sub>3</sub>	Ammonia
NO	Nitric Oxide
NO <sub>2</sub>	Nitrogen Dioxide
NO <sub>x</sub>	Nitrogen Oxides
NPRM	Notice of Proposed Rulemaking
NRTC	Nonroad Transient Cycle
O <sub>2</sub>	Oxygen (Gaseous)
OEM	Original Equipment Manufacturer
PAH	Polynuclear Aromatic Hydrocarbons
PM	Particulate Matter
Pt	Platinum
ROI	Region of Interest
SCR	Selective Catalytic Reduction
SE	Secondary Electrons
SEM	Scanning Electron Microscopy
SI	Spark Ignition
SiC	Silicon Carbide
SMF	Sintered Metal Fiber
SO <sub>3</sub>	Sulfur Trioxide
SOF	Solid Organic Fraction
TDC	Top Dead Center
Ti	Titanium
TIFF	Tagged Image File Format
TPM	Total Particulate Matter
UFP	Ultrafine Particles
USC	United States Code
USDA	United States Department of Agriculture
VOC	Volatile Organic Compound
WDS	Wavelength Dispersive X-Ray Spectroscopy
X-Ray CT	X-Ray Computed Tomography
XRF	X-Ray Fluorescence
Zn	Zinc
μCT	MicroCT
$\vec{u}, u$	Velocity vector
$\Delta$	Laplace operator
$\nabla$	Del operator
$a$	Fiber diameter
$d_p$	Pore diameter
$g$	Gravitational constant
H <sub>0</sub>	Null hypothesis
H <sub>1</sub>	Alternative hypothesis

K	Permeability
L	Characteristic length
n	Sample size
P	Pressure
Prob >  t	P-value
Q <sub>IN</sub>	Heat in
Q <sub>OUT</sub>	Heat out
r <sub>C</sub>	Compression ratio
Re	Reynolds Number
t	Time variable
V <sub>C</sub>	Clearance volume
V <sub>d</sub>	Swept volume
w	Wall thickness
α	Significance level
β <sub>k</sub>	Partial regression coefficient (k <sup>th</sup> variable)
ΔP	Pressure drop
ε, φ	Porosity
η <sub>TH</sub>	Thermal efficiency
η <sub>V</sub>	Volumetric efficiency
μ	Dynamic Viscosity
ν	Kinematic Viscosity
ρ	Density

(This page intentionally left blank)

# 1 INTRODUCTION

The diesel engine is a reciprocating internal combustion (IC) engine that creates mechanical power as a result of the chemical reaction between air and liquid fuel at high temperatures. Due to its high-energy efficiency, durability, and low flash point of fuel, the diesel engine has been broadly implemented in many present-day industries including the transportation, agricultural, and mining sectors, among others [1]. One of the primary drawbacks with the diesel engine is that it emits a large amount of particulate matter (PM) due to the incomplete combustion of hydrocarbons (HC) in its fuel. This PM consists of small, micron-sized particles that are easily inhaled by humans and are known to cause adverse health conditions such as cancer and emphysema.

To control these PM emissions, regulations exist that require the use of an after-treatment device on certain diesel engines. One of the most widely used after-treatment devices is the diesel particulate filter (DPF), and its popularity is due to its 85-95% reduction of PM in the exhaust stream [2]. DPFs are typically made out of a porous ceramic material like cordierite, but advances in filtration technology have introduced other substrate materials such as sintered metal fiber (SMF) filters. Regardless of the substrate material, incombustibles, such as lubricant-derived ash and other ash-like materials get trapped in the DPF, and can negatively impact the performance and fuel economy of the engine.

It is only through detailed, microscopic studies that we can begin to understand why and how ash collects in SMF DPFs. There are many advanced diagnostic tools that enable the study of ash deposition mechanisms in the DPF; the use of these tools is not new to ash research in DPFs. However, there is little to no documentation for researchers to utilize which outlines the best practices in analyzing both ash and substrate properties in SMF DPFs. There are two motivations behind this study: (1) to research current and innovative methods used in analyzing DPFs, in order to determine a standard methodology for accurately characterizing ash and substrate properties in SMF DPFs, and (2) to see how ash and substrate properties collected using this standard methodology affect filter performance in SMF DPFs.

## 1.1 Diesel Engine Fundamentals

Rudolf Diesel's namesake engine, patented in 1892, introduced a novel alternative to the spark-ignition (SI) internal combustion engine [3]. Instead of relying on a spark to manually ignite the fuel-air mixture in the cylinder, the diesel engine, or compression-ignition engine (CI), relies exclusively on the spontaneous combustion of heated air and atomized liquid fuel injected into the cylinder to drive a piston. A connecting rod then translates the cyclical motion of the piston into rotational motion via the crankshaft, which provides mechanical power.

This allows the diesel engine to produce about twice the mechanical work for the same amount of fuel as an SI engine [3]. Because diesel engines rely on the compression of cylinder air instead of the spark ignition of a fuel-air mixture, they are not susceptible to engine knock, or the premature auto-ignition of the fuel-air mixture, and consequently have higher compression ratios,  $r_c$ , than SI engines [3]. The compression ratio relates the maximum volume of the cylinder to the clearance volume,  $V_c$ , or volume when the piston is at top-dead center (TDC), and is a good indicator of engine efficiency.

To understand how both CI and SI engines work requires understanding their different operating cycles, specifically the 4-stroke and 2-stroke cycle. The fundamentals of a 4-stroke diesel engine operation are depicted below in Figure 1.1.a. and 1.1.b.

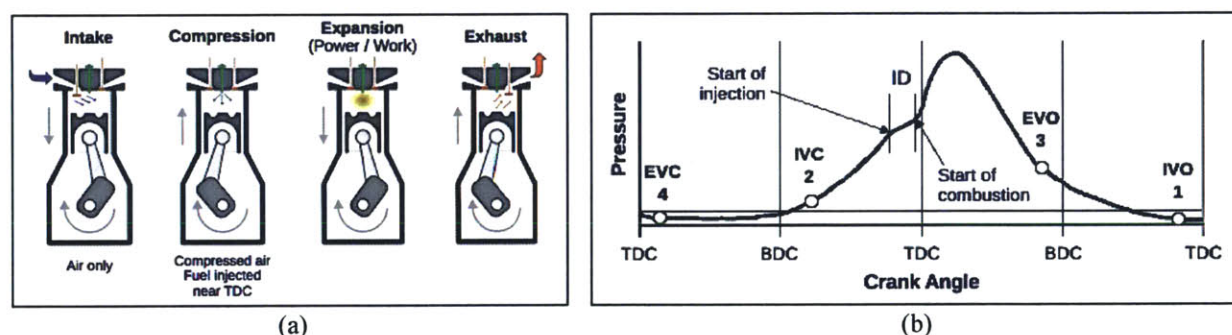


Figure 1.1. 4-stroke engine operating cycle, (a) and characteristic pressure vs. crank angle plot, (b) [4].

As shown in Figure 1.1.a., Step 1, the inlet valve is opened and air is fed into the cylinder during the intake stroke, causing the piston to move from top-dead center (TDC) to bottom-dead center (BDC), revealing the maximum cylinder volume, or swept volume,  $V_d$ . The inlet valve closes

(Figure 1.1.b., Step 2) and the piston compresses the air in the cylinder during the compression stroke, with fuel injection occurring toward the end of the stroke. There is a time delay between fuel injection and combustion, but when combustion occurs the pressure in the cylinder rises rapidly, which causes the gas to force the piston back down to BDC in the expansion or power stroke. Just before the piston approaches BDC in the expansion stroke, the exhaust valve is opened (Figure 1.1.b., Step 3) and the residual exhaust gases are ejected from the cylinder as the piston approaches TDC and starts another cycle [4]. This 4-stroke operating cycle is similar for SI engines; however, the method of fuel-air ignition is different.

The 4-stroke cycle requires 2 full crankshaft revolutions to translate the chemical energy of the fuel into mechanical power. Both SI and CI engines also can operate on a 2-stroke cycle, which consists of only a compression and power stroke that can accomplish the intake and exhaust functions by covering intake and exhaust ports at the correct time to allow for simultaneous compression-combustion and intake-exhaust through 1 crankshaft revolution. This feature allows 2-stroke engines to have more power strokes per revolution than 4-stroke engines and thus makes them more power dense [3]. Because 2-stroke engines have a higher power density, they are used in many applications where weight reduction is essential, such as large 2-stroke marine diesels in cargo ships. The main disadvantage of these engines is their proclivity for exhausting more unburned fuel than 4-stroke engines, causing more air pollution [5]. As can be seen in Figure 1.2 below, the 2-stroke engine depends on scavenging air to force the exhaust gases out instead of a 4-stroke engine that uses the piston to more completely force out the exhaust gases.

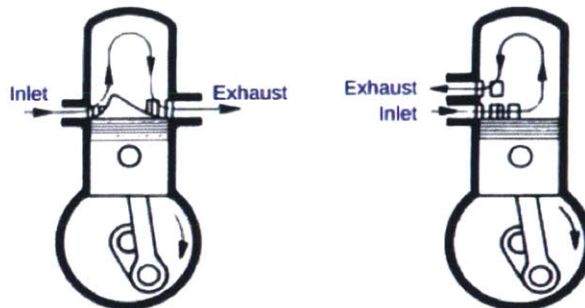


Figure 1.2. Two arrangements for the scavenging process of a 2-stroke engine [4].

## 1.2 Diesel Engine Advantages

When compared to gasoline SI engines, diesel engines offer many advantages in terms of efficiency, mechanical properties, engine emissions, and fuel benefits. Because diesel engines have higher compression ratios (12 to 24 vs. 8 to 12 for SI), their expansion stroke is relatively larger than a similar sized SI engine and their fuel-conversion efficiency is therefore higher [3]. Although for the same  $r_c$  diesels are theoretically less fuel-efficient than SI engines, it is the fact that diesels are not knock limited, which increases  $r_c$  and fuel-conversion efficiency. This higher efficiency is achieved in diesel engines due to the combustion gases being spread out over a larger expansion stroke compared to an SI engine, which reduces the temperature of the gases and the heat expelled. This principle can be demonstrated thermodynamically by the equation for thermal efficiency of a heat engine, Equation 1.1 below [6]:

$$\eta_{TH} = 1 - \frac{Q_{out}}{Q_{in}} \quad (\text{Eqn. 1.1})$$

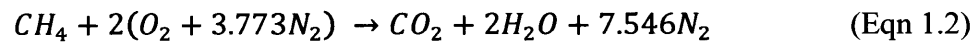
When the heat expelled,  $Q_{out}$ , decreases, as in the case of diesel engines, the thermal efficiency increases. Because SI engines are knock limited, they have a smaller relative expansion stroke and therefore much of the heat energy from combustion is directed away from the piston, making  $Q_{out}$  larger.

Additionally, diesel engine power is controlled by the amount of fuel injected into the cylinder instead of air throttling used in SI engines. This means there is less interference with the induction of air into the cylinder, which maximizes the volumetric efficiency,  $\eta_v$ , of the engine, and decreases pumping losses [3].

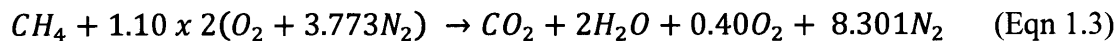
In general, diesel engines are more durable and reliable than their SI counterparts. Diesel engines are made with less sensitive materials and do not require the implementation of sophisticated spark ignition control devices that can be unreliable in SI engines [7]. Also, the lower exhaust temperatures of diesel engines remove the need for additional cooling systems required for gasoline engines [1]. This robustness that is characteristic of the diesel engine can cause them to last much longer than SI engines; it is not uncommon for diesel engines to operate for hundreds

of thousands of miles before needing maintenance on critical components [1]. Only recently, with the introduction of more intricate control units on diesel engines in an effort to curb air emissions, has there been a loss in engine durability [7].

Diesels also produce characteristically lower carbon monoxide (CO) and hydrocarbon (HC) exhaust emissions when compared to SI engines. CO in engine exhaust, generally speaking, stems from the incomplete combustion of the fuel in the cylinder [8]. To understand what incomplete combustion is, it helps to show an example of stoichiometric combustion with the Equation 1.2 below:



Using the molar masses of the constituent elements, the equation shows that it takes 276.5 grams of air to completely burn 16 grams of methane fuel (CH<sub>4</sub>), or an air to fuel equivalence ratio (AFR) of about 17.3. Now, if there is a 10% excess of air, or lean combustion, the process looks like Equation 1.3 below:



As Equation 1.3 shows, lean combustion theoretically produces no CO emissions. However, if the mixture is fuel-rich, combustion would not simply produce CO<sub>2</sub>, H<sub>2</sub>O, and N<sub>2</sub> as seen above. There would not be enough oxygen to fully oxidize the fuel, which would create additional products of CO and H<sub>2</sub>. Since diesels typically run fuel-lean in normal operations, CO is not a substantial pollutant. Hydrocarbons are also not a substantial pollutant in diesel exhaust emissions, with SI engines producing about 5 times more HC [3].

Also, diesel engines operate with a superior fuel. Although on a per mass basis, gasoline is more energy rich than diesel, the density of diesel fuel makes it about 5.5% more energy rich than gasoline on a per volume basis [3]. Adding in the thermodynamic and mechanical advantages, diesel engines are approximately 25-35% more fuel-efficient than SI engines [1].

Lastly, diesel fuel is less hazardous than the gasoline used in SI engines. The flashpoint of gasoline is around  $-45^{\circ}\text{F}$  whereas diesel fuel's flashpoint is  $>100^{\circ}\text{F}$  [9,10]. This means that at room temperature, gasoline releases vapors that can support a flame, whereas diesel fuel cannot. For many commercial operations, this equates to less restrictive safeguards for storing and handling diesel fuel than for gasoline. For example, there are additional, sometimes more stringent firefighting requirements reserved for small passenger vessels defined in Title 46 of the Code of Federal Regulations (CFR) that have a gasoline powered engine instead of a diesel engine [11]. The cost of complying with additional firefighting measures for gasoline engines is just another reason why diesel engines dominate many commercial sectors.

### **1.3 Diesel Engine Applications**

The advantages of diesel engines make them widely used in many different industries. Freight transportation, agriculture, and mining, among many other U.S. industries, all use diesel engines in their operations due to their unmatched fuel economy, packaging efficiency, and durability [1].

High-quality freight transportation is essential to the success and growth of the U.S. economy. Almost 90% of all the freight tonnage that the U.S. transports is powered by diesel engines because they are reliable and drastically reduce the cost of fuel for long distances travelled [1]. An investigation into the 1997 breakdown of highway and non-highway energy consumption in the U.S. shows that 100% of inner-city buses, water-borne freight, and rail freight were powered with diesel engines [1].

The agriculture sector has also benefited immensely with the inclusion of diesel engines. Before World War II, there were nearly 25 million people who lived on farms and used tractors that averaged about 25 horsepower to produce the following crop outputs: wheat - 17 bushels per acre, corn – 36 bushels per acre, cotton – 273 lbs per acre [1]. In 1997, less than 1 million people lived on farms and used tractors averaging 66 horsepower to produce: wheat – 43 bushels per acre, corn – 134 bushels per acre, and cotton – 618 lbs per acre [1]. The output increased despite decreases in the absolute fuel consumption and labor input, which the U.S.

Department of Agriculture (USDA) attributes to the substitution of diesel-powered machinery over previously used gasoline-powered machinery [1].

Mining is a broad term used to cover the extraction of many different natural resources such as coal, oil and gas, and even salt. The bituminous and lignite coal mining industry, valued at \$12 billion in 1997, is responsible for moving large amounts of material including coal and heavy machinery, and it relies on diesel engines for 72% of the operations [1]. Additionally, the oil and gas mining industry in 1997 used diesel power for 85% of drilling operations and 52% of all support operations [1]. The reason for choosing diesel power is due to the low operational cost and high-energy efficiency associated with it.

There are also other industries such as defense and transportation that widely use diesel engines, the main reason being that they have a higher fuel economy when compared to SI engines, and are durable and reliable enough to ensure continuous operations.

## **1.4 Diesel Engine Disadvantages**

Despite the many advantages of using diesel engines in industry, there are also disadvantages. For one, in-cylinder combustion in diesel engines causes them to be noisier when compared to SI engines [7]. While this may seem like a minute disadvantage, acoustic signature is a significant feature in selecting the optimal power plant in many applications such as naval ships and other military vehicles. Noise pollution is also regulated under United States Code (U.S.C) Title 42, Section 4901, which aims to reduce the detrimental effects of noise on public health and welfare [12]. Diesel engines have thus needed to fulfill the requirements of the Noise Control Act of 1972, which undoubtedly increased the cost of compliance.

Another disadvantage of diesel engines is that they emit high levels of nitrogen oxides ( $\text{NO}_x$ ) and particulate matter (PM) in their exhaust.  $\text{NO}_x$  refers to the summation of the different forms of nitric oxides, specifically, nitrogen oxide (NO) plus nitrogen dioxide ( $\text{NO}_2$ ).  $\text{NO}_x$  and PM are designated “criteria pollutants” by the Environmental Protection Agency (EPA) meaning permissible emission levels are set based on their respective harmfulness to both people and the

environment [13]. NO forms in the engine cylinder through the three sequential processes shown below in the following chemical equations, known as the Zeldovich mechanism [3]:



It has been established that the combustion of fuel disassociates certain compounds into their elemental nature ( $O_2 \rightarrow O$ ) as they oxidize the hydrocarbons present in the fuel. This is the same scenario with the formation of NO. NO forms during combustion because of the oxidation of atmospheric  $N_2$  at high temperatures [3]. This mode of formation is referred to as “thermal  $NO_x$ ,” and it is the primary mechanism in NO creation [3,14]. Additionally, “fuel  $NO_x$ ” is formed due to the oxidation of nitrogen content of the fuel, with diesel fuels typically containing more nitrogen than gasoline [3,14]. However, the significance of the fuel’s nitrogen in the formation of NO is far outweighed by the atmospheric  $N_2$  in the cylinder air [3]. For diesel engines,  $NO_2$  is also a significant compound found inside the cylinder.  $NO_2$  is typically formed during low speeds in diesel engines and can account for up to 20% of the total exhausted  $NO_x$  [3].

$NO_x$  emissions are hazardous both in the NO and  $NO_2$  form. NO emissions in lower concentrations are generally non-hazardous, but in high concentration they can cause body paralysis, spasms, and central nervous system problems [15]. NO behaves similarly to CO in that it reduces the absorption of oxygen into blood, but in the amounts typical of engine exhaust, NO alone is generally only harmful to infants and people highly sensitive to it [14]. NO is most hazardous to public health and the environment in its ability to combine with  $O_2$  to produce  $NO_2$ , a poisonous reddish-brown gas that causes a host of respiratory illnesses such as pneumonia, bronchitis, and pulmonary edema [15]. It does not take large concentrations of  $NO_2$  to be hazardous, either. The EPA has set  $NO_2$  acceptable limits at 0.053 parts per million (ppm) for public health and welfare in an effort to reduce the amount of illnesses caused by  $NO_2$  [16].  $NO_2$  is destructive to the environment as well, as it produces smog when combined with HC or volatile organic compounds (VOC) [17].

In addition to emitting CO<sub>2</sub>, H<sub>2</sub>O, CO, HC, and NO<sub>x</sub>, diesel engines also emit PM, which consists of solid carbonaceous particles in the form of soot. This emission is commonly seen as the black smoke that is ejected from the tailpipe of heavy-duty machinery, and it exists due to the incomplete combustion of HC in the cylinder. At temperatures below 500°C, organic compounds such as lube and fuel oil derivatives attach to soot particles in the exhaust stream [3]. These organics are just one of the three fractions that comprise PM, shown below in Figure 1.3, and they are referred to as the soluble organic fraction (SOF). The other two are the solid fraction, being the elemental carbon and ash particles, and also inorganics called sulfate particulates, which include sulfuric acid and water. All three are detrimental to human health, but the SOF is especially dangerous as it contains most of the polynuclear aromatic hydrocarbons (PAH), which are compounds that contain between 2 and 6 benzene rings [18]. Benzene is a carcinogenic organic compound that has been linked to mutagenic changes in human DNA, which can result in various forms of cancer.

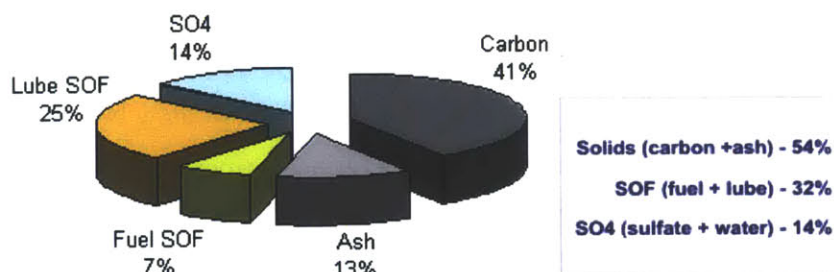


Figure 1.3. Breakdown of the constituent PM fractions [18].

The intricate formation of PM creates a wide range of particle sizes from nm-diameter size particles to  $\mu\text{m}$ -size particulate agglomerates. PM that is the result of incomplete combustion in diesel engines typically is of a fine or ultrafine size, corresponding to diameters below 2.5  $\mu\text{m}$ . Table 1.1 below shows the particle size range for PM:

Particle Classification	Abbreviation	Size Range
Course Particles	PM <sub>10-2.5</sub>	2.5 – 10 μm
Particles below 10 μm	PM <sub>10</sub>	< 10 μm
Fine particles	PM <sub>2.5</sub>	< 2.5 μm
Ultrafine particles or nanoparticles	UFP	< 0.1 μm

Table 1.1. Range of particle sizes classified as PM. Adapted from [18].

PM is a dangerous air pollutant due to this very reason; particles are small enough to be suspended in air, which makes them easy to inhale. The problem with trying to modify diesel engine operations to decrease PM emissions is that a decrease in PM causes an increase in NO<sub>x</sub>, and vice versa. This is referred to as the NO<sub>x</sub>-PM trade-off and this relationship makes it difficult to affect both PM and NO<sub>x</sub> emissions through engine design alone. For instance, retarding the injection timing has been shown to reduce NO<sub>x</sub> emissions by delaying combustion, so that smaller concentrations of NO<sub>x</sub> are formed at a lower in-cylinder temperature [3, 19]. This, however, increases the PM, which requires additional downstream filtering. It is possible, though, to take advantage of the high amounts of NO<sub>x</sub> in the exhaust by employing a catalyst, which serves to oxidize the 85-95% NO in the exhaust into about 50% NO<sub>2</sub> [20]. This oxidation of soot through NO<sub>2</sub> effectively lowers the regeneration temperature, but requires additional downstream catalysis of the NO<sub>x</sub> [20]. This theme will be further explored in *Section 1.6*, but first an explanation of the regulations surrounding diesel engine emissions is necessary.

## 1.5 Diesel Emissions Regulations

Because diesel engines are responsible for emitting hazardous amounts of CO, HC, NO<sub>x</sub>, and PM, various regulatory bodies enforce emission standards to ensure the safety of people and the environment. Before addressing the specific requirements that applicable diesel engines must meet in order to curb air emissions, it is helpful to introduce the authorities given to these regulatory bodies by law.

Each geographical location has their own, unique governing body that establishes and proposes laws with regard to reducing atmospheric pollutants. For instance, in the United States, the EPA writes and enforces air emissions law as prescribed by the Clean Air Act (1990 Amendment)

under 42 U.S.C. Ch. 85, Subchapter I, Part A [21]. Other locations such as Europe, has the European Union (EU) propose standards in reducing harmful air emissions. Once authority is given to the agency by government legislation, the EPA drafts air emissions regulations and submits them as a Notice of Proposed Rulemaking (NPRM) in the Federal Register (FR), which allows involved stakeholders, such as industry partners, to comment on draft law and offer edits or critiques. Once the rule has been reviewed, the EPA can then codify the rule in the CFR, which specifies the detailed aspects of how to follow the law [22]. These federal laws represent the minimum standards to be achieved, though, and do not preclude states from adopting more stringent regulations. For example, California has adopted its own air emission standards proposed by the California Air Resources Board (CARB), which are more stringent than federal statutes in many cases [23]. For many commercial operations, this reality means either complying with the stricter emissions guidelines, or suspending operations in a particular area.

In promulgating air emissions law, regulatory bodies need to understand the source of air emissions. It would be ineffective to propose rulings that would only affect low-level offenders; therefore research is required to understand the sources and amounts of air pollutants. Consequently, diesel engines emit enough CO, HC, NO<sub>x</sub>, and PM to necessitate the EPA to form specific standards for diesel air emissions. EPA air emission standards are divided into 6 subgroups based on the vehicle's operation. They are: Cars and Light Trucks, Heavy-Duty Onroad Engines, Nonroad Diesel Engines, Locomotives, Marine Engines, and Stationary Diesel Engines [23]. Each category has specific requirements with respect to reducing CO, HC, NO<sub>x</sub>, and PM, and since the inception of the Clean Air Act Amendment in 1990, emissions have reduced significantly across all vehicle types.

To expound on the specific emission requirements for each category would be excessive and span across different types of engines and fuels (SI, diesel, natural gas), therefore only heavy-duty onroad engines and nonroad diesel engines will be described. Additionally, CARB emissions requirements will not be explicitly identified.

Heavy-duty onroad engines, as defined in 40 CFR 85.502, "describes all engines intended for use in heavy-duty vehicles," or vehicles with a gross vehicle weight rating (GVWR) > 8,500 lbs

[24, 25]. This description accurately describes most trucks and buses. To precisely model and test the emissions levels for heavy-duty engines, the Transient Federal Test Procedure (FTP) heavy-duty cycle is used [25]. Duty cycles, in general, replicate the operational characteristics the engine will most likely encounter on the road. The FTP most accurately models both city and open-road driving in the U.S. The emissions requirements for *heavy-duty diesel engines* have changed immensely over the years and are shown below in Figure 1.4:

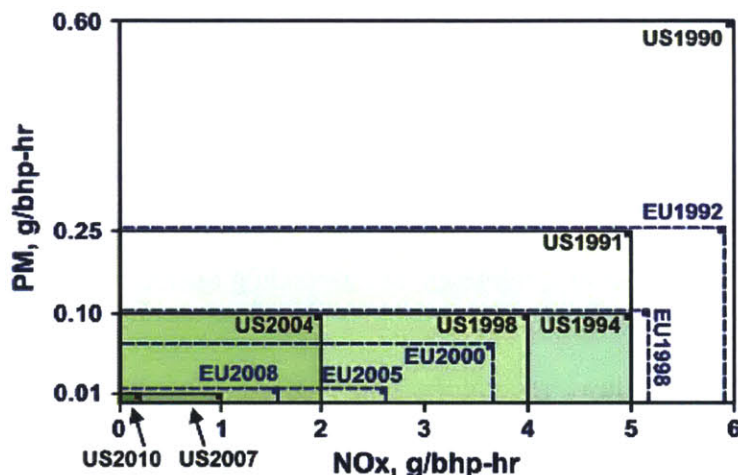


Figure 1.4. Reductions of PM and NOX in heavy-duty diesel engines over the past 20 years [26].

Similarly, nonroad diesel engines have seen a large reduction in emissions. Nonroad engines are defined in 40 CFR 1068.30 as engines that are: (i) “used in or on a piece of equipment that is self-propelled or serves a dual purpose by both propelling itself and performing another function,” (ii) “used in or on a piece of equipment that is intended to be propelled while performing its function,” or (iii) “by itself or in or on a piece of equipment, it is portable or transportable, meaning designed to be and capable of being carried or moved from one location to another” [27]. These definitions cover garden tractors, off-highway mobile cranes, bulldozers, lawnmowers, and mining vehicles provided they are not conducting in underground mining operations, which is regulated by the Mine Safety and Health Administration (MSHA) [28].

Regulation of nonroad diesel engine emissions has followed a 3-tiered phase-in period, with Tier 4 standards currently being phased in (2008-2015). Tiers 1-3 were promulgated in 1998, with Tier 1 having a phase-in period from 1996-2000, Tier 2 from 2001 to 2006, and Tier 3 from 2006 to 2008 [28]. Engine model years falling within the phase-in period are required to comply with

the applicable Tier standards. It should be noted that Tiers 1 through 3 emissions regulations are all accomplished using engine design modifications and typically do not require the use of after-treatment. Tier 4 nonroad regulations requires the additional reduction of NO<sub>x</sub> and PM by 90%, which, barring any significant advances in diesel technology, requires the use of an after-treatment device for certain diesel engines depending on their power and model [28, 29]. The air emission reductions for nonroad engines are shown below in Figure 1.5:

EPA and EU nonroad emissions regulations: 37 – 560 kW (50 – 750 hp)

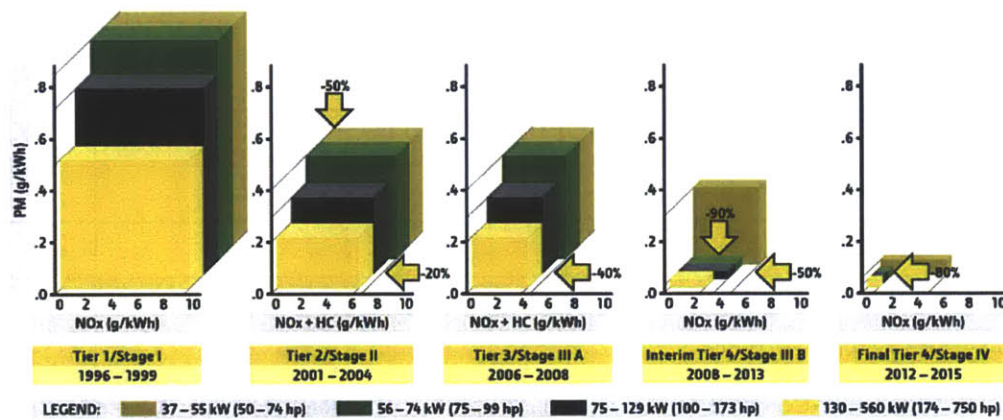


Figure 1.5. Reductions of PM and NOX in nonroad diesel engines [30].

The test cycle used in measuring Tier 1-3 emissions from nonroad diesels is a steady-state test cycle equivalent to the international ISO 8178 standard, whereas Tier 4 emissions are measured using the more stringent Nonroad Transient Cycle (NRTC) in addition to steady-state [28]. Because emissions requirements are becoming more limiting with regard to NO<sub>x</sub> and PM (CO and HC have essentially remained unchanged over the years), action needs to be taken with diesel engines to be in compliance. Tier 4's 90% reduction in NO<sub>x</sub> and PM provides no time for advance diesel technology to meet these strict demands, therefore, compliance must be achieved by using after-treatment devices.

## 1.6 After-treatment Devices

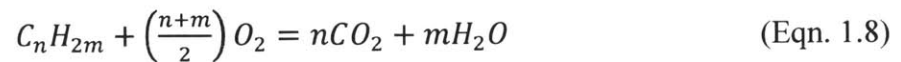
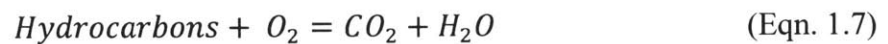
Various devices can further decrease levels of CO, HC, NO<sub>x</sub>, and PM in the exhaust stream. Some after-treatment retrofit devices can accomplish individual reductions in a specific pollutant, whereas many of them are able to simultaneously reduce multiple pollutants using one device. Each after-treatment device is unique in its application to certain industries; that is, some

may be tailored to marine diesel engines whereas others may provide emission reductions for heavy-duty diesel engines, based on the applicable requirements from the EPA. The industry targeted for each after-treatment device is what influences the design of the device and its emissions reduction performance. Table 1.2 below shows some of the common after-treatment devices and their respective reductions in CO, HC, NO<sub>x</sub>, and PM [31].

Technology	Typical Emission Reductions (%)			
	PM	NO <sub>x</sub>	HC	CO
Diesel Oxidation Catalyst (DOC)	20-40		40-70	40-60
Diesel Particulate Filter (DPF)	85-95		85-95	50-90
Partial Diesel Particulate Filter (pDPF)	Up to 60		40-75	10-60
Selective Catalytic Reduction (SCR)		Up to 75		
Closed Crankcase Ventilation (CCV)	varies			
Exhaust Gas Recirculation (EGR)		25-40		
Lean NO <sub>x</sub> Catalyst (LNC)		5-40		

Table 1.2. Diesel after-treatment devices and their respective emission reductions. Adapted from [31].

Although specific after-treatment devices can be used to accomplish overall reductions in CO, HC, and PM, usually different devices have to be used in series to achieve total compliance with the regulations. Heavy-duty engines are able to do this by using a diesel oxidation catalyst (DOC), DPF, and selective catalytic reduction (SCR) device. The DOC is the first device the engine exhaust encounters, and its purpose is to reduce CO, HC, and the SOF portion of the PM [32]. The DOC does this through oxidation of each pollutant via platinum (Pt) catalyst particles and the equations below show the respective oxidation mechanisms of each emission [32].



In addition to decreasing CO, HC, and PM, DOCs also can increase the (NO<sub>2</sub>/NO<sub>x</sub>) ratio through the oxidation of the NO at temperatures around 300°C [32]. In certain circumstances, the

increase in NO<sub>2</sub> is advantageous due to the ability of NO<sub>2</sub> to more effectively oxidize PM. Of course, the additional NO<sub>2</sub> has to be treated downstream of the DOC. The downside of the DOC is its oxidation of sulfates in the exhaust stream. Depending on the sulfur content of the fuel, enough of the inorganic sulfate particulates can oxidize to form sulfur trioxide (SO<sub>3</sub>) and then sulfuric acid (H<sub>2</sub>SO<sub>4</sub>) in the following equations [32]:



In addition to being hazardous to health, H<sub>2</sub>SO<sub>4</sub> can compromise catalysis and reduce the effectiveness of emissions filtration [32]. For this reason, low sulfur fuels are essential to ensuring the reliability and functionality of the after-treatment system. Also, in some cases the total particulate matter (TPM) can actually increase despite reductions in CO and HC, due to the high sulfur content of the fuel as seen in Figure 1.6 [32].

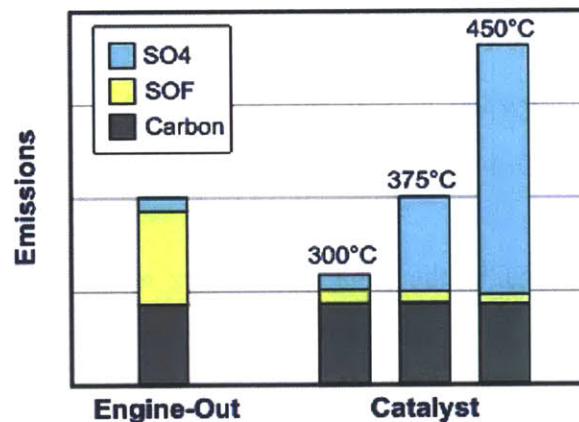


Figure 1.6. Certain operating conditions and fuel sulfur levels can increase TPM [32].

Diesel particulate filters have been used in controlling exhaust PM emissions since 1985, when Mercedes started installing DPFs on their vehicles [2]. For 30 years, DPF technology and understanding have progressed drastically to allow for >90% reductions in the exhaust stream PM through after-treatment devices. DPFs work by trapping the solid fraction of the PM, principally the black carbon or soot. Over time though, the DPF accumulates large amounts of soot, which causes an increase in pressure drop ( $\Delta P$ ) across the filter. This increase in  $\Delta P$  has

adverse effects on the engine performance and can cause a severe fuel economy penalty. To address this, many DPFs are able to *regenerate*, or oxidize soot at different exhaust temperatures.

There are two principle methods of regeneration: passive and active. Passive regeneration is able to continuously burn off soot particles in the DPF at the regular exhaust temperature. Usually the DPF is coated with catalyst particles that enable the soot to be oxidized at a much lower temperature [2]. Active regeneration relies on the periodic oxidation of filter soot through an increased exhaust temperature that is the result of a change in the fuel injection regime [2]. With the DOC decreasing the CO and HC, and the DPF decreasing the PM, the last device that is used to treat the exhaust is the SCR to decrease any remaining NO<sub>x</sub>.

Most SCR devices depend on the chemical reduction of urea (CO(NH<sub>2</sub>)<sub>2</sub>) into ammonia (NH<sub>3</sub>), which combines with the exhaust gas to produce non-hazardous gaseous nitrogen and water. There are many different chemical reactions that can yield N<sub>2</sub> and H<sub>2</sub>O downstream of the SCR, but the basic theoretical mechanisms for this reaction are shown below in Equations 1.12 and 1.13 [33]:



On the downstream side of the SCR, the exhaust gases are removed of hazardous amounts of NO<sub>x</sub>, and can exit the tail pipe. A typical heavy-duty diesel engine after-treatment system is shown below in Figure 1.7:

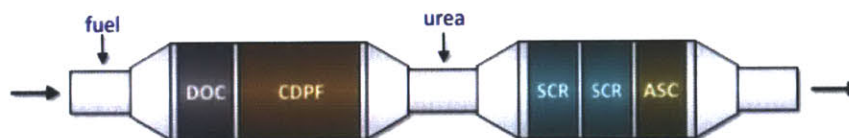


Figure 1.7. Common arrangement of diesel after-treatment devices to meet EPA standards [34].

An after-treatment system composed of a DOC, DPF, and an SCR can significantly reduce exhaust gas emissions, and allow applicable diesel engines to be in compliance with stricter

emissions regulations. However, constant use of this system results in the decreased performance of individual components, which can negatively affect engine performance. The DPF, in particular, is subject to many adverse effects such as the accumulation of incombustible, lubricant-derived ash in the substrate. This effectively clogs the filter, which reduces the filtration efficiency in addition to causing backpressure in the engine. To effectively address this concern first requires an in-depth understanding of different types of DPFs and the governing equations surrounding their operation.

(This page intentionally left blank)

## 2 DIESEL PARTICULATE FILTERS

With increasingly stringent emissions regulations, DPFs have recently been the subject of intense research. Cars and light trucks will have to comply with the newly adopted Tier 3 emissions regulations, which require an order of magnitude reduction in PM (from Tier 2) by 2022 [35]. Model year 2007 and later heavy-duty engines must reduce PM to 0.01 g/bhp-hr [25]. While standards have not explicitly required the use of a DPF, there are no suitable alternatives that would achieve such high reductions in PM with just engine optimization alone. This has caused the acceptance of DPFs on all medium and heavy-duty diesels in North America, with approximately 2 million being installed from 2007-2010 [2]. As such, current research is dedicated to improving the performance of the DPF and understanding its interaction with other components of the engine and after-treatment assembly.

Research has been focused on commonly used DPF substrates, as their application is prevalent in both the light and heavy-duty onroad market. These substrates consist of a honeycomb wall-flow monolith that is typically constructed using a porous cordierite or silicon carbide (SiC) material. Deconstructing the exhaust flow process in porous ceramic DPFs has revealed specific governing equations that can explain the various sources of pressure drop and their resultant effect on engine fuel economy.

However, there has been less research with regard to different substrate materials and configurations, such as SMF filters. This reality stems from regulations targeting larger air emitters, such as onroad heavy-duty trucks, instead of focusing on diesel engines in nonroad and other applications, where novel DPF substrates are more common. Regardless, much of the science has been studied and developed around porous ceramic DPFs, and it serves as a starting point for determining the application to other substrate materials such as SMF DPFs. Before experimentation can begin in SMF DPFs, a thorough understanding of the properties of porous ceramic DPFs and SMF DPFs is required to determine how interchangeable the methods are with each other.

## 2.1 Wall-Flow Monolith Characteristics

The ceramic wall-flow monolith is the most commonly used filter, controlling about 70% of the global DPF market [36]. The basic structure of the wall-flow monolith DPF is a cylindrical filter with inlet and outlet channels alternatively plugged to force exhaust gas to filter through the walls of the substrate, as seen in Figure 2.1 [37]. The porosity of the medium allows PM in the exhaust to collect within and on the filter walls, and can reduce anywhere from 95-99.9% of all solid fraction particles in the PM [2]. Accounting for SOF and sulfates, the wall-flow monolith DPF has a high filtration efficiency, with a total reduction in PM of about 85-95% [2]. This PM accumulation can clog the filter, and require oxidation via either active or passive regimes. Active regeneration, as previously explained, raises the exhaust temperature through additional fuel combustion or heating methods, whereas passive relies on catalysts to lower the soot oxidation temperature.

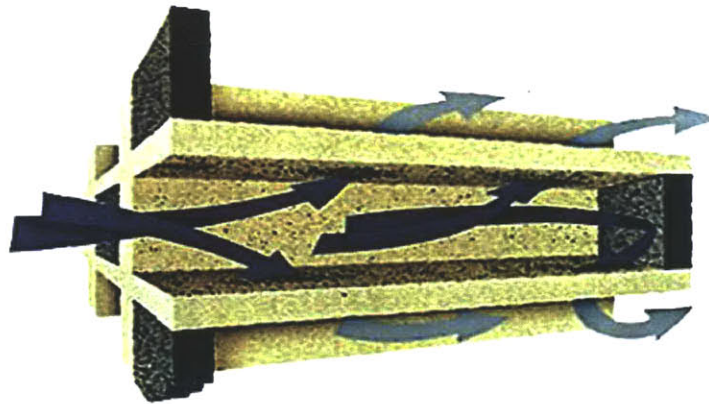


Figure 2.1. Wall-flow monolith structure [37].

The substrate material used in wall-flow monolith DPFs is typically cordierite or SiC because of their mechanical and thermal advantages. Cordierite is a ceramic with a chemical formula  $2\text{MgO}\cdot 2\text{Al}_2\text{O}_3\cdot 5\text{SiO}_2$  and it has a characteristically low thermal expansion coefficient, which means that it is less susceptible to geometric changes with changing temperature [36]. Conversely, SiC is less susceptible to melting, but has a higher thermal expansion coefficient and typically is more expensive [37]. A comparison of the two filter materials can be found below in Table 2.1 [38].

Property	Cordierite	SiC
Channel Width [mm]	1.3 - 2.1	1.0 – 1.6
Wall Thickness [mm]	0.3 - 0.5	0.3 – 0.8
Mean Pore Size [ $\mu\text{m}$ ]	13 - 34	8 - 17
Porosity [%]	45 - 50	42 - 58
Permeability [ $\text{m}^2$ ]	$0.5 \times 10^{-12}$	$1.2 - 1.3 \times 10^{-12}$
Melting Temperature [ $^{\circ}\text{C}$ ]	1450	1800 - 2400

Table 2.1. Material differences between cordierite and SiC DPF substrates. Adapted from [38].

Although there are noticeable differences between cordierite and SiC DPF properties, the mechanisms of soot and ash deposition in the filter are essentially the same.

## 2.1.1 Soot and Ash Accumulation in Wall-Flow Monolith DPFs

The accumulation of soot and ash in wall-flow monolith DPFs is well documented and understood [37, 38, 39, 40, 41]. Initially, the soot and ash transports into the pores of the filter in what is referred to as depth filtration. This mode of accumulation is detrimental to the  $\Delta P$  across the filter as it minimizes the available pore volume of the substrate and makes it more difficult for exhaust gas to penetrate. As more soot and ash is loaded into the filter, the porosity of the substrate decreases and material builds up in the filter, eventually collecting on top of the channel walls, in what is referred to as cake filtration. This filtration regime increases the  $\Delta P$  across the filter, but at a lesser slope than depth filtration. Figure 2.2 below illustrates how the accumulation of soot and ash can increase  $\Delta P$  in DPFs [39].

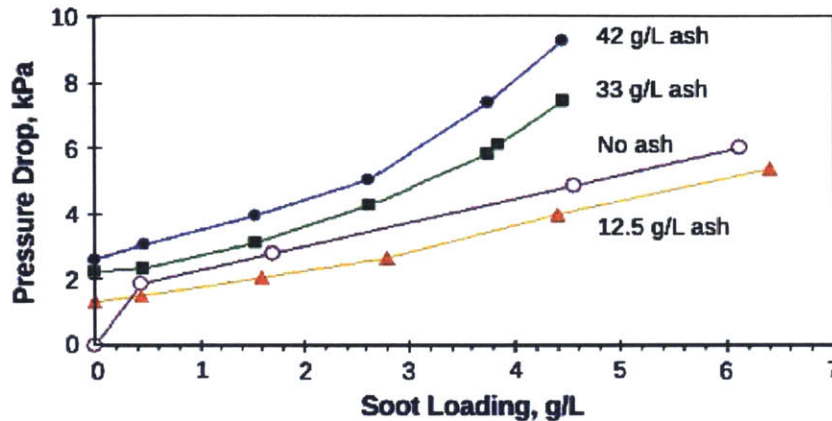


Figure 2.2. The effect of soot and ash loading on pressure drop across a D5.66" x 6", 200 cpsi, .012" wall thickness catalyzed DPF, measured with ambient air at 20,000 h-1 space velocity [39, 40].

Although the buildup of soot and ash can increase the pressure drop across the filter, regeneration can help to oxidize the soot to free up more pore space. Regeneration, though, leaves behind ash particles, typically derived from lubricant oil additives, which can cause an increase from 50-100%  $\Delta P$  [41]. Lubricant-derived ash constitutes only about 1% by mass of the incoming exhaust flow PM, but because the ash does not penetrate the filter, it builds up over time [41]. Studies have shown that regeneration, either active or passive, tends to cause the nm-scale ash precursors deposited on the soot particles to shrink together and form into larger agglomerates at high temperatures as seen in Figure 2.3 [39]. Knowing the basic transport mechanisms of ash and soot in the wall-flow monolith DPF, it is possible to determine the resultant effect on engine backpressure and fuel economy.

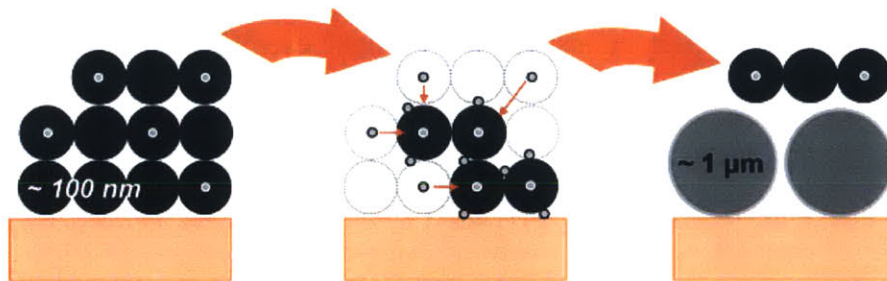


Figure 2.3. Ash and soot transport mechanism in wall-flow monolith DPF [39].

## 2.1.2 Backpressure and Fuel Economy

Having the basic understanding of how soot and ash collects in the wall-flow monolith DPF, it is helpful to understand the effects of exhaust backpressure on fuel economy. Backpressure is

simply the hydraulic resistance that a fluid must overcome so that it can move. In a diesel engine there are many sources of backpressure such as pipe bends (gravity), after-treatment devices, and mufflers, among others [42]. When a DPF is loaded with soot, the resistance or pressure across the filter will increase, thus increasing the total backpressure. This causes the diesel engine to have to work harder to eject the gases from the cylinder, and the pressure ratio across the pump consequently decreases [43]. A decrease in the pressure ratio means that less air is being added to the cylinder, so as a way to provide power to overcome the exhaust manifold backpressure, more fuel is injected which causes a fuel economy penalty [43].

Various experiments and field studies have been conducted to determine the fuel consumption penalty (FCP) with incremental rises in backpressure. For turbocharged engines, a 1.5-2.5% increase in fuel consumption was reported per 10 kPa increase in backpressure [42]. As Figure 2.4 below shows, there was a 1.8% brake specific fuel consumption (BSFC) increase per 10 kPa increase in an 85 kW Deutz diesel engine, when operating at 2200 rpm and exceeding the OEM recommended backpressure limit (which tends to be very conservative) [42]. Additionally, Figure 2.4 shows the resultant increase in soot production due to increase in exhaust backpressure. The fuel-rich combustion to overcome increased backpressure results in higher PM amounts in the exhaust, which only serves to compound the problem, if not regenerated.

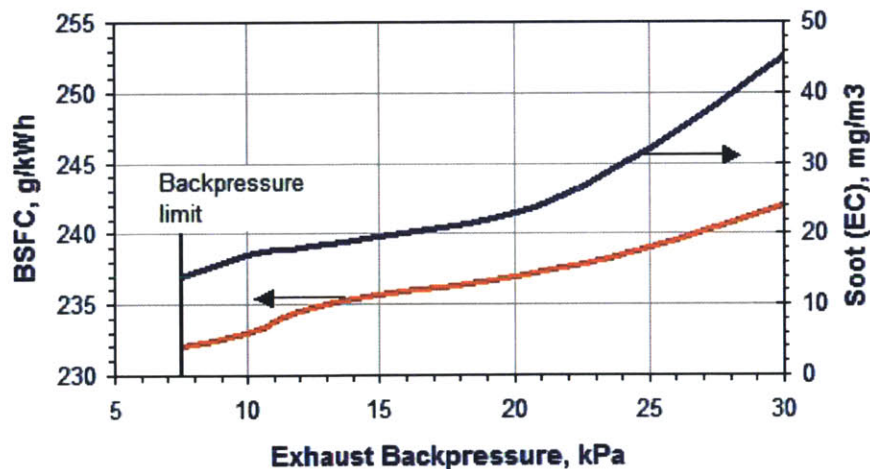


Figure 2.4. Effect of exhaust backpressure on specific fuel consumption and soot production for 85 kW Deutz BF6M 1012 Euro I diesel engine at 2200 rpm [42].

### 2.1.3 Governing Equations

Pressure drop across a wall-flow monolith DPF is composed of many different sources. Contraction and expansion of inlet and outlet exhaust gases, frictional losses along the length of a channel, and pressure losses along the wall, ash, and soot layer all contribute to the total  $\Delta P$  across the filter [37, 38]. All have varying degrees of contribution to pressure drop, with frictional losses associated with the wall, ash, and soot layers accounting for approximately 50-90% of the total [38]. As this is the largest contributor to the total filter  $\Delta P$  and also the least understood, it will be investigated in depth.

Deriving the appropriate fluids equation for exhaust flow through a wall-flow monolith requires making several assumptions, namely: incompressible flow and Reynolds Number ( $Re$ )  $\ll 1$ , i.e. creeping, laminar flow. The derivation of Navier-Stokes Equations to Stokes Flow is shown below in Equation 2.1 and 2.2:

$$\rho \frac{D\vec{u}}{Dt} = \rho \frac{\partial \vec{u}}{\partial t} + \rho \vec{u} \cdot \nabla \vec{u} = -\nabla p + \mu \nabla^2 \vec{u} + \rho g \quad (\text{Eqn. 2.1})$$

Material derivative,  $\rho \frac{D\vec{u}}{Dt} = \rho \frac{\partial \vec{u}}{\partial t} + \rho \vec{u} \cdot \nabla \vec{u} = 0$  due to incompressible flow.

$$-\nabla p + \mu \nabla^2 \vec{u} + \rho g = 0 \quad (\text{Eqn. 2.2})$$

Where,

$\rho$  = fluid density

$u$  = velocity vector

$p$  = pressure

$\mu$  = fluid dynamic viscosity

$g$  = gravitational constant

Additional derivations and assumptions of the Stokes Flow equation result in Darcy's Law, which describes flow through a rigid, porous medium [44]. Darcy's Law is shown below in Equation 2.3 [37, 38]:

$$\Delta p = \left(\frac{\mu}{K}\right) \cdot u \cdot w \quad (\text{Eqn. 2.3})$$

Where,

K = permeability of porous medium

w = thickness of layer

Permeability depends on the intrinsic properties of the material such as porosity and pore diameter and is usually given by the manufacturer, but an estimation of K can be determined using the Kozeny-Carman correlation shown below in Equation 2.4 [37, 38]:

$$K = \left(\frac{1}{5.6}\right) \varepsilon^{5.5} d_p^2 \quad (\text{Eqn. 2.4})$$

Where,

$\varepsilon$  = porosity of filter wall

$d_p$  = diameter of pore, m

Because Equation 2.3 describes the pressure drop as a function of layer thickness, it appears to be best suited for cake layer pressure drop measurements, but adjustments of the permeability equation, Equation 2.4, can account for depth filtration effects on pressure drop by correcting the pore diameter. This distinction will become very important in analyzing the applicability of these governing equations to SMF DPFs.

## 2.2 SMF DPF Characteristics

Sintered metal fibers are used in DPF applications due to their overall high filtration efficiencies, innovative regeneration methods, low fuel penalty, and flexible exhaust requirements. Despite these numerous key advantages, the utilization of sintered metal DPFs is limited, accounting for only about 4% of the total DPF market [36]. The likely reason for this disparity between sintered metal and porous ceramic filters is the material weight. Ceramic cordierite and SiC have a material density of approximately 2.51 and 3.2 g/cm<sup>3</sup>, respectively [37, 45]. Some of the common metals used for SMF DPFs have a material density of 7.2 g/cm<sup>3</sup>, more than twice the

density of cordierite and SiC [46]. When accounting for filter porosity, the density of the SMF DPF is reduced by 85% to  $1.08 \text{ g/cm}^3$ , whereas the honeycomb density for most porous ceramic DPFs is about  $0.72 \text{ g/cm}^3$  [37]. Because SMF DPFs have such a high porosity, multiple filter cartridges have to be used to achieve substantial PM reductions, which exacerbates the weight problem. In the end, the overall weight of the SMF DPF assembly is much greater than the porous ceramic arrangement. This aspect of SMF DPFs makes them best suited for applications such as stationary power sources and mining vehicles, where additional weight is not as detrimental to the fuel economy than say a semi-trailer truck. Because there are many different types of SMF DPF arrangements and materials used, it is a daunting task to give specific details about each arrangement. For the sake of simplicity, the iron-chromium alloyed, electrically regenerative SMF DPF substrate, will be further explained in detail.

The SMF DPF is comprised of a material called Fecralloy, which consists of iron, chromium, aluminum, yttrium, and zirconium [46]. The aluminum forms a protective oxide layer that surrounds the base metals, and the yttrium prevents the corrosion of the fibers at high exhaust temperatures [47,48]. These Fecralloy fibers are arranged randomly in the X-Y (depth-wise) plane to form an approximate 1 to 1.5 mm thick schedule, and then sintered at high temperatures to create the filter [47]. The depth direction of the SMF substrate, however, is not arranged randomly [47]. The fibers decrease in diameter as a function of depth into the filter (inlet to outlet) and can be divided into 3 main size groups: top layer – 30-40  $\mu\text{m}$ ; middle layer – 20-30  $\mu\text{m}$ ; bottom layer- 10-20  $\mu\text{m}$  [47]. These fiber diameters are subject to manufacturing variability, though, and will be further explained in *Section 5.1*. In addition to the fiber diameter changing as a function of depth, porosity also changes slightly from the inlet to outlet side of the filter, with an overall average porosity of approximately 85% [48]. This too will be explained more thoroughly in *Section 5.5*. Figure 2.5 below shows the fiber distribution in SMF DPFs.

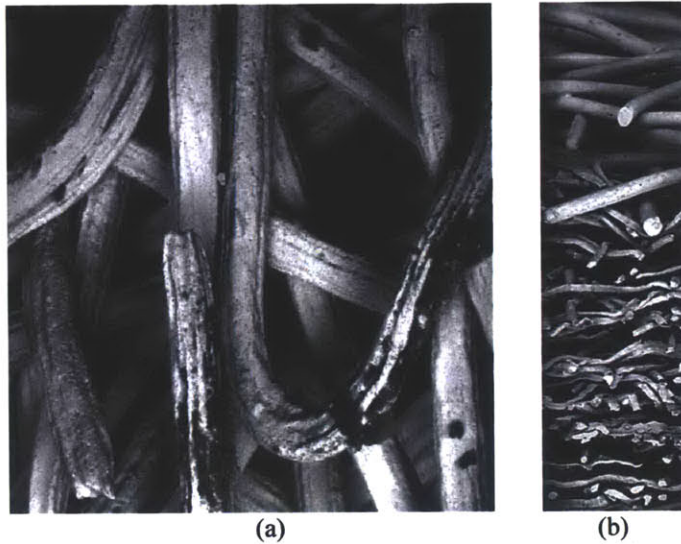


Figure 2.5. Top view of large fibers, (a) and cross section view, (b) of SMF DPF [47].

After the SMF sheets are sintered, they are shaped into a corrugated, cylindrical cartridge, which serves to increase the available filtration area. As previously mentioned, the filtration efficiency of each individual cartridge can be lower than the EPA's PM requirements; therefore they are stacked in series to further increase the filtration area and achieve higher soot reductions. This process of soot filtration into the corrugated cartridges is also fundamentally different than exhaust flow through a porous ceramic filter. Dirty exhaust flow enters the cartridge assembly axially, but penetrates through each filter in the radial direction, causing clean flow to leave through the middle of the cartridge. The cartridge assembly and flow characteristics of SMF DPFs can be seen below in Figure 2.6.

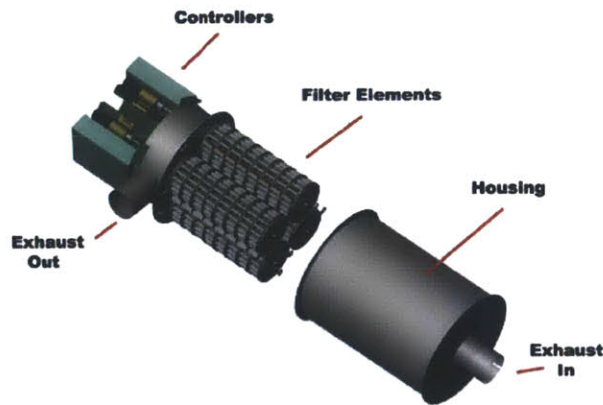


Figure 2.6. Complete SMF DPF assembly [49]

## 2.2.1 Soot and Ash Accumulation in SMF DPFs

The physical mechanisms of soot and ash collection in SMF DPFs are still being studied, but there are certain preliminary trends that exist, that differ greatly from the accumulation of soot and ash in wall-flow monolith DPFs. In wall-flow monoliths, the highest relative  $\Delta P$  occurs early in the filters lifetime in what is referred to as deep-bed or depth filtration. As more ash enters the pores of the ceramic substrate, the ash forms a cake layer on top of the channel walls, which causes a decreasing rate of  $\Delta P$ . In SMF DPFs, evidence shows that the depth filtration regime has a more gradual  $\Delta P$  slope, whereas cake filtration is marked by a steep increase in  $\Delta P$  as shown in Figure 2.7 [47, 50]. This phenomenon has also been shown in aerosol clogging of high-efficiency particulate air (HEPA) filters, which are in many facets geometrically similar to SMF DPFs.

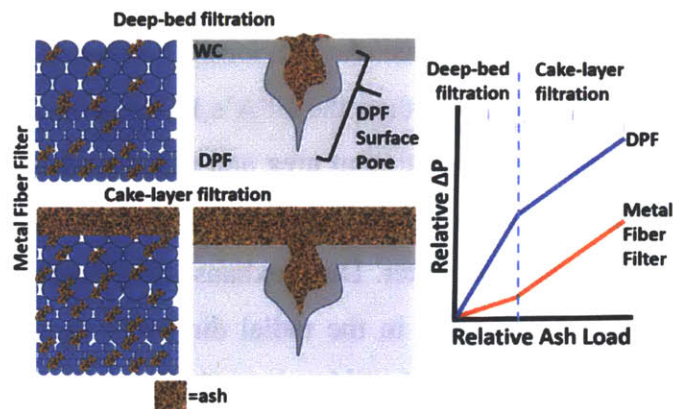


Figure 2.7. Preliminary ash deposition differences between porous ceramic DPFs and SMF DPFs [47, 50].

To fully understand the properties of soot and ash accumulation in SMF DPFs requires an understanding of the active electrical regeneration scheme. Most SMF DPFs, like wall-flow monoliths, have a means of determining the  $\Delta P$  across the filter during the operation of the engine. When the electronic controls sense the backpressure is of a level beyond OEM specifications, a flow controller can stop the flow to a single SMF cartridge or multiple cartridges, and pass high voltage through the conductive medium. The flow controllers essentially shut off exhaust flow to a certain section of the filter to minimize convective heat dissipation, and also to optimize energy usage during regeneration. The SMF filter has a low thermal mass, therefore it heats quickly and oxidizes soot in the cartridge quickly via resistive or Ohmic heating at temperatures typically above  $600^{\circ}\text{C}$  [47].

The ability for SMF DPFs to act as a selective filtering and heating medium gives it a very low fuel penalty of < 1% and also characteristically low backpressures of < 5 kPa [47, 48]. As with wall-flow monoliths, though, these regeneration events leave ash particles and agglomerates within the filter and over time they reduce the porosity of the filter, causing an increase in backpressure. To understand the methods of ash distribution in SMF DPF requires an analysis of the aforementioned governing equations to see if they are applicable to different filtration processes.

## 2.2.2 SMF DPF Governing Equations

To test the application of Darcy's Law and the Kozeny-Carman equation to SMF DPFs, several key assumptions must be made. First, it is assumed from experimental testing of porous ceramic DPFs, that the largest contributor to  $\Delta P$  in SMF DPFs derives from the losses due to the soot, ash, and fibers. Secondly, the use of Darcy's Law is applicable based on  $Re \ll 1$ , in the equation:

$$Re = \frac{u \cdot L}{\nu} \quad (\text{Eqn. 2.5})$$

Where,

$u$  = wall velocity, m/s

$L$  = characteristic length, m

$\nu$  = kinematic viscosity,  $m^2/s$

For SMF DPFs, the velocity term in Reynolds number is not the inlet velocity of the exhaust into the cartridge housing, but rather the radial velocity into the filter itself, and it is approximated to be 0.125 m/s based on design. The characteristic length term is the diameter of a single fiber, which ranges from approximately 10  $\mu m$  to 40  $\mu m$ , depending on which layer of the filter the flow is encountering. A wide range of exhaust temperatures are evaluated to represent the various engine loading operations, as well as to provide a safety factor for the kinematic viscosity. Exhaust temperatures from 0°C to 1000°C give kinematic viscosities from  $1.34 \times 10^{-5}$  to  $16.77 \times 10^{-5} m^2/s$ . In all cases, even with improbable exhaust temperatures,  $Re \ll 1$  and thus Darcy's Law can be used to determine  $\Delta P$  across the SMF DPF.

While the Kozeny-Carman equation (Eqn. 2.4) is a good estimation of permeability in porous media such as ceramic DPFs, it is not an accurate equation to model permeability in fibrous media such as SMF DPFs. This is due to the fact that the pore network of porous media such as ceramic cordierite and SiC is relatively easy to approximate given the porosity of the material is known and the estimation of the average pore size is not difficult to measure. This equation cannot be easily applied to anisotropic fibrous media for the same reason; the pore structure and network is not well defined, and thus other measures must be taken to determine permeability in fibrous media. Various empirical relationships exist in literature that can model the permeability of fibrous media based on its two most important characteristics: porosity and the diameter of the fiber [51, 52]. These relationships apply to a range of porosities and also ordered or disordered fibrous media. An example of one such empirical relationship is shown below in Equation 2.6 [51]:

$$K = \left( \frac{5.55}{e^{10.1(1-\phi)} - 1} \right) \cdot a^2 \quad (\text{Eqn. 2.6})$$

Where,

K = permeability of fibrous medium

$\phi$  = porosity

a = diameter of fiber

This relationship is accurate for porosities from 0.4 to 0.95, and applies to randomly arranged fiber lay ups [51]. There are also many other empirical relationships that relate permeability of a fibrous filter to its porosity and fiber diameter, all of which can provide a direct link between porosity and pressure drop [52]. Many of these empirical relationships are the result of computational fluid dynamics (CFD) simulations, which can calculate filter properties such as permeability, porosity, and pressure drop. Although the focus of this research does not go into CFD, much of the data collected and methods used will help ensure accuracy in future simulations. Understanding the dependence the governing equations have on porosity, it is now possible to investigate the methods used to measure ash accumulation and other modes of porosity reduction in SMF DPFs.

### 3 ADVANCED DIAGNOSTIC APPROACH

There is no prescribed definition of what “advanced diagnostics” are, but generally speaking, they refer to post-mortem analyses using advanced instrumentation and analytical tools. As it applies to the study of SMF DPFs, advanced diagnostics are utilized to help understand and quantify ash phenomenology and substrate properties. Specifically, these tools are:

1. Environmental Scanning Electron Microscopy (ESEM)
2. SEM Post-Processing Software (ImageJ)
3. Energy Dispersive X-Ray Spectroscopy (EDX)
4. X-Ray Fluorescence (XRF)
5. Focused Ion Beam (FIB)
6. X-Ray Computed Tomography (X-Ray CT)
7. X-Ray CT Post-Processing Software (VG Studio Max)

Many of these tools and others have been used to generate meaningful data in studying ash and substrate properties in porous ceramic DPFs [38, 40, 41]. However, there are material differences between a porous ceramic DPF and a metallic DPF as explained in *Section 2.1* and *Section 2.2*, so instrument settings must be adjusted to guarantee precise and accurate data collection. This section attempts to resolve those differences by outlining the procedures and instrument settings best suited for analyzing SMF DPFs. Also, this section outlines the fundamental understanding of the advanced diagnostic tools used. Some of the descriptions delve into the field of quantum mechanics, but this detail is necessary to illustrate what exactly is happening when the settings are changed. This detail further shows how the settings affect the sample, so that future researchers will give consideration to experimental decisions, instead of haphazardly choosing instruments settings that could either destroy the sample or skew the data.

The developed methods are the result of best practices and experimental iteration, which makes it easier to hone in on the ideal settings for data collection. While the following procedures and settings have seen improvement in advanced diagnostic techniques for SMF DPFs, they are by no means the optimal settings, and more research is still required in this area. It should be

established, though, that the optimal settings for data collection might not be practical with regard to experimental time and cost. Therefore, these procedures outline the first-generation approach to generating useful data in determining the effect of ash and substrate properties on porosity reduction and pressure drop in SMF DPFs.

### 3.1 Scanning Electron Microscopy (SEM)

Scanning electron microscopy (SEM) is a non-destructive advanced diagnostic tool used to produce nm-resolution images of an object. It is non-destructive in the sense that the same sample can be imaged multiple times, but the SMF DPF cartridge itself must be cut into smaller pieces to fit inside the chamber. The working principle behind SEM relies on the simultaneous scanning and detection of electrons that are emitted from the specimen. As seen in Figure 3.1.a., a high voltage electron beam is directed onto the sample using electromagnetic lenses, and the collision causes the discharge of various energy-intensity electrons, which are then captured by different detectors such as the secondary electron (SE) detector and the backscatter electron (BSE) detector [53]. Scanning the sample during this process and combining information from the incident electron beam with the electrons detected, creates a raster image, which displays topographical surface information of the sample on a computer screen [54]. The magnification and spatial resolution of SEM is about 20x to 30,000x and 50 to 100 nm, respectively [53].

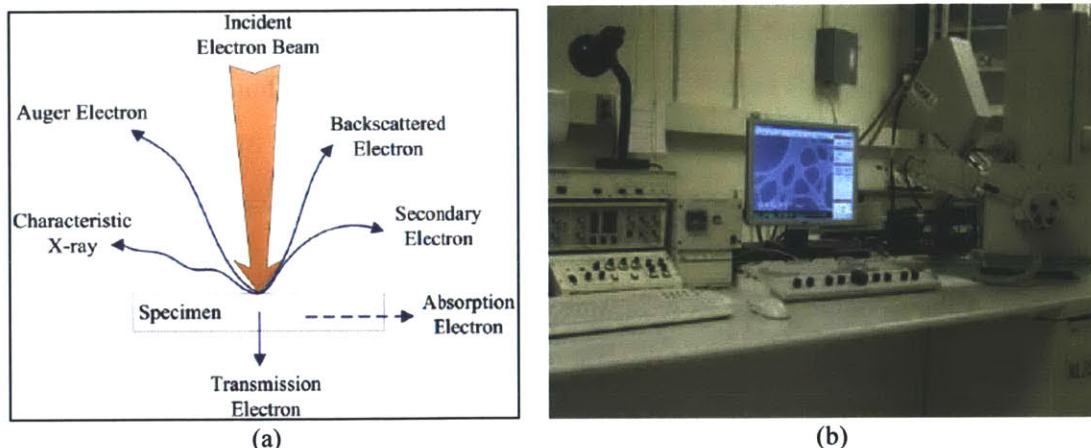


Figure 3.1. Fundamental principles of SEM, (a) and ESEM used at MIT's CMSE, (b) [55, 56].

The Environmental Scanning Electron Microscope (ESEM), shown above in Figure 3.1.b, is located at MIT's Center for Materials Science and Engineering (CMSE) and is used to study the

ash and substrate properties in SMF DPFs. ESEM works in accordance with the previously mentioned principles, but removes the need for sample preparation such as gold coating [53]. Gold coating is accomplished to make non-conductive samples conductive, but this distinction does not apply to SMF DPFs, as they are already highly conductive.

To ensure that the SMF DPFs and included ash are imaged correctly and under appropriate settings, it is important to first identify which detector to use. The SE detector provides enhanced topographical imaging of the sample and overall superior resolution with regard to the sample's texture, but has difficulty deciphering compositional differences between elements of contrasting color [57]. Therefore, the SE detector would show the filter and ash particles in similar gray-scale intensities. The BSE detector loses some of the desired geometrical characteristics of SE detection, but can distinguish compositional differences in the sample with higher accuracy [57]. Since SMF DPFs are alloys comprised of various metals, and ash agglomerates contain Ca, Mg, and Zn, the BSE detector is used as it produces higher quality images that show the differences between various constituent elements. The settings for attaining clear, high-resolution images of SMF DPF samples are described in Table 3.1 below.

<b>Setting</b>	<b>Value</b>
Detector	BSE
Accelerating Voltage	10.0 kV to 15.0 kV (ESEM) ≥ 15.0 kV (EDX analysis)
Spot Size	3, 4, or 5 (ESEM) 5 (EDX analysis)
Aperture Number	3 (100 μm diameter)
Vacuum Pressure	LOW VAC (0.7 - 1.5 torr)
Scan Time	< 3 hours
Magnification	2000x (ESEM) 800x (EDX)

Table 3.1. Experimental settings used for ESEM and EDX.

As Table 3.1 shows, the accelerating voltage varies between 10.0 kV and 15.0 kV. A general rule of thumb is to select the lowest voltage that will give the information needed, and these settings

give high-resolution images of both filter fibers and ash particles [58]. Typically, metals are imaged using higher voltages, but for longer scans of about 3-5 hours, higher voltages can distort the image. Even at 15.0 kV, the image brightness and contrast fluctuate with longer scan times, which necessitates the occasional change in voltage and spot size to reduce the effects of beam damage [58]. Figure 3.2 below shows the difference in image quality of a DPF fiber taken at the beginning of a scan versus the end of a 3-hour scan.

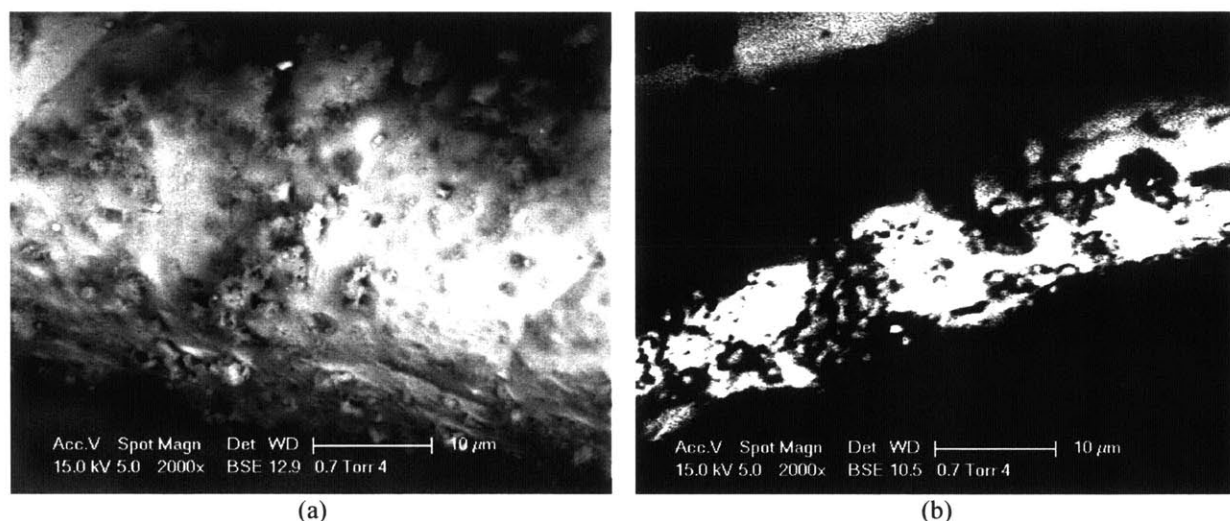


Figure 3.2. ESEM image quality at beginning of scanning, (a) versus image quality approximately 3 hours after scan, (b).

The spot size, which is the actual width of the electron beam that hits the sample, also has a significant effect on the image quality. An increase in spot size causes an increase in the current, but care should be taken not to provide too much current, as the image will suffer from beam damage as shown above [58]. Smaller spot sizes (1 or 2) are optimal for high-magnification work (>50,000x), but in analyzing SMF DPF features, these high-magnification levels are excessive [58]. For the SMF DPF analyses, spot size 5 is predominantly used because it gives a high-resolution, noise-free image, but 3 hours is the maximum amount of time useful data can be collected. Past 3 hours, the beam damage effects compound, and the image quality suffers irreparably. If more than 3 hours of data needs to be collected, spot sizes 3 or 4 should be used, as long as they are consistent for all filter samples.

Conversely, the aperture number indicates the width of the beam that leaves the electron gun, with larger aperture numbers indicating smaller beam widths, and thus an increased depth of

focus [59]. For imaging SMF DPFs at 2000x, aperture number 3 gives sufficient depth of focus. As with the previous settings, if image quality improves with other aperture numbers, they can be used as long as they are identical throughout the analysis.

The final two factors outlined in Table 3.1 are the vacuum pressure and the magnification. With vacuum pressure, the LOW vacuum mode is preferred because it yields a higher resolution image than HI vacuum mode. Magnification can vary depending on what specific feature is being investigated, but for much of the forthcoming analysis, 2000x magnification is used because of its high fiber and ash resolution. If any image analysis or post-processing is being done on the ESEM images such as particle counting, a standard, normalized magnification should be used.

## **3.2 ESEM Image Processing**

The image processing software, ImageJ, is used to determine the size and distribution of ash particles and agglomerates in SMF DPFs. ESEM 8-bit ( $2^8 = 256$  shades of gray) TIFF files are imported into ImageJ and various functions are used to both refine the image and analyze it. ESEM TIFF files are taken under the specifications provided above in Table 3.1 while trying to create as much contrast as possible between the ash and metal fibers. Creating high contrast allows ImageJ to more accurately recognize and quantify the ash particles. The detailed analysis process for ESEM images is described below.

ESEM images are first opened in ImageJ. The image's dimensions are calibrated by drawing a straight line over the scale bar and setting the "Known Distance" equal to the scale's distance (10  $\mu\text{m}$  in this case), as seen in Figure 3.3.a. Isolating and measuring certain aspects of the image requires "thresholding" the picture's gray-scale histogram to highlight the objects of interest. For example, to look at the ash primary particles in Figure 3.3.b below, the gray-scale value is set between 116 and 255. These values determine the gray-scale intensity of the pixels in an 8-bit image, with 0 corresponding to black and 255 corresponding to white. It should be noted, though, that thresholding is an approximate method, and the gray-scale values chosen are subject to change based on differences in image brightness and contrast. After thresholding, the pixels of the apparent ash particles are then converted to black, with all background pixels becoming

white, using the “Binary” command shown in Figure 3.3.c. Ash properties such as number and area are then determined using the “Analyze Particles” option. This process highlights the ash particles based on the area threshold that is selected, and gives a report describing the number and area of individual particles, shown in Figure 3.3.d.

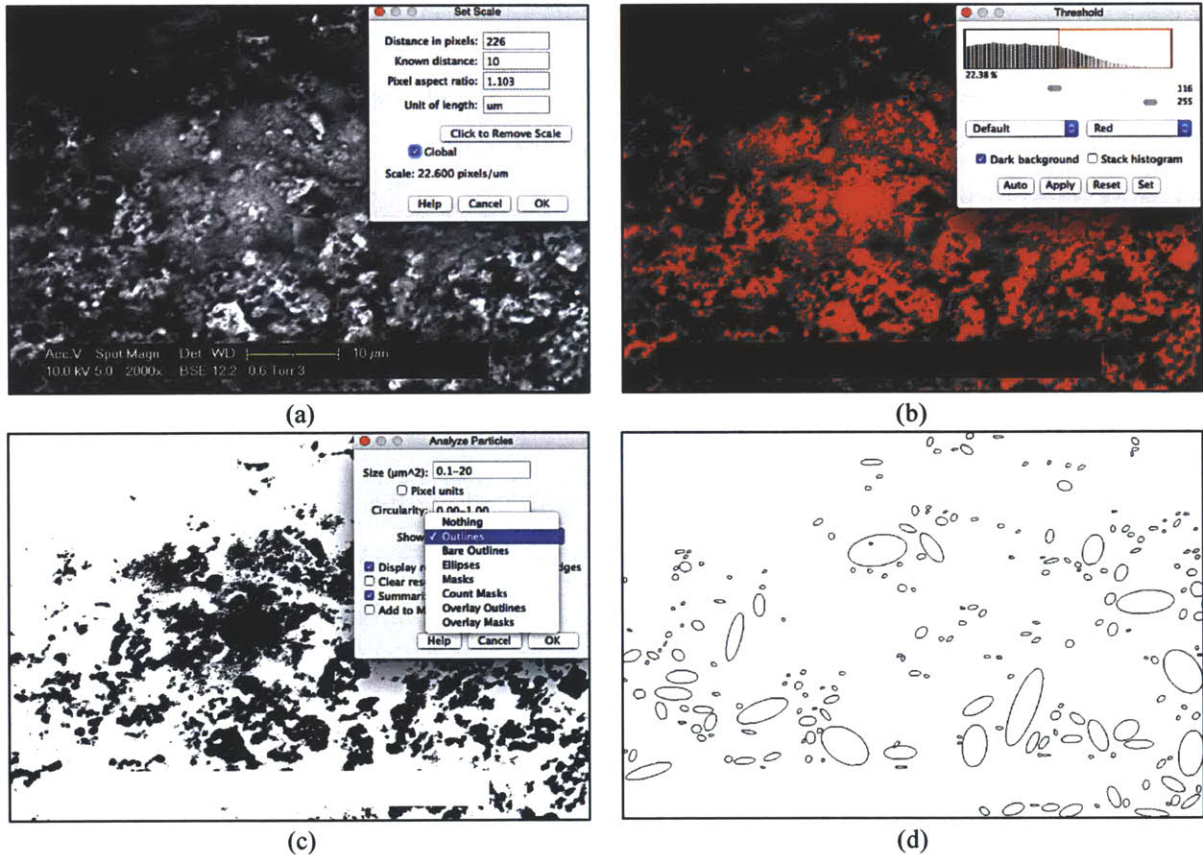


Figure 3.3. Scale set on ESEM image to analyze, (a); histogram threshold of ash gray-scale values, (b); binary command and identifying particle size of interest, (c); and circled ash particles, (d).

While ImageJ attempts to provide reliable ash size and distribution data, it does little with regard to understanding the compositional differences in ash. Therefore, another tool must be used to detect the elemental makeup of ash particles and agglomerates.

### 3.3 Energy Dispersive X-Ray Spectroscopy (EDX)

EDX is a method used to identify the chemical composition of a sample. In addition to detecting SE and BSE, many SEMs also capture the X-Rays emitted. This process works by analyzing the X-Ray energy that is emitted from a sample, when subjected to high voltages, and relating it to a

specific element. When the incident electron beam from the SEM hits the sample, it penetrates at a certain depth and displaces electrons at the inner orbital shells that are replaced by electrons in high-energy outer shells [60, 61]. This penetration depth, or spatial resolution is dependent on the accelerating voltage, critical excitation energy, and density of the sample, and is important to know in order generate the best X-Ray signal and output spectrograms [61]. Because the depth required to emit X-Rays is similar to the BSE escape depth, EDX analysis is best suited for use with the BSE detector [61].

The energies associated with the electrons in an atom's shell are very specific to an element, and the movement of electrons from outer to inner shell releases a characteristic X-Ray, which is then analyzed by the detector [60]. The inner orbital shells, like the K and L shell, are closer to the atom's nucleus and thus require more energy to displace the electrons [61]. This binding energy that is maintaining the orbital structure of the atom can be overcome knowing the excitation potential of the element being studied. For instance, if the element of interest is silver (Ag, atomic number = 47), then according to Figure 3.4.a. below, there has to be over 30 kV of voltage to remove an electron from the K-shell.

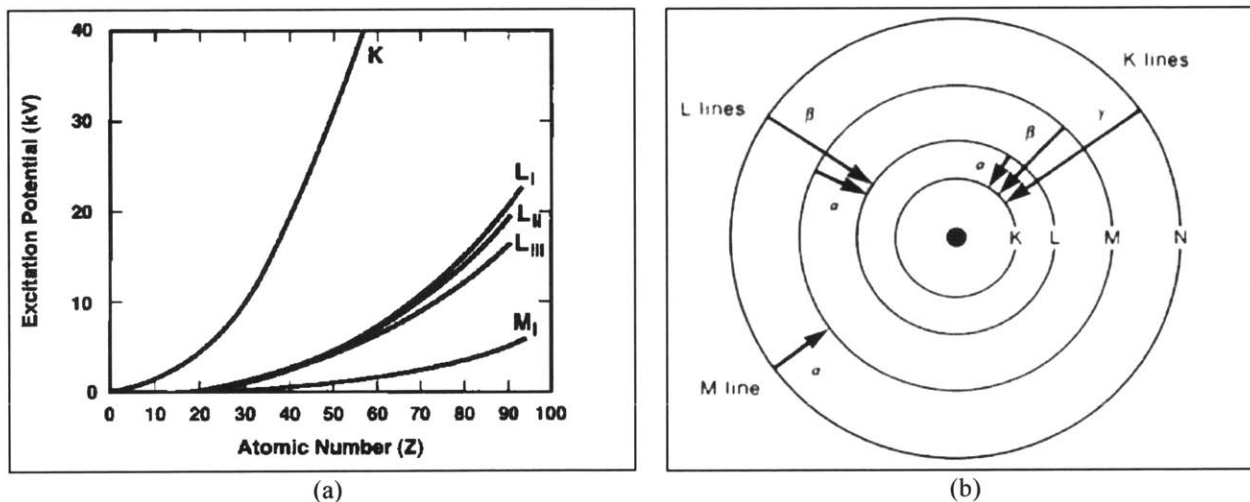


Figure 3.4. Excitation potential needed to displace an electron from specific orbital shell, (a) and illustration of orbital shells surrounding atom's nucleus, (b) [61].

A margin should be implemented when setting voltage levels of the electron gun, though. Typically 1.5 to 3 times the excitation potential is enough to displace an electron from an element of interest [61]. This principle is critical in determining the best settings for EDX

analysis. Given all of the elements in the ash particles and metal fibers, Zn is the heaviest, with an atomic number of 30. This corresponds to an excitation potential of about 10 kV, and using the “overvoltage” factor, anywhere from 15 kV to 30 kV is adequate to displace electrons from the K-shell of Zn [61]. Because EDX is used simultaneously with ESEM, the preferable settings should accomplish both SEM imaging as well as EDX analysis with a high degree of accuracy. Therefore, 15.0 kV is used as the best overall setting for SEM and EDX analysis.

In studying SMF DPFs, EDX is ideal for analyzing the various elements that are contained within ash agglomerates and identifying Al oxide layer growth in the fiber. There are a variety of techniques that can be used in the EDX software which give detailed compositional data of the SMF samples. The three useful data collection methods used are: spectrum analysis, element-mapping analysis, and point analysis.

A spectrum analysis determines all the elements that are present in the ESEM scanned image. For this reason, spectrum analyses can take a long time, but certain settings can be changed to ensure quick and accurate element detection. To make sure the output EDX spectograms are reliable, the dead time of the scan should be approximately 30% [62]. Dead time refers to the moments in the EDX analysis where the detector is analyzing and processing data, but not collecting X-Rays [62]. The ESEM voltage and spot size are two factors that affect the dead time of EDX data collection. An increase in the voltage or current of the incident electron beam will cause the dead time to increase beyond 30%. To make up for the dead time increase, the amp time can be increased, which preserves the high resolution. Amp time is a time constant used to optimize the signal processing of the X-ray events, and is by default a value of 3.84 [62]. The sample working distance is another ESEM property that can be changed during imaging to keep a dead time of approximately 30%.

The settings put forth thus far, 15 kV, spot size 5, and an amp time of 3.84, all result in a favorable dead time around 30%, and are adequate settings for attaining significant data. Also, the user can input the time of scan manually, with the options of 30, 50, 100, or more seconds. 50 seconds is determined to be a good compromise between data quality and collection time. The

increase in scan times decreases the percent error of the identified elements, but the difference is negligible.

Element-mapping analyses relate certain pixels in the ESEM image to a certain element. This is a crucial aspect of understanding where certain ash particles deposit in SMF DPFs. Also, it gives the user an in-depth knowledge about what different ash and soot particles look like when scanning SEM images. Figure 3.5 below shows a mapping scan of a field aged SMF DPF.

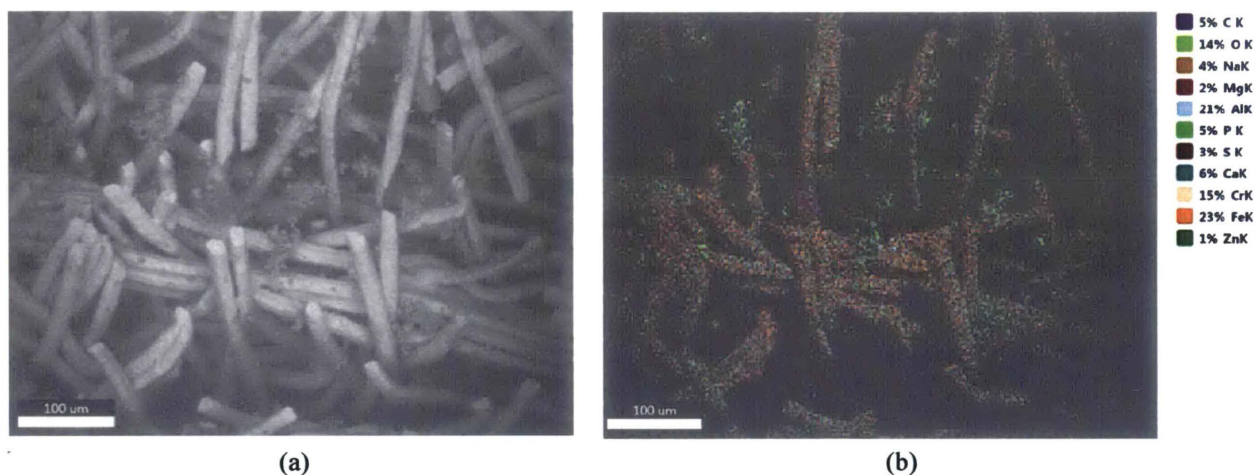


Figure 3.5. ESEM image of SMF DPF fibers and trapped soot and ash, (a) and EDX elemental mapping analysis of ESEM image, (b).

This technique can be very time intensive, though, with higher resolution scans taking on the order of hours. To solve this problem, some of the settings should be changed to improve the data quality and collection time. The settings of the spectrum analysis mentioned above are preserved in element-mapping analyses, but the additional settings that can be changed to expedite the data collection process are: Dwell time, Frames, Resolution, and Quality. The first setting that should be changed is “Quality,” and it should be set to “Manual,” which gives an estimation of the mapping analysis duration based on the inputs of the other settings. The “Dwell time” is the time length of data collection for each pixel in the image, and understandably, can increase the mapping analysis time. Similarly, “Frames” indicates the amount of passes that the detector will make over the ESEM image, with a doubling in frames equal to a doubling in the analysis time. Lastly, “Resolution” affects the mapping time simply by increasing the number of pixels that are in the image.

The properties of the filter and ash to be analyzed will dictate which process to use. If a very detailed analysis of the amount of Ca, Mg, and Zn is desired, then higher dwell time, frames, and resolution will provide sufficient data. But for most cases, which require qualitative analyses between aged filter samples, settings should be manipulated to yield a mapping analysis time of approximately 15-20 minutes; this is an acceptable compromise between mapping quality and experimental time. If there is already user knowledge about what ash and soot looks like in the filter, another method, such as point analysis, will provide higher resolution data in even a shorter amount of time.

The point analysis method allows for the isolation of specific points in the image to detect for elemental composition. This tool requires some knowledge of filter geometry and ash and soot phenomenology, and is not a broad-spectrum scan like the mapping analysis. The specific settings that are outlined in the spectrum and mapping analysis all apply to the point analysis as well. The only additional setting that can be changed to improve the quality of the scan is the resolution of the image. Increasing the resolution will increase the number of pixels and allow for more precise point selection. This is especially important in analyzing ash agglomerates, because the point size may be too big to determine the individual ash elements with a low resolution. The resolution selected for the point analysis scans is 1024 x 800, as it achieves an acceptable balance between timeliness and quality. An example of a point analysis and the resultant spectrogram is shown below in Figure 3.6.

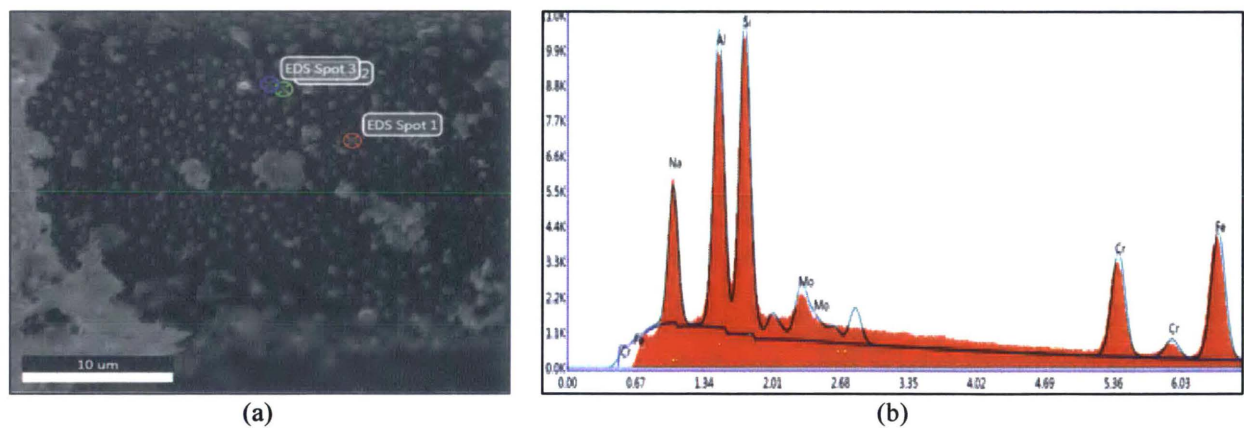


Figure 3.6. EDX point analysis of 3 areas of interest, (a) and resulting spectrogram of 1 area, (b).

Often times though, the use of EDX is limiting because it describes such a small area of the filter and does not give a complete understanding of the spatial distribution of ash and soot. Fortunately, other methods such as X-Ray fluorescence (XRF) exist, which can scan larger SMF DPF samples for major and minor components and help determine the deposition mechanisms of ash and soot on a larger, global scale.

### **3.4 X-Ray Fluorescence (XRF)**

XRF is another advanced diagnostic technique used to determine the elemental makeup of a sample. There are two primary methods of attaining fluorescent X-Rays from a sample: energy dispersive X-Rays (EDX) and wavelength dispersive X-Rays (WDS). Many XRFs rely on the principles of WDS, as it attains vastly higher working resolutions than EDX [63]. However, the resolution and accuracy of the WDS XRF translates into much larger data acquisition times and higher experimental cost. For this reason, EDX XRF (similar to principles in *Section 3.3*) is used to study the elemental composition of SMF DPFs.

The XRF instrument used is the Bruker Tracer-III SD Portable XRF located at MIT's CMSE. This handheld portable instrument operates similarly to the EDX gun on the ESEM, but does not have the flexibility to provide the range of current and voltage settings typical of ESEM. The scan energies range from 1 keV to 40 keV, with different settings tailored for analyzing specific elements [64]. As such, the spatial resolution of the XRF is less superior to that of EDX, making it ideal for the qualitative analysis of larger sample sets. For SMF DPFs, that means attaining reliable data on larger areas of the filter to better map out the spatial distribution of ash.

Because the ash elements of interest are Ca, Mg, and Zn, the instruments settings have to be adjusted to effectively identify them. This entails utilizing a titanium (Ti) filter, which is ideal for identifying elements like iron (Fe) and below on the periodic table [64]. Although this filter excludes Zn, it still can appear on the spectrogram. Additionally, the laboratory procedures dictate that the voltage and current be set to 15 kV and 55  $\mu$ A, respectively [64].

XRF can determine the difference in amounts of inlet versus outlet ash by scanning each side of the filter. Scans using XRF do not take very long ( $\sim$  2 minutes), and are ideal for gathering large

data sets in a short amount of time. An output XRF spectrogram of an SMF DPF is shown below in Figure 3.7:

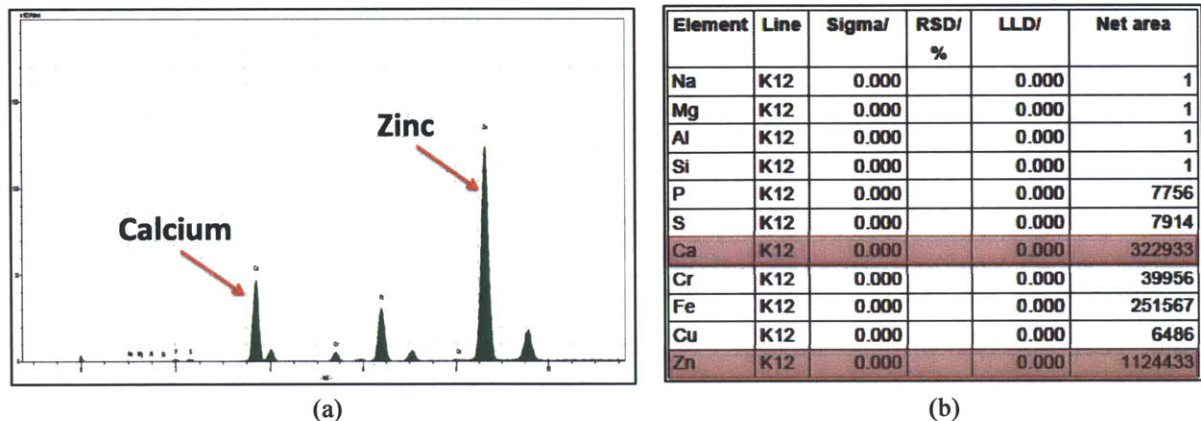


Figure 3.7. XRF output spectrogram, (a) and breakdown of constituent elements, (b).

While ESEM, EDX, and XRF are able to show ash, soot, and metal fibers in great detail, these tools do little to show how ash and soot actually attach to the metallic substrate. To understand the adhesive mechanisms of ash and soot on the metal fibers requires using another method.

### 3.5 Focused Ion Beam (FIB)

FIB is an advanced diagnostic tool that uses positively charged gallium ( $\text{Ga}^+$ ) ions to mill samples on a microscopic level. The instrument design is analogous to SEM, but instead of bombarding the sample with negatively charged electrons, larger, positively charged ions directed through electrostatic lenses collide with the sample and displace atoms, resulting in destructive localized milling [65]. The speed of the electron in SEM is almost 1,000 times faster than a  $\text{Ga}^+$  ion in FIB, but the mass of the  $\text{Ga}^+$  ion is over 100,000 times greater than the electron [66]. Consequently, the momentum of the  $\text{Ga}^+$  ion is enough to affect the atomic lattice of the sample, and displace atoms [66]. Similar to atomic binding energy discussed in *Section 3.3*, the incoming  $\text{Ga}^+$  ion possesses enough energy to continuously displace sample atoms until the ion's energy is reduced to a critical level and becomes implanted into the sample [65]. If the incoming accelerating voltage of the  $\text{Ga}^+$  ion beam is 20 keV and the binding energy of the atoms in the sample is 4 keV, then theoretically the ion would remove about 5 sample atoms before becoming implanted. In actuality, this process is not so simple as some of the energy is dissipated via heat

and electron emission. Figure 3.8.a below shows an illustration of the FIB's operating principles and Figure 3.8.b shows an image of FIB used on a metal fiber.

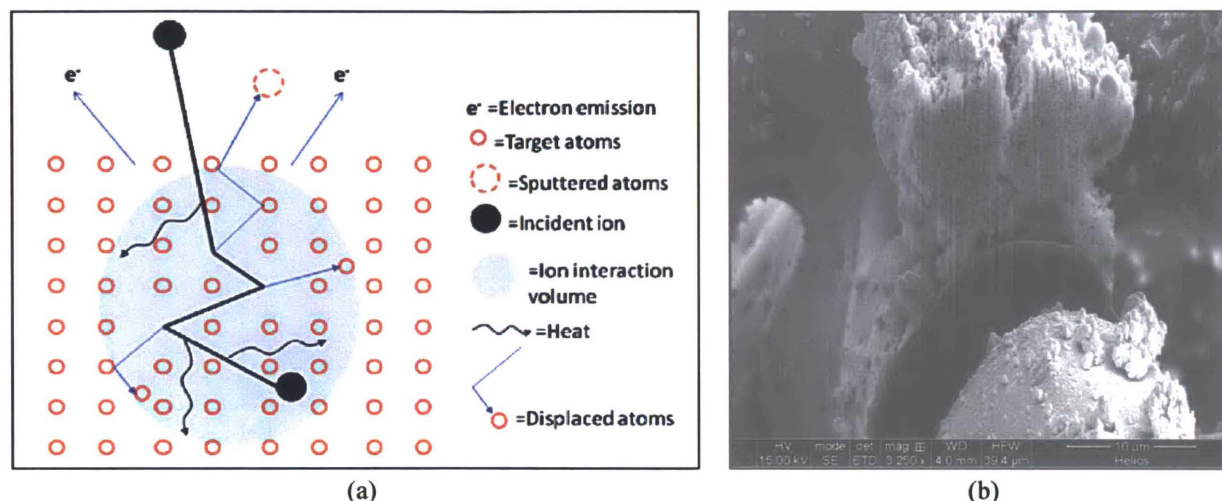


Figure 3.8. Fundamental principles of FIB sputtering, (a) and milled cross section of SMF DPF, (b) [65, 47].

This process is useful over a broad range of resolution, from 5-10 nm to 100-200  $\mu\text{m}$ , and is a good candidate for studying ash and soot primary particles as well as filter-ash interactions [65]. Many FIBs in use today are of a dual-beam design, meaning they are combined with the functionality of SEM. This feature makes it easy to switch between milling and imaging. The FIB used for analyzing SMF DPFs is a dual-beam FEI Helios 600 Nanolab located at MIT's CMSE. Much of the work done with the FIB focuses on ash and soot deposit mechanisms on the fibers and Al oxide layer growth on the fiber.

### 3.6 X-Ray Computed Tomography (X-Ray CT)

X-Ray CT is a non-destructive analytical technique that generates 3-D objects by imaging multiple 2-D slices of a sample at various orientations. This method works by placing a sample on a rotating stage and exposing the sample to X-Ray radiation, which produces varying intensity projections of the object onto an X-Ray detector located behind the sample [67]. Unlike SEM techniques that show pixels of a 2-D image, X-Ray CT works by scanning the 3-D "voxels" of the test sample and recording their intensity data on a 2-D projection, as can be seen in Figure 3.9. This data is then reconstructed using advanced computational algorithms into a 3-D object that can be further analyzed using post-processing software [67].

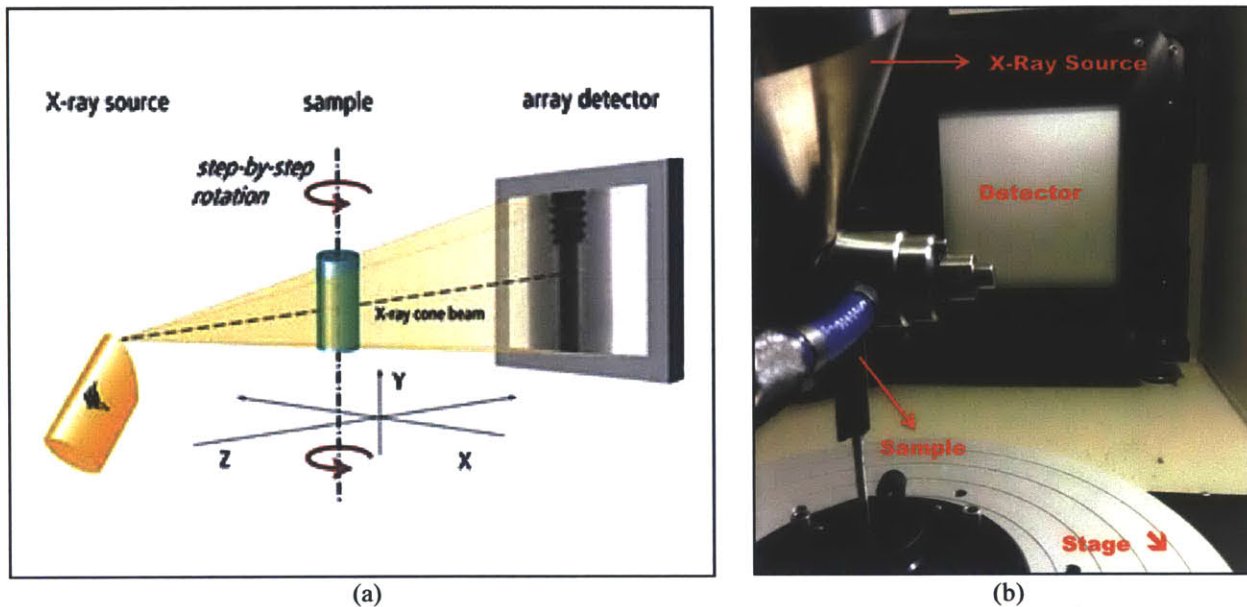


Figure 3.9. Fundamental principles of X-Ray CT, (a) and X-Ray CT used at Harvard's Center for Nanoscale Systems (CNS), (b) [68]

X-Ray CT has only recently been used in the lab to characterize the ash and substrate properties of DPFs. This advanced diagnostic tool is well suited for the field of engine after-treatment systems because it can show macroscopic, substrate-level details while still allowing for micron-scale resolution in analyzing ash properties. The specific X-Ray CT instrument used is the MicroCT ( $\mu$ CT) system located at Harvard's Center for Nanoscale Systems (CNS). The lab outlines the procedures used to ensure an optimal scan for most sample types. There are certain additional procedures, though, that should be considered in addition to those of the lab that provide better scan quality.

Because the metallic substrate of SMF DPFs is hard, an unfiltered scan can reveal “soft” X-Rays, which subtly distort the sample and provide less than optimal image quality. Attaching a metallic filter, such as a 0.1 mm Al filter, to the X-Ray source can help reduce those soft X-Rays and drastically improve the scan quality and resolution [69]. Also, it is advantageous to prepare small samples for X-Ray scans so that the specimen stage can be placed as close as possible to the X-Ray source. When an object is closer to the X-Ray source, it casts a larger image onto the detector, which affords the user the opportunity to zoom in further on the 3-D object and reveal more details [67]. This is especially important for SMF DPFs because ash can be seen more clearly in smaller samples. The SMF DPF samples prepared for X-Ray analysis are

approximately 5.0 mm x 10.0 mm x 1.5 mm test coupons, and they are placed at distances less than 20.0 mm from the X-Ray source. The current and voltage used for the scans are 117  $\mu$ A and 85 kV, respectively. It is important to keep the scan settings identical as it allows for better comparisons between clean and aged samples. Finally, at distances less than 20.0 mm from the X-Ray source, the focus should be adjusted to a value at or around -16 to give the highest resolution scan.

When it is time to actually scan the sample, the volume of interest should be chosen for a small piece of the filter to reduce the scan time as well as future reconstruction time. This practice also mitigates any edge distortion the sample might have undergone when it was being cut prior to scanning. As Figure 3.10 shows below, by choosing to reconstruct a small 338 x 337 x 340 voxel piece of the filter instead of the full 2,000 x 2,000 x 2,000 voxel filter, the computer memory required to open the file reduces from 22.35 GB to only 0.11 GB. This memory reduction proves critical when trying to manipulate the 3-D volume in post-processing software as well as running CFD simulations.

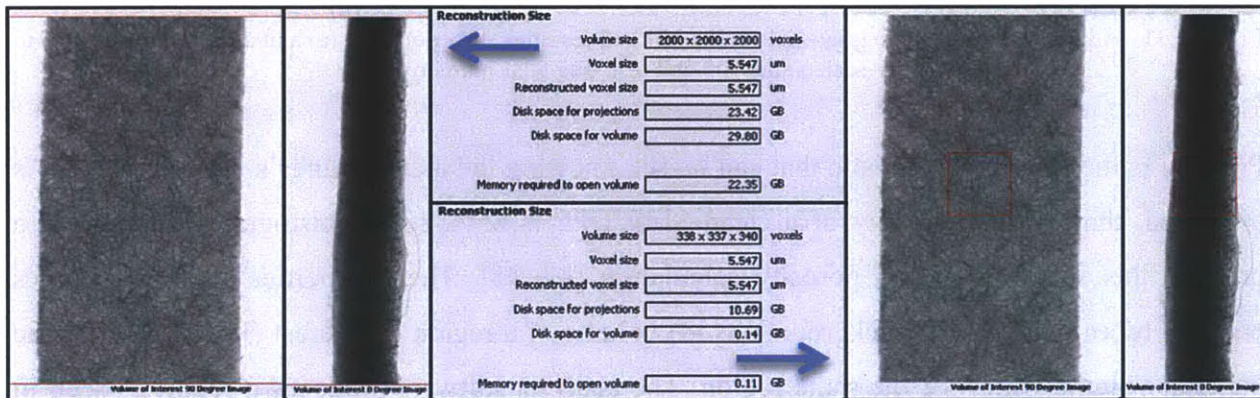


Figure 3.10. Reduction in X-Ray CT region of interest and resulting reduction in file size.

Once the scan is completed, a stack of 2-D slices is reconstructed into a volume file using the program, CT Pro 3D. The settings for reconstruction should be the same for clean and aged samples, which will allow for better comparison between sample sets. Therefore, no specific program settings will be explained, just as long as they are kept consistent for all scans.

### 3.7 X-Ray Post-Processing

Sophisticated post-processing software, such as VG Studio Max, is used to analyze many of the filter’s properties. Once the coupon is rendered in the software, user input is required to divide the sample’s characteristic gray-scale histogram into sections that accurately depict the filter. This process requires knowing some property about the filter that can be set by adjusting the histogram; it is not enough to set the gray-scale range based on what the filter looks like. Figure 3.11 below displays this concept by showing how the isosurface gray-scale values of the histogram can affect material properties of the filter, like porosity.

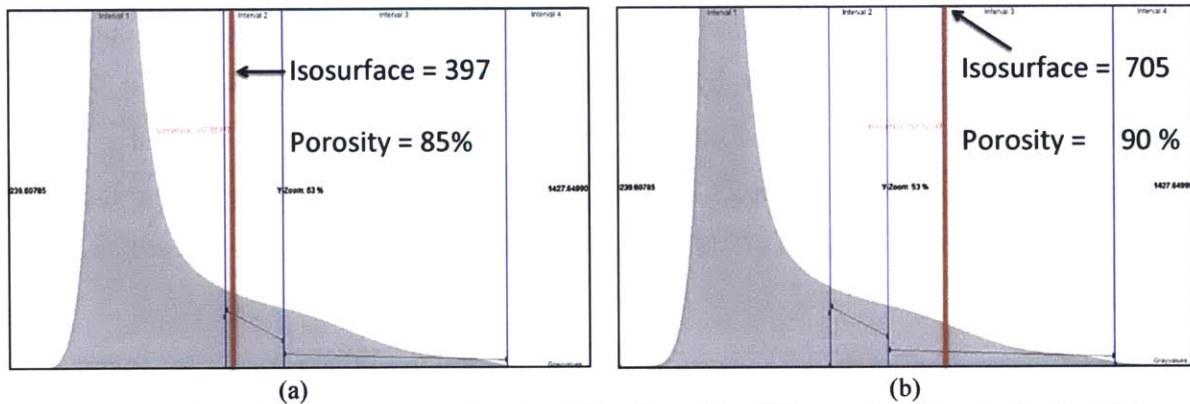


Figure 3.11. Adjusting histogram to gray-scale value 397 and resulting 85% porosity, (a) and adjusting histogram to gray-scale value 705 and resulting 90% porosity, (b).

Porosity is the filter characteristic that can be set, knowing the manufacturer’s average value. As discussed, the average porosity of a clean SMF DPF is 85%, so the histogram is adjusted to produce this value through a porosity calculation [47, 48]. The “Properties” tool determines porosity by calculating the background (void) volume of a region of interest (ROI) and then the material volume (filter) of the same region. The analysis software produces a report as seen in Figure 3.12 and porosity can then be determined using Equation 3.1 below:

<b>Object volume [mm<sup>3</sup>]:</b>	<b>0.321792</b>
<b>Total volume - object volume [mm<sup>3</sup>]:</b>	<b>0.168534</b>

Figure 3.12. VG Studio Max output report on porosity (34% porosity in this case).

$$\epsilon = \frac{\text{Total volume} - \text{Object Volume}}{\text{Total Volume}} \quad (\text{Eqn. 3.1})$$

Calculating porosity is the most widely used tool with regard to SMF DPFs as it has a direct impact on the pressure drop across the filter, as we have seen in Equation 2.6.

Another important feature of the software is the surface extraction option, which constructs a 3-D finite-element mesh out of the scanned sample. This mesh can be saved as various file types including: .STL, .IGES, and .STEP, which can be imported into most 3-D computer-aided design (CAD) software [70]. The significance of this feature is that it can provide enhanced object properties for running CFD simulations. Instead of the user creating an object mesh for the simulation, the actual filter can be substituted to provide more realistic and accurate measurement data. This is a critical aspect of modeling SMF DPFs because it would be virtually impossible to accurately design the random fiber orientations in a CAD program. An example of a rendered 3-D mesh of an SMF DPF is shown below in Figure 3.13.

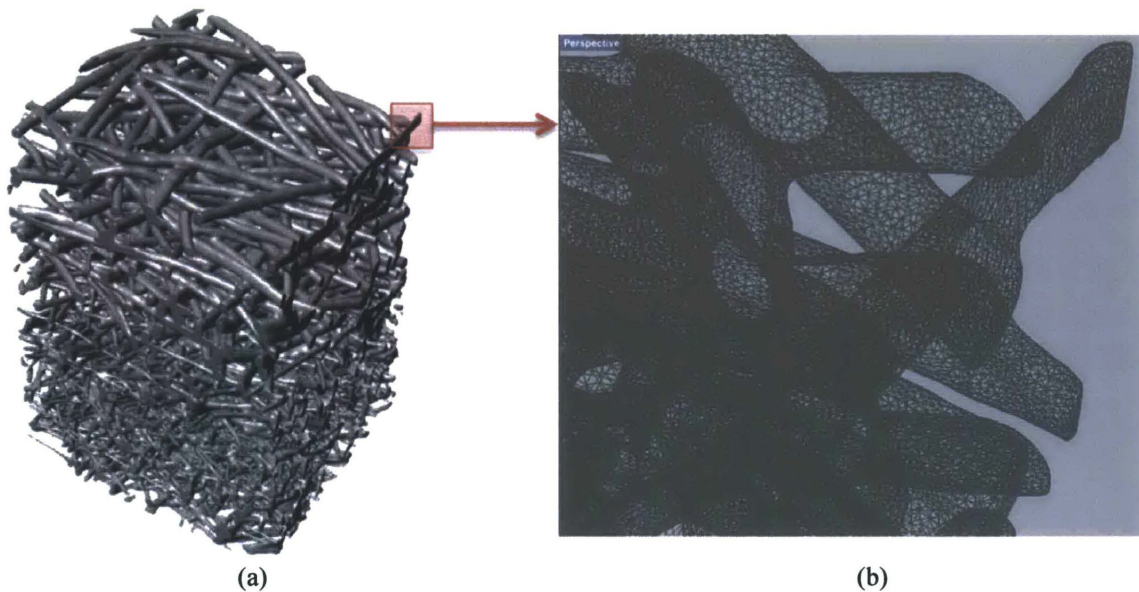


Figure 3.13. CAD rendered object of SMF DPF sample scanned using X-Ray CT, (a) and mesh of portion of SMF DPF, (b).

Now that the advanced diagnostic instrument settings and methods have been established and explained, it is possible to outline the specific procedures used to measure ash and substrate properties in SMF DPFs. Additionally, the sample history will be introduced to provide more information about the field-aged SMF DPFs. This sample information will eventually help create a statistical model relating the operational characteristics of the aged filters with the data collected using the advanced diagnostic tools described above.

(This page intentionally left blank)

## **4 EXPERIMENTAL PROCEDURES**

Since there is very little known about ash accumulation and distribution mechanisms in SMF DPFs, the experimental set up is designed to fill in the present knowledge gaps. The research focuses on identifying the following: (1) the difference between the fiber diameter of a new medium versus an aged medium in each layer of the filter, (2) the difference between elemental surface composition of a new medium versus an aged medium, (3) the extent to which ash bridges the pores in the medium, (4) the properties of ash particle size and agglomerate structure, and (5) the spatial distribution of ash trapped in the medium. The goal of this study is to see how these various parameters relate to an increase in pressure drop across SMF DPFs. Currently, there is no designed ash loading system, or any experimental method that can measure pressure drop across SMF DPFs. For this reason, pressure drop must be studied indirectly through filter porosity and empirical relationships.

To address the aforementioned topics, 4 different field samples are analyzed using the various advanced diagnostic techniques described in *Section 3*. Once the field samples are imaged and processed, statistical software is utilized to determine if there are any statistically significant trends in the data sets.

### **4.1 Sample History**

The 4 samples analyzed are all SMF DPFs used in off-road applications: 2 field samples are from a 2700-hour loaded salt mining vehicle, and the other 2 are from a 19000-hour loaded stationary power generating source. All samples came from 1 cartridge in the filter assembly, and both sets of samples were subject to both active and passive regeneration schemes. The engine used in the 2700-hour loaded samples was a 113-hp, 3.19 L Deutz diesel engine and the fuel used for the engine consisted of an approximate 50% B-99 blended biodiesel fuel. The engine used in the 19000-hour loaded samples was a 910-hp, 24.0 L Detroit Diesel with an unknown fuel. Additionally, the 2700-hour sample was subjected to approximately 5000 regenerations and the 19000-hour sample sustained about 12000+ regenerations.

## **4.2 Experimental Methodology -**

### **4.2.1 Fiber Diameter Determination**

The motivation behind this study involves investigating the process of fiber oxide layer growth and degradation within different regeneration schemes. The initial hypothesis, based on preliminary analysis, is that growth of the oxide layer causes flow restriction that can increase the pressure drop across the filter. Without an experimental testing apparatus, it is not possible to replicate this fiber oxide layer growth, but the mechanism of oxide growth is likely due to the high regeneration temperatures in the active regeneration case.

There are many different tools and methods that can be used to study fiber diameter growth. High magnification imaging allows the measurement of the fiber diameter directly using the ESEM's "Ruler" tool, which can determine differences between clean and aged filters. This method is used as a first approach, as it is relatively easy to do and is not time intensive. The difficulty with this method is that it is subject to user error, and also it cannot effectively differentiate between user error and manufacturing variance. For this reason, 40 measurements are randomly taken at each filter depth location (top-middle-bottom) for the 4 aged samples and then compared to the control: a clean, unused filter. The reasoning behind choosing the sample size of  $n = 40$  is to closely approximate the population, or the actual size of the fibers at each level [71]. Assuming the samples follow a normal distribution, a higher sample size provides more accurate data and higher confidence in results. To achieve a robust data set, it is necessary to use another method to determine the change in fiber diameter.

The  $\mu$ CT and X-Ray post-processing software, VG Studio Max, are used together to determine the changes in fiber diameter. Within the "Wall Thickness" Module of VG Studio Max, a color-coded cross section of an SMF DPF shows the size distribution of fibers at each level in the filter and reports statistical data in a histogram as seen below in Figure 4.1. This method works by algorithms detecting the distance between two surfaces, with the user inputting the "Search Angle," which is the angle at which the program searches for the opposite surface [70]. For the Wall Thickness analyses, a search angle of  $30^\circ$  is used, along with "High Encoding Precision," which ensures optimal precision, but increases computing time. This data gives average fiber

diameter, standard deviation, the minimum and maximum fiber thickness detected, and the analyzed sample volume. Unlike using ESEM, it can calculate the entire population distribution, and does not rely on a sampling analysis. Using this method, the fiber diameters are analyzed among the aged samples and compared to the clean sample. This process will show the effects of loading time as well as regeneration on the fiber diameter. Additionally, the standard deviation calculated for each sample using Wall Thickness analysis will serve to supplement variance data collected using the ESEM Ruler function.

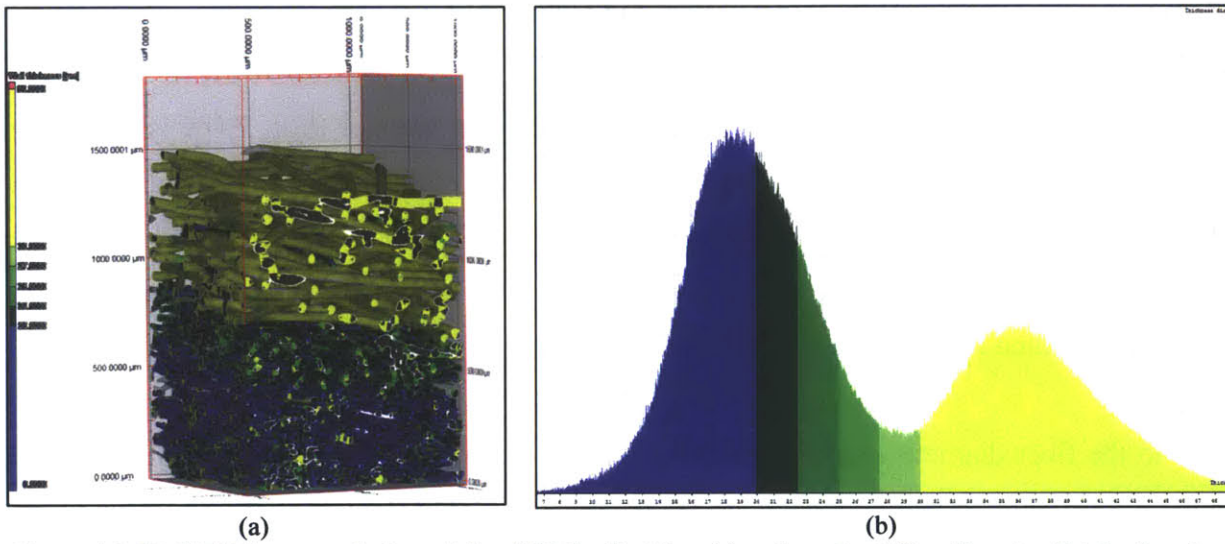


Figure 4.1. Wall Thickness analysis module of VG Studio Max, (a) and resultant fiber diameter distribution shown in histogram, (b).

## 4.2.2 Surface Composition of Fibers

The elemental surface composition of the fibers can reveal a lot with regard to the sample's operational history; the amount of lubricant-derived ash adhering to the fiber surface, the presence of oxide layer flaking, and the relative amounts of soot in the filter can indicate the type of oil used, regeneration mechanisms, and run-time. Knowing this, the main goal of this study is to understand how the composition of metal fibers can correlate to potential increases in pressure drop. Initial studies and ESEM imaging shows that the oxide layer grows to a critical size and then detaches from the fiber (see Figure 4.2), only to be caught downstream in the filter. It is hypothesized that this phenomenon may drastically reduce the porosity and cause an increase in pressure drop across the filter.

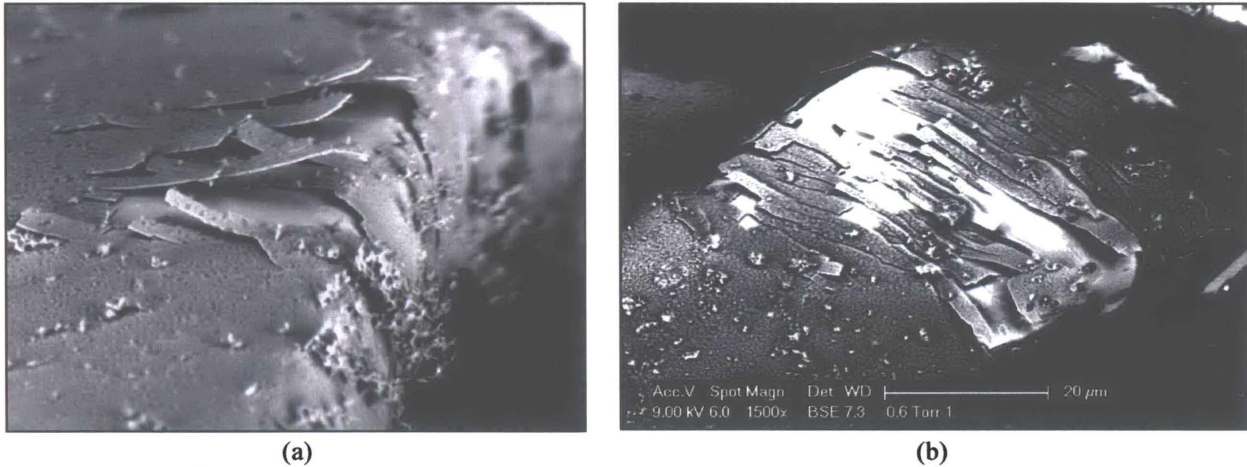


Figure 4.2. ESEM image of oxide layer detachment on fiber, (a) and resulting exposed metal of fiber (b).

To understand the effects of the Al oxide layer detachment on pressure drop, EDX is used. The relative amounts of Al are analyzed using EDX at each layer of the 4 aged filters and compared to the 5% aluminum content of Fecralloy in a clean SMF DPF [46]. Significant increases in the % Al output of EDX will indicate where the oxide layer is flaking and depositing in the filter. This analysis method relies on the settings outlined in *Section 3.3*.

Similar to the fiber diameter study, a sampling analysis is used. However, instead of taking 40 samples at each level, 40 samples total are taken across the full depth of the filter (14-top layer, 13-middle layer, 13-bottom layer). The reason for this is because EDX analysis takes longer than using the Ruler command on ESEM, and 40 samples at each level would not be experimentally practical. If there exists the need for more sampling due to excessive variance in EDX outputs, then more will be taken.

### 4.2.3 Porosity and Ash Bridging in SMF Pores

Unlike ceramic filters with clearly identifiable pores, SMF filters have no defined pores. The filters themselves are porous, but the porosity is not a function of the material, as is the case in cordierite or SiC DPFs. Rather, the porosity depends on the random geometrical lay up of the fibers in the X-Y plane, which allows space for “pores.” For the sake of simplicity, a pore in an SMF DPF is any location in an infinitesimally thin 2-D slice of the filter that has an overlap of 3 or more fibers, creating a polygonal shape as shown in Figure 4.3.b. This causes difficulties in mapping the pore network in an SMF DPF; therefore ash bridging can only be truly seen in a 2-D

case. But quantifying ash bridging is challenging in 2-D, so other properties that relate to ash bridging need to be measured.

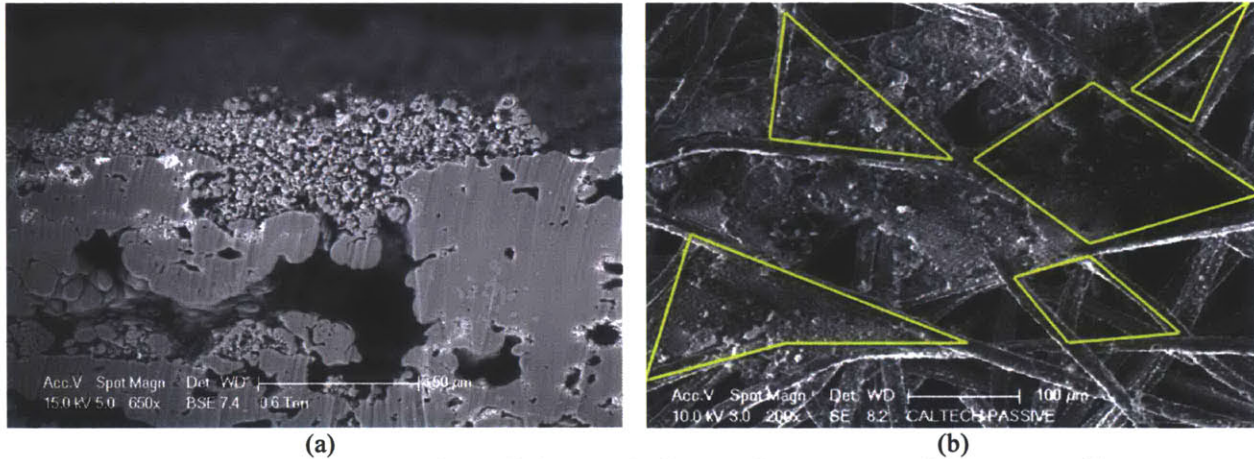


Figure 4.3. Pore structure in cordierite DPF [47], (a) and pore structure in SMF DPF, (b).

To accurately measure quantities that relate to ash bridging in SMF DPF pores requires knowing the main purpose of the study. The motivation behind calculating ash bridging in pores is to study the effect of how ash eliminates pore space and subsequently clogs the filter, causing flow restriction. Determining the direct extent to which ash bridges in the SMF DPF pores relies on collecting many data points between various advanced diagnostic instruments including ESEM, FIB, and other tools. Using these tools, the data collected would show microscopic levels of ash bridging which are subject to high amounts of variability. Therefore, a broader approach to examining ash bridging will provide more telling data.

Measuring the change in filter porosity using  $\mu$ CT and VG Studio Max can help effectively determine the extent of ash bridging across the pores in SMF DPFs. In keeping with statistical best practices, 15 core samples are taken at each level of the 4 aged filters, and their porosities are compared to the clean SMF DPF porosities. If excessive variance is detected in the 15 samples, more will be taken to ensure higher levels of confidence in the data. All settings used to conduct the analysis are described in *Section 3.7* and remain the same when scanning each sample, aged or clean. Figure 4.4 below shows what core samples of an aged SMF DPF look like at the 3 different layers, and their resultant porosities.

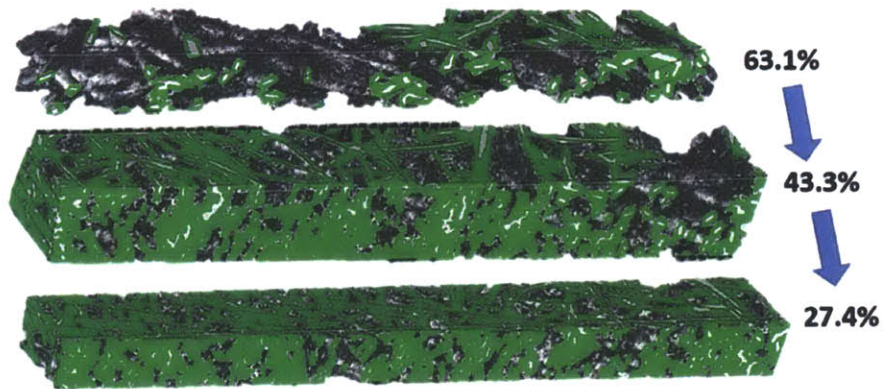


Figure 4.4. Core samples of SMF DPF at top, middle, and bottom layers and resultant porosity [47].

It should be reiterated that reductions in filter porosity are not solely a function of ash bridging between the pores. As described above, fiber oxide layer growth also may contribute to large reductions in porosity, especially in the lower layers of the filter. This means that total reductions in porosity cannot be completely attributed to ash bridging, so the actual extent of ash bridging has to be isolated in its effect on pressure drop. An in-depth analysis of what constitutes ash bridging in the pores, ash primary particles and agglomerates, is required to understand how ash removes filter space.

#### 4.2.4 Ash Particle Size and Agglomerate Structure

Whereas the ash bridging analysis provides a broad scope of resolution, an ash particle and agglomerate size study discretizes that process by measuring and counting each individual particle and agglomerate. The purpose of this study is to weigh the contribution of particles and agglomerates to overall changes in porosity at each level of the filter. Additionally, the aim of this research topic is to determine if run-time and regeneration strategy contribute to the evolution of ash particle size and agglomerate structure.

To understand the particle size of ash in an SMF substrate requires thorough image analysis using ESEM and ImageJ software. A sampling analysis is conducted following suit with the previous analyses of taking  $n = 40$  samples from each depth location in the filter. This process is completed only for the 4 field-aged samples, as the clean sample does not contain any ash or soot. The entire process of taking 40 samples at 3 levels of each of the 4 aged filter results in a

large data set of 480 images. This robust data set will help provide a high level of confidence in the results. Additionally, the ESEM images are all recorded at the same 2000x magnification (62.5  $\mu\text{m}$  by 46.8  $\mu\text{m}$  image) level in order to keep the ash count limited to a specific default space. All other settings used for the analysis are described in *Section 3.1* and *Section 3.2*.

After the raw imaging data is collected with ESEM, ImageJ is used to analyze the size of ash particles with the “Threshold” and “Analyze Particles” functions previously described. Numerous iterations reveal that a majority of ash particles fall in the area range of 0.1  $\mu\text{m}^2$  to 20  $\mu\text{m}^2$ ; anything below that range is dominated by noise particles, and anything above represents ash agglomerates. Due to long scan times, noise particles from image damage and imperfect thresholding are prevalent. To remove noise particles, the “Despeckle” command is used as appropriate. Despeckle is an image filter in ImageJ that works by taking an average of the pixels surrounding the noise pixel and replacing it with that gray-scale value [72]. Therefore, if one black pixel with gray-scale value 0 is surrounded by 8 white pixels of gray-scale value 255, the black pixel will be replaced by a pixel of average value 226.67. This process is represented in Figure 4.5 below.

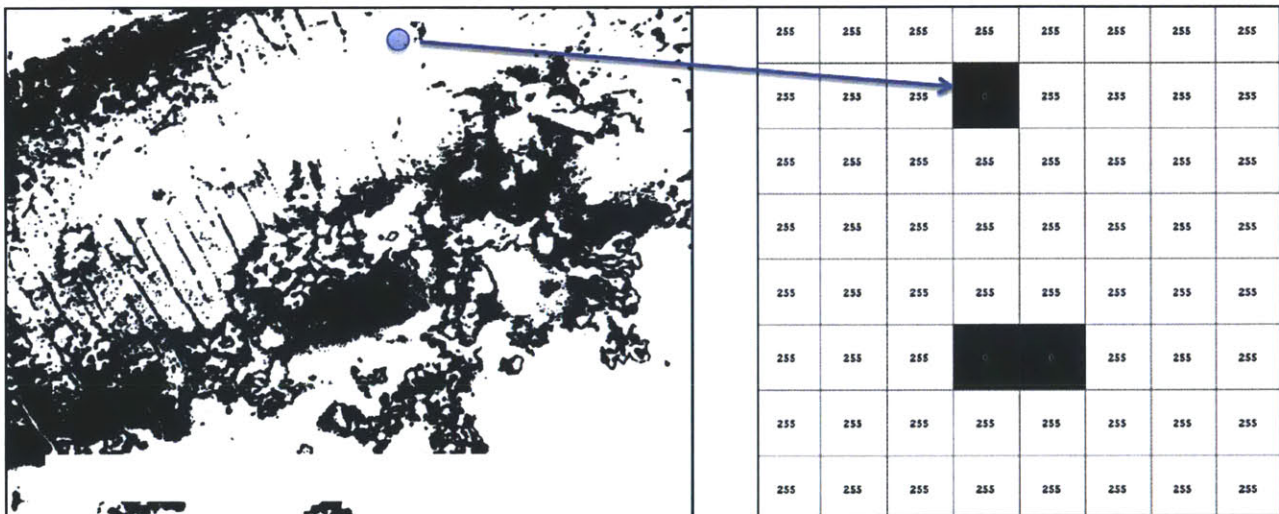


Figure 4.5. Despeckle filter isolating noise particles and converting to background.

After the “Binary” image is refined and removed of any noise particles, the particle analysis reveals all groupings of pixels falling within the 0.1  $\mu\text{m}^2$  to 20  $\mu\text{m}^2$  range and gives their average gray-scale value and area. The ash primary particles are assumed to be spherical; therefore their

diameters can be extracted from the given area. These results are then compiled and analyzed using the statistical methods described at the end of this section. To ensure that the ash primary particles fall within appropriate sizes, Table 4.1 below serves as an outline for the different ranges in diameter of ash particles in various studies.

Source	Particle Size ( $\mu\text{m}$ )
SAE 2000-01-1016	$d_{\text{eff}} \sim 0.5 - 2.0$ , range $\sim (1-10)$
SAE 2001-01-0190	$d_{\text{primary}} \sim 0.1 - 0.5$
SAE 2004-01-0948	2.4 – 37.6
MECA 2005	5-50
SAE 2005-01-3716	0.4 - 8
SAE 2006-01-0874	1

Table 4.1. Compilation of ash particle sizes from various sources [73, 74, 75, 76, 77, 78], Adapted from [38].

This information does not verify that the developed process for measuring ash particle size is completely accurate, but it does provide an appropriate range of ash primary particle sizes. Observing multiple data points outside of this range would have severe implications for the trustworthiness of the data collection method.

The process used for analyzing the size of ash agglomerates is slightly different. It is difficult for ImageJ to separate the fiber surface from the ash agglomerates, and automatic thresholding tends to neglect large portions of the ash agglomerate structure. To account for the whole ash agglomerate, the “Spray Can” tool is used, with the user highlighting the extents of the ash cluster. After the agglomerates in the ESEM images are identified, they are subject to the same method as the ash primary particles, except the area of interest is the  $20 \mu\text{m}^2 - \text{Infinity}$  range.

## 4.2.5 Spatial Distribution of Ash

The depth-wise spatial distribution of ash in SMF DPFs can be derived from the analysis reports that ImageJ produces for particle and agglomerate size. ImageJ gives the number of ash particles and agglomerates that are in each TIFF image, and after analyzing 40 images at each filter level, the spatial distribution of ash can be determined. This method is limiting in that it attempts to

summarize ash deposits over an entire cartridge by small coupon samples, so it must be researched using another method.

Instead of analyzing the filter cross sections, XRF is used to analyze X-Y direction inlet versus outlet ash amounts in SMF DPFs. This process involves cutting 4 samples of each filter into larger, approximately 2.0 cm by 2.0 cm squares and subjecting both sides to X-ray fluorescent radiation. The output spectrogram shown in Figure 3.7 summarizes the elements in the coupons and gives the count number of X-Rays for each element. The main purpose of this experiment is to understand the relative differences in ash between the inlet and outlet side of the filter. Although this experiment fails to quantify the ash buildup in the middle layer of the sample, it will help strengthen the data collected in *Section 4.2.4* for the top and bottom layers on a larger scale.

## **4.3 Statistical Procedures -**

### **4.3.1 Statistical Techniques**

The procedure for understanding the impact of ash and fiber oxide layer growth on porosity relies heavily on sampling. The reliability of the sample data collected is negated if statistical rules are not adhered to. Therefore, a procedure for establishing trends within the data is essential to studying the relationship between porosity and the parameters explained above. By calculating the statistical significance of the above parameters through multiple regression equations and screening experiments, it is possible to identify the variables that have the largest effect on reducing filter porosity and pressure drop. This information then identifies with a certain level of confidence what parameters should be manipulated in the operation and design of SMF DPFs.

The basic sampling procedures for each research topic are the following:

1. Collect  $n = 40$  samples (ESEM images, EDX graphs, etc.) using advanced diagnostic equipment.
2. Analyze relevant parameters from raw data; discard any samples that have poor image quality, or were taken under poor conditions.

3. Graph data points on a normal quantile plot to determine if normality assumption is valid (See Figure 4.6.a.).
4. Re-analyze any data points that are extreme outliers ( $> 3x$  inter-quartile range).
5. Substitute new data from Step 4, if applicable.
6. Remove any existing extreme outliers (See Figure 4.6.b.).
7. Graph new data set to determine normality assumption (See Figure 4.6.c).
8. If data assumes a normal distribution, accept the data and provide 95% confidence interval results of specific parameter.

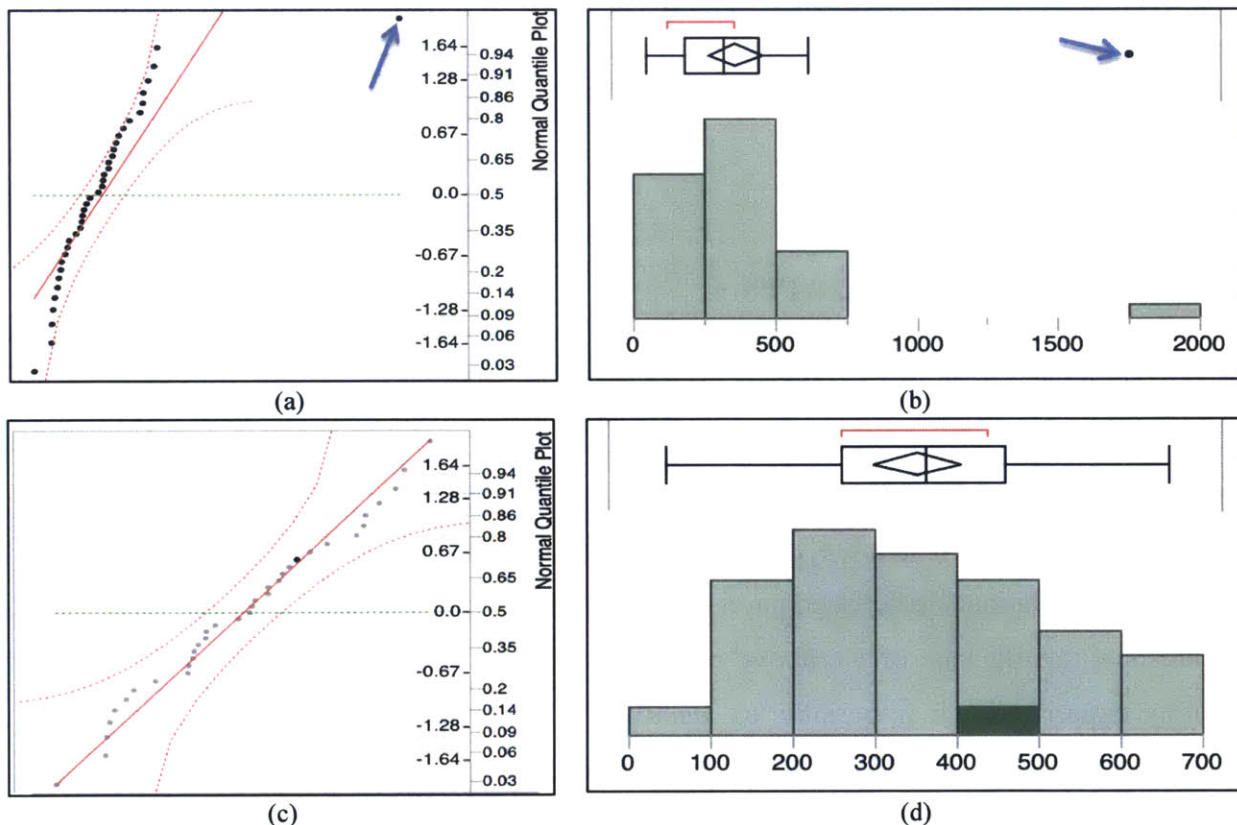


Figure 4.6. Plotting initial data set on normal quantile plot, (a); identifying extreme outliers in data set, (b); removing extreme outliers and plotting again, (c); and verifying normality assumption of data, (d).

It is imperative to understand the distribution of data points in the sample set. The raw data cannot be forced into a normal distribution by unnecessarily removing outliers, as this would skew the results of any confidence interval. If the statistical procedure results in removing too many outliers, the study is stopped.

### 4.3.2 Parameter Screening

A summary of the parameters that the experimental methodology captures in addition to data provided on the samples is listed below (provided data in italics):

- *Run Time*
- *Layer*
- *Regeneration (None, Active, Passive)*
- *Number of Regenerations*
- Average Diameter of Fiber
- Percentage of Aluminum
- X-Ray counts of ash elements - XRF
- Number of Ash Primary Particles
- Average Diameter of Ash Primary Particles
- Number of Ash Agglomerates
- Average Area of Agglomerates
- Filter Porosity

Because filter porosity is most directly related to pressure drop through empirical equations, it is the established response. All other parameters are the factors that have an effect on the porosity in SMF DPFs, but the degree to which they reduce porosity is currently unknown. To understand the magnitude that each regressor has on the response, screening experiments must be conducted to understand the full effect of what influences pressure drop the most. To accomplish this, statistical software packages such as JMP Pro 11 can analyze multiple effects and determine which ones should be placed in the model. The software also gives the analysis of variance (ANOVA) for the regression formula and determines its statistical significance.

After all the data is collected using the experimental methodology, the parameters are screened for statistical significance and then placed in a multiple regression model. If other parameters are seemingly significant with research, such as % Ca in ash, they will also be included to determine their effect on porosity; the list above is not exhaustive. This methodology of attaining large data sets for multiple variables is used primarily because the research of SMF DPFs is new. It is a

reliable first-order approach to record every data point that is collected, and filter it through objective, mathematical programs that list its statistical significance. It would be difficult to try to understand the effects and interactions of the parameters on porosity from a theoretical viewpoint, because there are so many variables. The following results and analysis will show what parameters are deemed significant in their effects on porosity, and will serve as a good focal point for future research.

## 5 RESULTS AND ANALYSIS

The following results use the advanced diagnostic techniques explained in *Section 3* and address the 5 research topics outlined in the experimental methodology portion of *Section 4*. The samples analyzed are described in *Section 4*, and are all compared to a baseline clean sample to show how the ash and filter substrate properties change with loading. The final portion of the results attempts to develop a statistical model that predicts porosity in the filter as a function of the sub-parameters analyzed.

### 5.1 Fiber Diameter Determination Results

The purpose of the fiber diameter study is to determine the effects of oxide layer growth in filters as a result of aging and to eventually measure its result on porosity and pressure drop. 40 or more samples are randomly taken from each depth location of the filter and manually measured using the Ruler function in ESEM's Microscope Control program. The results of the fiber diameter study are shown below in Figure 5.1:

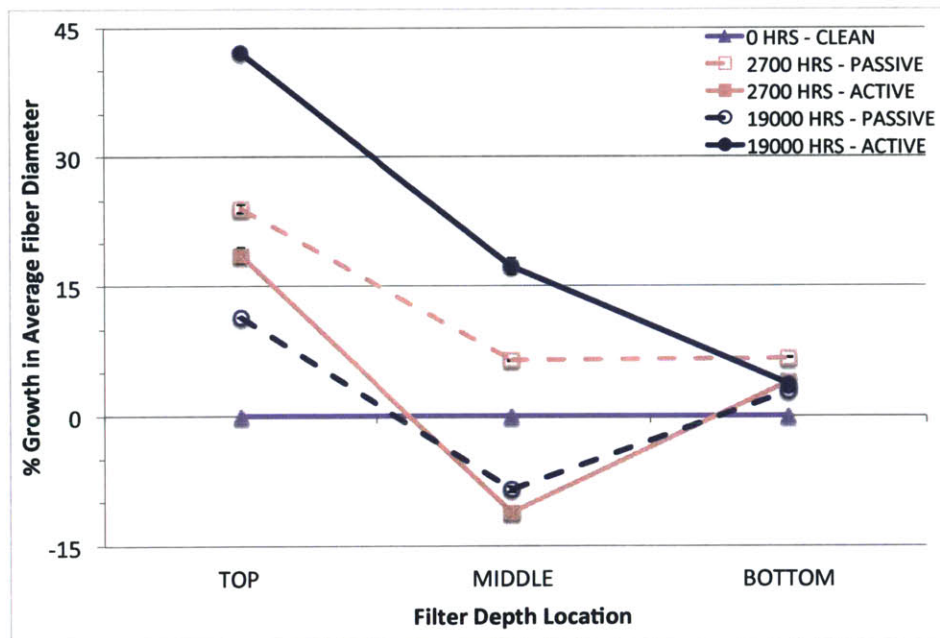


Figure 5.1. % Fiber growth (ESEM) vs. Filter Depth Location.

Although there appears to be no consistency between fiber growth and filter depth location at each level, certain levels of the filter display trends among the samples. For example, in each

aged sample, the top level of the filter experiences the most fiber growth, while the bottom fibers consistently see the least amount of absolute change. The fact that the 19000-hr active sample has 42% growth in the top fibers and only about 4% growth in the bottom fibers helps support the theory that run-time, regeneration mode, and the number of regenerations have a significant effect on the size of the fibers, more so in the top level of the filter than the bottom level. Additionally, the 2700-hr active sample has approximately 19% growth in the top fibers and 4% growth in the bottom fibers, likely due to less run-time and regenerations.

Between regeneration modes, the 19000-hr active sample has more fiber growth at each level of the filter than its passive counterpart. This is a logical trend, as the high temperature of regeneration would serve to expedite the corrosion and thus growth of the Al oxide layer. However, this trend is not evident in the 2700-hr samples, as the passive case has an average 8% higher growth than the active case. A possible reason for this contradiction may be that the 2700-hr samples have not been aged or regenerated enough to attain steady fiber growth. Excluding the middle fibers of the filter, the 2700-hr active sample is relatively similar to the 2700-hr passive sample. It is the middle level of the filters, though, which causes a large discrepancy between the sample sets, and it should be analyzed further.

In both the 2700-hr active and 19000-hr passive samples, the middle fibers of the filter experienced an 11% and 8% reduction in fiber diameter, respectively. Understanding that the purpose of the Al oxide layer on the FeCrAlloy fibers is to protect the base metals, it seems plausible that the reduction in fiber diameter may be due to severe degradation of the Al oxide layer causing corrosion of the underlying Fe and Cr. After the Al oxide layer has been completely shed from the fiber, the corrosive nature of exhaust gas would deteriorate the base metal and cause the fiber diameter to shrink. If there does exist a “critical” size at which the Al oxide layer grows and then detaches from the fiber, then this phenomenon may explain what happens to the remaining base metals of the fiber.

One noteworthy aspect of this study not shown in Figure 5.1, is the standard deviation associated with each fiber diameter group. The top and middle layers fluctuate between higher and lower standard deviations, but the bottom layer consistently has the least variation in fiber diameter

size for each case. This is possibly due to the smaller oxide layer growth to fiber diameter ratio seen in the bottom fibers of the filter. The 19000-hr active sample has 42% growth on the top fibers that have an average clean diameter of about 35- $\mu\text{m}$ , whereas its bottom fibers have about 4% growth on an average 15- $\mu\text{m}$  diameter. This accounts for a 1.2% growth per  $\mu\text{m}$  for the top fibers and only a 0.27% growth per  $\mu\text{m}$  for the bottom fibers. Essentially, the growth mechanism in the bottom fibers is more consistent with its low manufacturing variance than actual fiber growth, so it consistently has smaller variance in its fiber diameter. There are possibly other reasons for this phenomenon, but when fiber growth is significantly greater in one level of the filter than another, it may be due to unequal heat transfer from active regeneration, which would cause very different ash and substrate properties at each fiber level.

To test the validity of the above results, the Wall Thickness Module of VG Studio Max is used. The advantage to using this tool is that it provides a population distribution of the fiber diameters instead of a sampling analysis, with the aim of yielding more definitive results. The results of the Wall Thickness analysis are shown below:

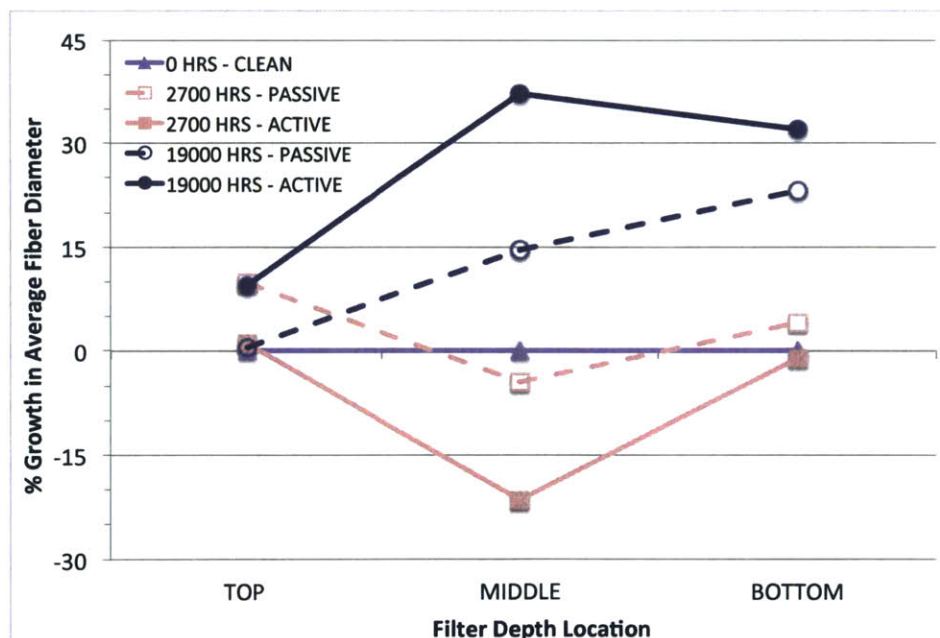


Figure 5.2. % Fiber Growth (Wall Thickness Module) vs. Filter Depth Location.

Similar trends appear in the Wall Thickness Module as were witnessed using the Ruler function. Again, on average the 19000-hr active sample has noticeably larger fiber diameters than the

19000-hr passive sample, supporting the original hypothesis of oxide layer growth within the active case. This data, though, shows the opposite trend in the distribution of fiber growth, with the 19000-hr active sample generally increasing in fiber growth as a function of filter depth.

Also, the 2700-hr passive sample has larger fiber diameters than the 2700-hr active sample at all levels of the filter, seemingly opposing the hypothesis. This same trend was shown in Figure 5.1, and again the difference may be attributed to shorter run-times and less regenerations. The last significant aspect of the data that is upheld in both analyses is the standard deviation of the bottom fibers. Again, the bottom fibers of the SMF DPF have the least amount of variance. This is consistent in all samples despite larger growth in the 19000-hr bottom fibers, but it contradicts the previous assumption that unequal heat transfer is the cause for smaller growth rates in the bottom fibers.

It is certain that the Wall Thickness Module is including both ash and Al oxide fragments when it analyzes fiber diameter. If the Al oxide layer does in fact peel off the fiber to become stuck in the bottom fibers of the filter, then the variance associated with fiber diameter would include these species and skew the fiber growth data. As such, it is likely that the bottom fibers indeed have the lowest variance in fiber diameter, but the amount of fiber growth in this study is questionable.

The initial goal of this study was to quantitatively measure the fiber diameters at each level of the SMF DPF and determine how it relates to run-hours and regeneration scheme. This data would then be correlated to measured decreases in porosity, and thus a relationship between run-time or regeneration and pressure drop could be reached. While many of the same trends appear in both the ESEM and Wall Thickness studies, the Wall Thickness Module is likely a less accurate depiction of the fiber diameter distribution of an SMF DPF, due to its probable inclusion of ash and Al oxide species in its measurements. For this reason, it will not be considered as an essential parameter in the statistical model. To better understand the effects of fiber oxide growth, a qualitative EDX analysis of the Al levels at each level in the filter may help.

## 5.2 Surface Composition of Fibers Results

The results of the surface composition experiment are shown below in Figure 5.3. The study consisted of running EDX scans to identify the % Al at the top, middle, and bottom layers of the filter in accordance with the sampling procedures outlined in *Section 4* and the settings defined in *Section 3*. As mentioned, the standard ESEM image size used for the EDX analysis was 800x. Also, the standard deviation and 95% confidence interval results were attained for the EDX measurements to ensure that there was no statistical overlap in the data sets. All of the recorded EDX readings were then compared to the baseline clean SMF DPF sample, with its marketed 5% Al chemical composition existing predominantly on the surface of the fiber [47].

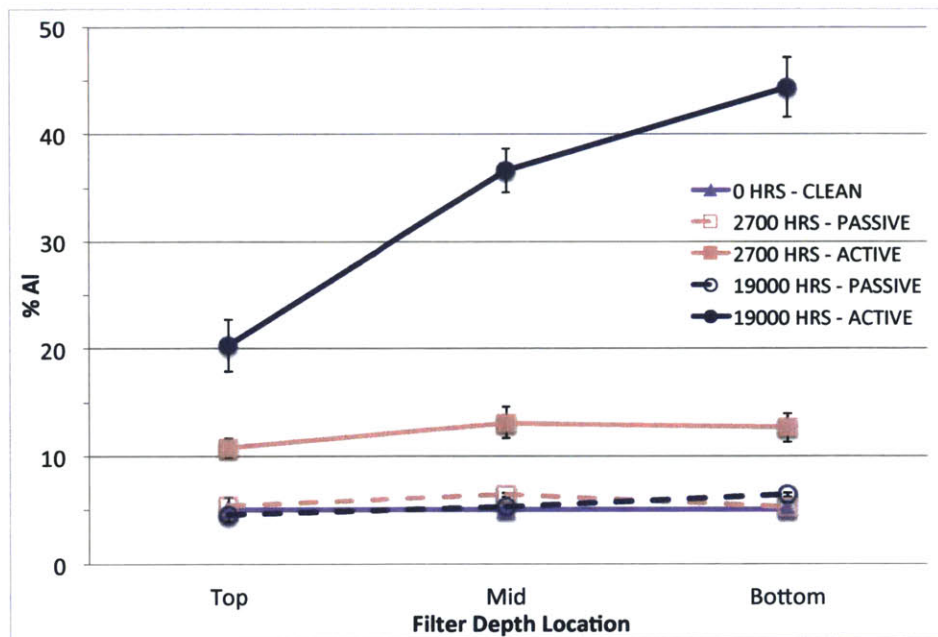


Figure 5.3. % Al vs. Filter Depth Location.

The data shows that the % Al increases as a function of filter depth for the 19000-hr active sample. Also, the % Al increases from the top fibers to the bottom fibers in the 2700-hr active sample, but the % Al between the middle and bottom fibers is essentially the same, with the middle layer containing slightly more Al. The 2700-hr active and 19000-hr active samples contain on average 2.14 and 6.23 times more Al, respectively, than the passive samples. Additionally, both the 2700-hr and 19000-hr passive samples contain 5.70% and 5.42% Al, respectively; very close to the advertised 5% surface composition of Fecralloy. This suggests that that amount of Al generally does not increase in passive samples.

It is important to understand the possible source of the high % Al readings in the active regeneration samples. The increased Al levels in the active filter, especially in the 19000-hr active sample, may potentially be caused by the growth and subsequent detachment of the Al oxide layer from the fiber, an idea put forth in *Section 4.2.2*. Assuming the porosity of the bottom level of the filter is low enough to trap these detached fragments of Al oxide, the % Al would gradually increase in the bottom fibers, as the top and middle fibers shed their oxide coatings. The ESEM study of *Section 5.1* already determined that the fiber growth in the bottom level of the filter is inconsequential, therefore it can be reasonably assumed that the % Al in the bottom fibers of the filter derive from both the 5% Al content of Fecralloy and the additional Al oxide species from upstream fibers.

It is possible that the Al oxide layer in top level of the filter breaks away from the fiber first and becomes trapped in the middle level of the filter. Then the oxide layer of the middle level of the filter breaks away and becomes trapped in the bottom level of the filter. As the filter experiences continuous exhaust conditions, with intermittent regeneration, which stops the flow to a particular cartridge, the Al oxide layer would continue to move from the top level of the filter to the bottom level. So a possible reason why the % Al in the 2700-hr case differs from the 19000-hr case is because the filter cartridge has only run for 2700 hours and 5000 regenerations and has not been in operation long enough for the middle fiber oxide layer to shed and subsequently collapse into the lower filter level. This sequential oxide layer growth and detachment is supported in Figure 5.1, which showed that the top fibers have more growth than the bottom fibers. However, without analyzing filter samples in the intermediate range between 2700 and 19000 hours, it is difficult to make this assessment with quantitative certainty.

An advantage to using EDX to study the % Al in the filter is that it also records the other elements that exist on the fiber and in the adjacent void space. Hence, one experiment can help quantify multiple parameters. As such, the various amounts of Ca and Zn ash that appeared in ESEM images were recorded and subjected to the same statistical procedures that were used for the % Al experiment. This analysis will help determine the extent to which ash reduces the porosity in the filter, and will further enable the differentiation between porosity reductions due

to Al oxide detachment versus ash accumulation. The results of the EDX Ca ash sampling experiment are shown below in Figure 5.4.

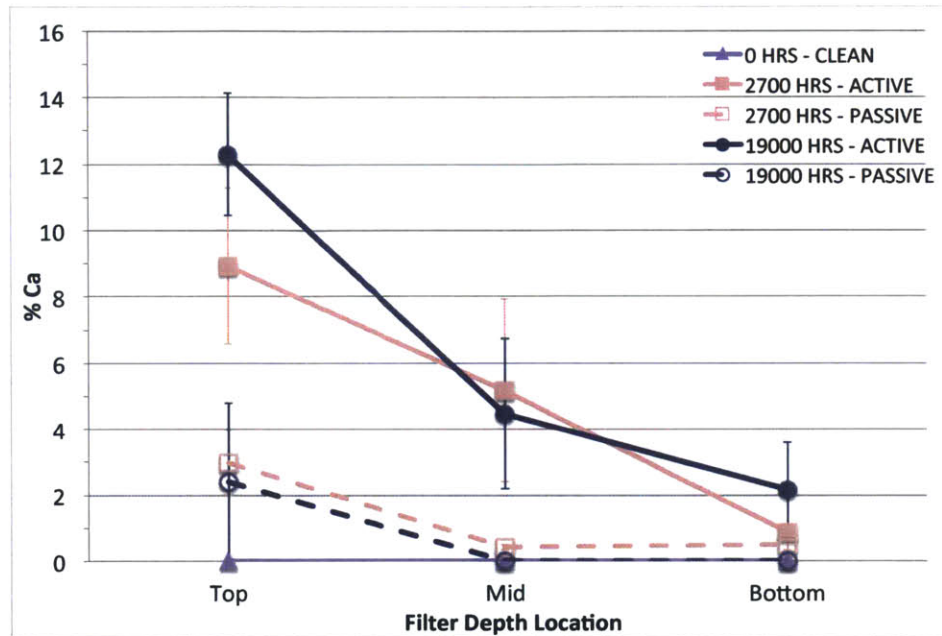


Figure 5.4. % Ca vs. Filter Depth Location.

The data shows that the amount of Ca ash decreases with depth into the filter. The 2700-hr active case has about 10 times more ash in the top layer than in the bottom layer, and the 19000-hr active sample has about 6 times more ash at the top than the bottom. Also, it is evident that the regeneration scheme influences the quantity of ash; the 2700-hr active sample contains approximately 3 times more ash than the passive case in the top fibers, and the 19000-hr active sample has about 5 times more ash in the top fibers. To resolve all of the sources that contribute to a reduction in porosity, the results of the Zn ash analysis are shown below in Figure 5.5:

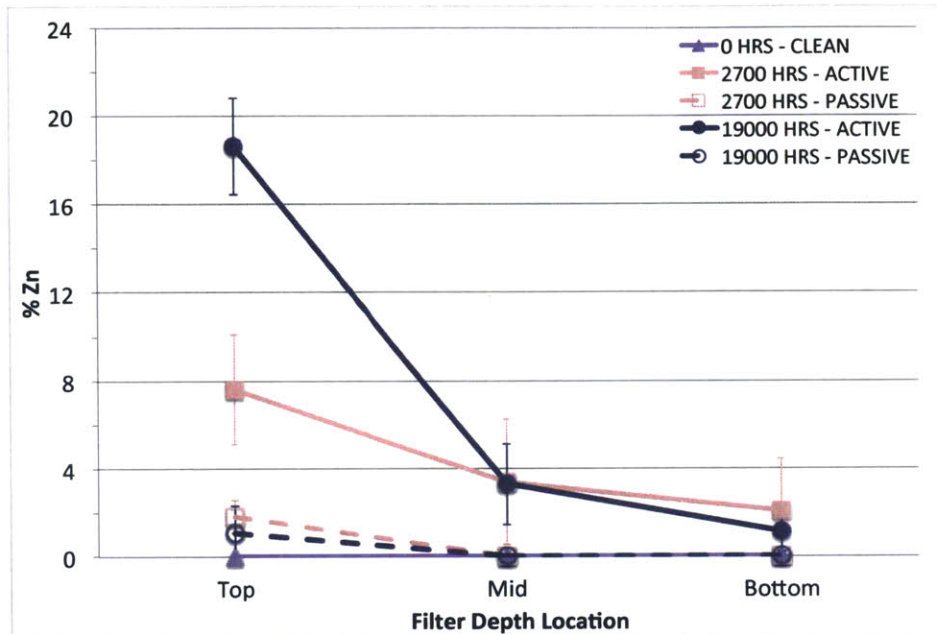


Figure 5.5. % Zn vs. Filter Depth Location.

The results of the Zn ash correspond with the previous Ca ash results; the amount of Zn significantly decreases with depth into the filter. The 2700-hr active sample has 4 times more Zn ash in the top level than in the bottom level, and the 19000-hr active sample contains almost 17 times more Zn in the top than the bottom. This level of ash accumulation in the top fibers was not seen for Ca in the 19000-hr active sample, and may be indicative of preferential filtration, or “stickiness,” of the Zn ash compared to Ca.

The active case has more ash at all levels of the filter than the passive case. What is interesting to note in both the Ca and Zn analyses is that the top layer ash level drastically increases with longer run-time. For instance, the middle and bottom layers of the 2700-hr and 19000-hr samples contain about the same amount of ash, but the top fibers of the 19000-hr sample contain approximately twice as much ash as the 2700-hr sample. Just by visually analyzing Figure 5.5, there seems to be a level at which ash accumulation slows in the middle and bottom levels of the filter, causing more ash to collect on the top fibers. This mechanism is hard to deconstruct by analyzing two samples at run-time extremes, but it seems to support the model depicted in Figure 2.7, whereby ash and soot penetrate the bottom fibers and “fill-up” the filter. To fully explore this concept, though, would require analyzing the initial ash build-up in SMF DPFs at 1 or 2 hours of loading.

Having a thorough understanding of the % Al distribution and Ca and Zn ash accumulation in the filter, it is necessary to discretize the EDX ash results to determine the total number and area of the ash primary particles and agglomerates.

### **5.3 Ash Particle Size and Agglomerate Structure Results**

This study was conducted to help understand the ash particle and agglomerate size and structure as a function of the run-time and regeneration strategy. The initial hypothesis, based on previous research in porous ceramic DPFs, is that active regeneration events causes the agglomerated soot clusters to shrink or collapse during oxidation, bringing ash particles closer together to form larger ash structures [39, 40, 65, 74]. This theory has been widely studied and researched for cordierite DPFs, and explains the evolution of 10-20 nm-range ash precursors into 1-10  $\mu\text{m}$ -range primary particles, which then form larger agglomerates of 10  $\mu\text{m}$  and over [39, 40, 65, 73, 74]. This ash formation process can be seen in Figure 2.3. With more run-time and regenerations it is expected that these ash particles will form into larger, more complex ash structures via high-temperature sintering.

To understand ash formation mechanisms in DPFs, knowledge of the fuels and lube oils used is essential to postulate how ash grows from primary particles into the agglomerates that are easily detected using laboratory instruments such as EDX, XRF, and X-Ray CT. Because limited information is provided on the fuels and lube oils used in the engine operation, only speculation can attempt to resolve any differences between expected and actual ash particle and agglomerate size evolution. The results of the ash primary particle size study are shown below in Figure 5.6:

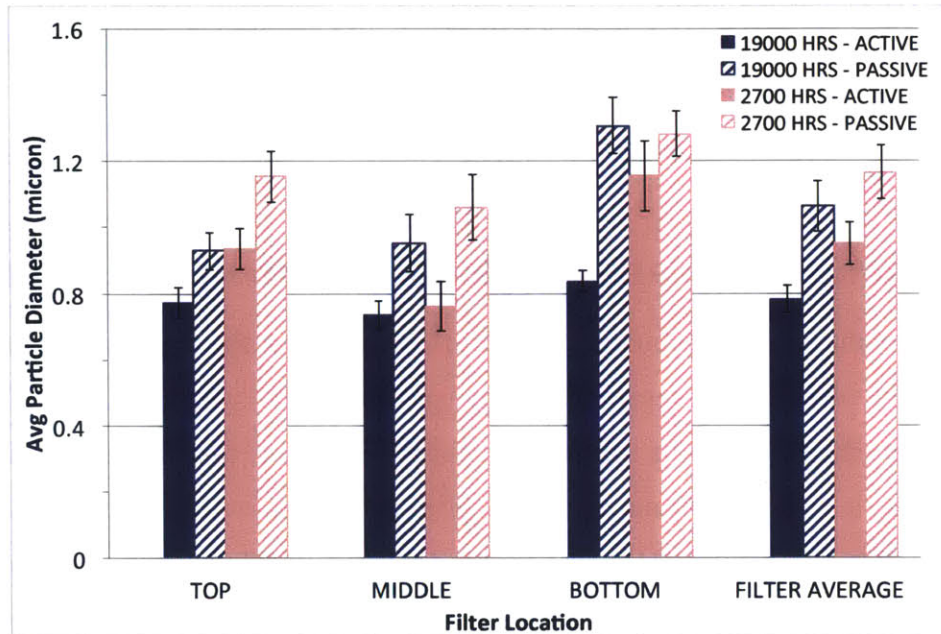


Figure 5.6. Average Ash Particle Diameter vs. Filter Depth Location.

Indeed, the ash particles analyzed are of a micron-scale diameter that corresponds with measured data in literature [73, 74, 75, 76, 77, 78]. This simple fact lends a modicum of credibility to the ImageJ statistical sampling analysis conducted, but the effects of ash sintering are not seen in the results. In both the 2700-hr and 19000-hr active sample, the average primary particle diameter is 0.95  $\mu\text{m}$  and 0.78  $\mu\text{m}$ , respectively. Both of these diameters are smaller than the passive regeneration case of the 2700-hr and 19000-hr sample of 1.16  $\mu\text{m}$  and 1.06  $\mu\text{m}$ , respectively. This opposes the original hypothesis that more regenerations tend to cause ash particles to combine and sinter at high temperatures. However, the fact that the passive particle diameter is consistently larger than active for both the 2700-hr and 19000-hr samples, suggests that the original hypothesis may have been limited in its characterization of the ash formation process.

Using the basis of the original theory that active regeneration induces the collapse of soot particles to agglomerate ash, it is critical to determine the key parameters that contribute most to ash particle size growth. Literature has shown that ash formation and distribution in cordierite filters is not simply a function of the type of regeneration, but rather depends on a subset of variables such as the amount of soot at the beginning of regeneration and the exhaust flow conditions [41]. Applying this principle to SMF DPFs, it is safe to say that these exhaust

conditions such as temperature, molar and volume ratios, and the amount of soot before regeneration can influence ash properties like packing density, porosity, and thus particle size.

The particle size distribution as a function of filter depth reveals that the middle layer of the filter generally contains the smallest sized ash particles, and the bottom layer of the filter contains the largest sized particles. If using the original hypothesis that high temperature sintering creates larger ash particles, it would seem that the heat of regeneration changes at different layers of the filter, resulting in non-uniform particle sizes. However, as described above, there are multiple sub-parameters that influence regeneration and thus particle size. Without knowing the various exhaust properties such as temperature and molar ratio, it is difficult to surmise how these parameters may affect particle size.

Another explanation for why the ash particle diameter seems to oppose the standard theory of ash formation may be that the results include “ash-like” materials that have been unaccounted for in the exhaust. If there were larger contaminants, ImageJ analysis would undoubtedly count them as ash particles, increasing the average particle size. It is unclear what fuel the electrical power generator used, but the salt mining vehicle used a 50% biodiesel fuel blend, which could possibly introduce other “ash-like” particles into the filter.

Transesterification is the process used to convert natural oils from animals or plants into fatty acids, which react with catalysts to form methyl esters, or biodiesel. This process uses different catalysts, one of which being sodium (Na) due to its high reactivity [79]. If compounds containing sodium are being introduced into the SMF DPF in high amounts, they present another “ash-like” material, which would serve to further restrict flow.

Sodium was of minimal interest at the beginning of the study, but a reanalysis of the EDX data from *Section 5.2* shows Na as a recurring element in the scans. The amount of Na captured in each SMF DPF sample is shown below in Figure 5.7:

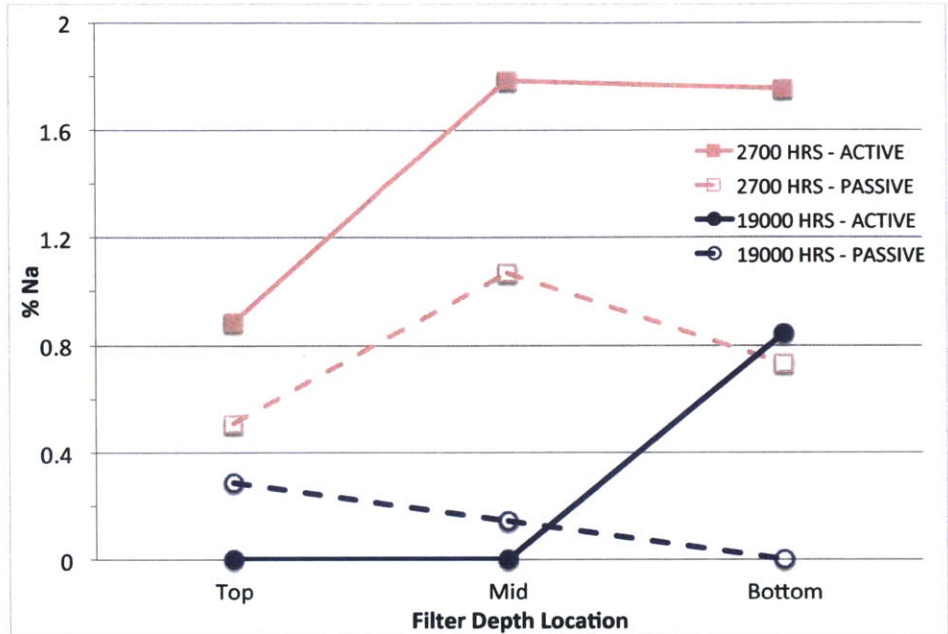


Figure 5.7. % Na vs. Filter Depth Location.

It is clear that Na is an “ash-like” element that is caught in the filter, and it exists in higher amounts in both 2700-hr samples. This may be due to either Na in the biofuel, the salt-mining vehicle’s operating environment, or a combination of both. The source of Na in the 19000-hr sample is unknown, but it is possible that the generator operated on some blend of biodiesel fuel. The effect of Na on influencing the ash particle size is difficult to derive without knowledge of parameters such as soot amount, exhaust temperature, and detailed oil specifications, but the influence of Na on flow restriction may be significant. For instance, the 2700-hr active sample has a relatively high amount of Na in the bottom fibers of the filter, and consequently the average particle diameter is largest in the bottom fibers. This trend between the amount of Na and average particle does not apply for each sample, but it will be objectively analyzed through statistical screening to determine its effects on ash formation and subsequent porosity reductions.

In addition to calculating the average diameter of each ash particle, Image J also reports the total number of particles for each ESEM image analyzed. As explained in *Section 4.2.4*, each ESEM image analyzed is 2000x making the dimensions 62.5  $\mu\text{m}$  x 46.8  $\mu\text{m}$ . This means that the number of particles counted are over a 2925  $\mu\text{m}^2$  area of the SMF DPFs cross section. The number of ash particles for each sample as a function of filter depth location is shown below in Figure 5.8:

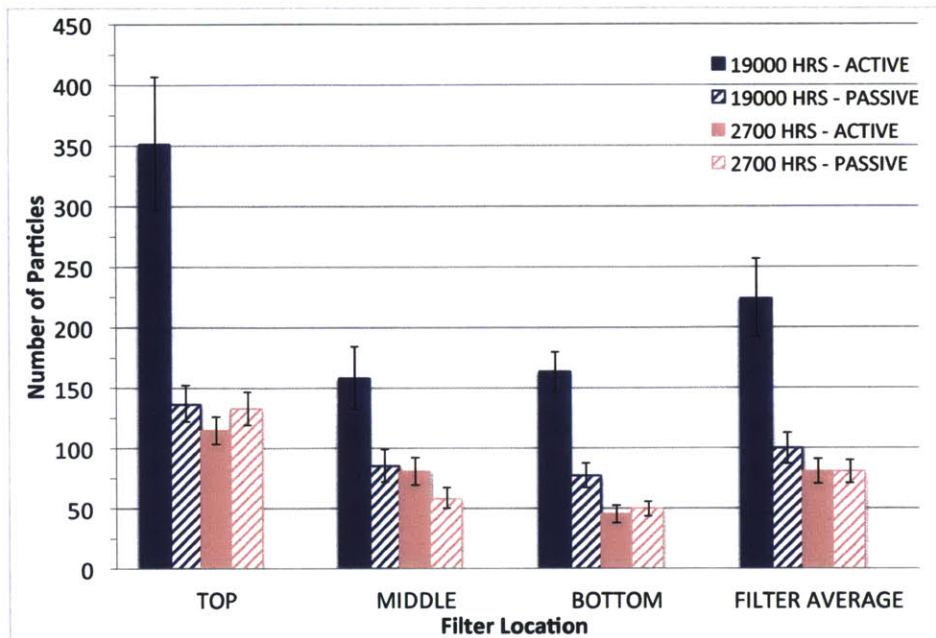


Figure 5.8. # Particles per Standard 2000x ESEM Image vs. Filter Depth Location.

The particle number results clearly show that time and regeneration strategy have a noticeable effect on the number of ash particles within the filter. The 19000-hr active sample contains on average 224 ash particles per 2000x image, with 351 in the top layer alone. This number reduces drastically to approximately 150 ash particles per 2000x image in the middle and bottom levels of the filter, more than a 50% reduction from the top level. This seems to correlate well with the total amounts of Al, Ca, and Zn found in *Section 5.2* using EDX analysis.

There is no evident trend in particle numbers between the 2700-hr active and passive samples, as they fluctuate between their error bars at the top, middle, and bottom levels of the filter. The likely reason for this is due the short run-time compared to the 19000-hr sample. The 2700-hr sample, in a sense, has not reached a steady state, and its ash is still finding open void-space in middle and bottom filter layers. This is an important distinction as it indicates that there is no established cake layer on the filter yet. While it is difficult to make an absolute statement like this without having aged samples of 8000 or 10000 hours, the data supports the filter ash filling mechanism illustrated in Figure 2.7. While a microscopic, particle-by-particle analysis of ash may provide statistically significant evidence of a link between run-time, regeneration, and the amount of ash particles, an ash agglomerate analysis is necessary to corroborate the data sets at a higher order of magnitude.

Ash agglomerates were analyzed using the ImageJ “Analyze Particles” function and setting the area of interest from 20  $\mu\text{m}^2$  to infinity. This setting ignores the ash primary particles, and focuses on larger groupings of ash. The results of the ash agglomerate size study are shown below in Figure 5.9:

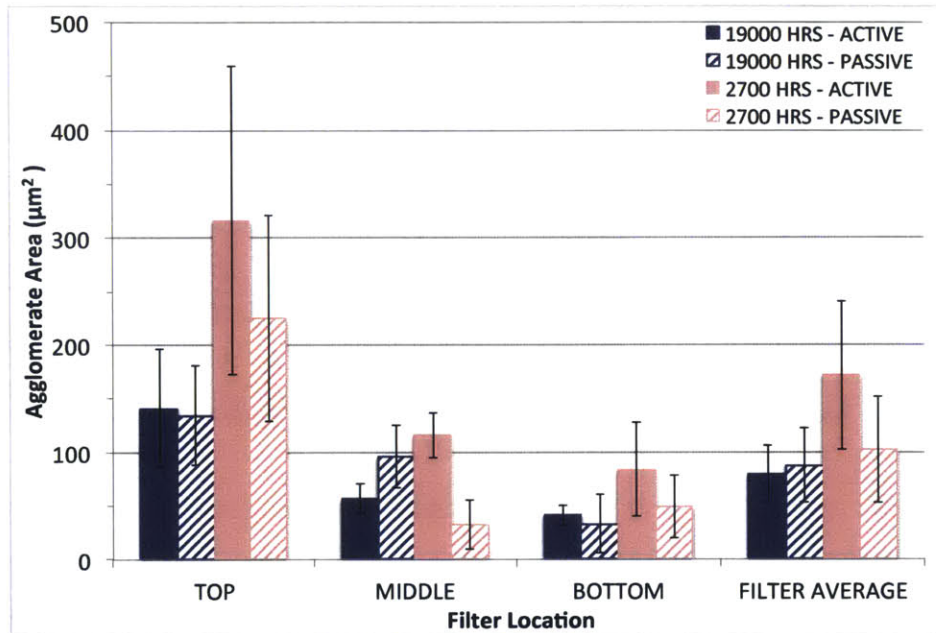


Figure 5.9. Average Agglomerate Area vs. Filter Depth Location.

Based on the variability associated with the average area of agglomerates, it is safe to say that the ImageJ method of analyzing larger ash structures is perhaps not the best metric for quantifying ash. The only significant trend that can be extracted from the data is the relative number of ash agglomerates, which decreases from the top of the filter to the bottom in both samples. Otherwise, there is no visible relationship between the number of agglomerates and run-time or regeneration mode. The likely cause of this error is due to ImageJ not being able to effectively differentiate between ash agglomerates and Al, thereby including Al oxide fragments in the agglomerate area calculation.

The fidelity of this data is also questionable due to the fact that the 3 other studies described above support the hypothesis that the amount of ash is higher in the 19000-hr case than in the 2700-hr case. Regardless, the data will be placed in the regression formula at the end of this section, and if it is truly insignificant a screening experiment will identify it as such.

The ImageJ reports that were generated for the ash agglomerate area also listed the number of agglomerates measured in each ESEM image. The number of ash agglomerates for each sample as a function of filter depth is shown below in Figure 5.10:

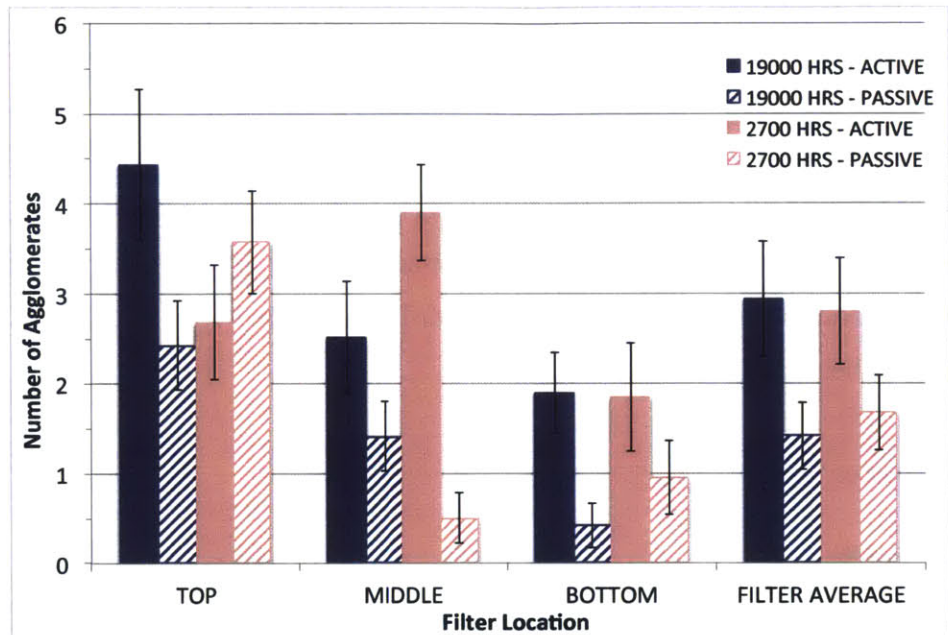


Figure 5.10. # Agglomerates per Standard 2000x ESEM Image vs. Filter Depth Location.

Again, the results show variance in the number of ash agglomerates in each sample, represented by the large error bars. However, the 19000-hr sample in both the active and passive case show the number of ash agglomerates per ESEM image progressively decreasing as a function of filter depth. This trend does not apply for the 2700-hr samples, which follows no visible linear trend between filter levels. The average number of agglomerates in both active cases is almost double the number in the passive cases.

The ash agglomerate size and number study shows the limitations of using post-processing software like ImageJ. There is no effective method to differentiate ash agglomerates from the Al oxide contained within the agglomerates as the gray-scale value for both falls within the limits of thresholding. This results in the ash agglomerate data encompassing both agglomerates and the % Al values previously calculated in *Section 5.2*. Because this data may represent qualitative trends that are difficult to extract by just analyzing the numbers, it will be included in the regression analysis as a possible effect on reducing porosity. However, at this point, it is clear

that another experimental method may more effectively quantify large amounts of ash in the SMF DPF substrate.

## 5.4 Spatial Distribution of Ash Results

A portion of the spatial distribution of ash results has already been presented and analyzed in *Section 5.3*; however, the results represent ash accumulation on a microscopic level. While it is clear that some of the ash distribution data may be flawed, a broader-scale approach to analyzing ash could provide more telling results. The following results consist of 4 SMF DPF coupons of each of the 4 field samples. The samples were scanned for 120 seconds on both the inlet (top layer) and outlet (bottom layer) sides of the filter. The averaged results of the XRF Ca ash analysis are shown below in Figure 5.11:

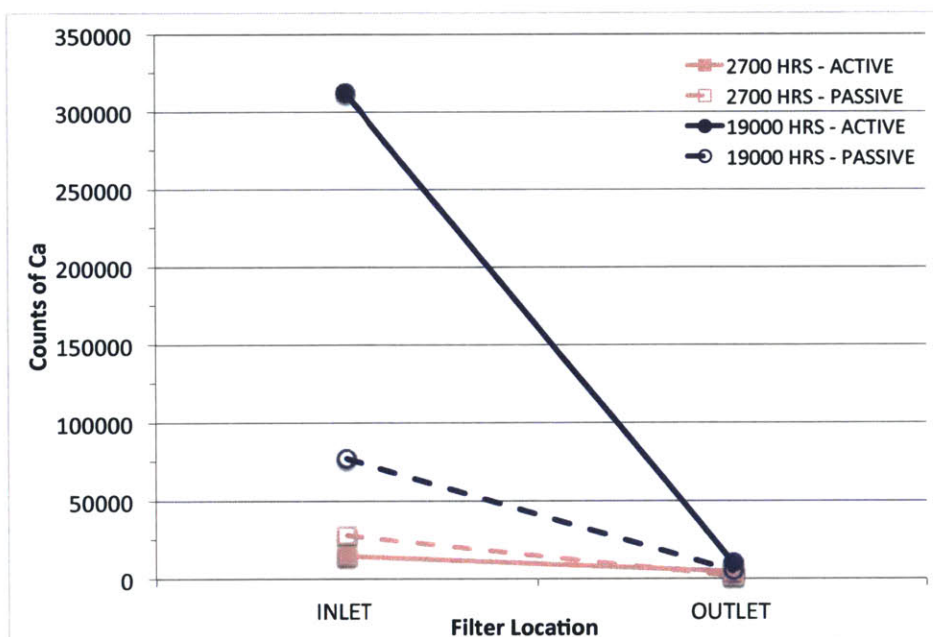


Figure 5.11. XRF Counts of Ca vs. Filter Depth Location.

The XRF analysis Ca data refutes the EDX Ca data to a degree. The EDX analysis of Ca in the filter revealed the 19000-hr active sample to possess the most Ca ash across the filter, followed by the 2700-hr active sample. Although the XRF analysis supports the EDX data for the 19000-hr active case, the 19000-hr passive case contains the second highest amount of Ca ash. Essentially, the EDX analysis presents the amount of Ca ash as a function of regeneration

scheme, while the XRF data shows that the relationship is more between Ca ash and run-time. To see if this trend is similar with other ash elements, the Zn XRF data needs to be analyzed.

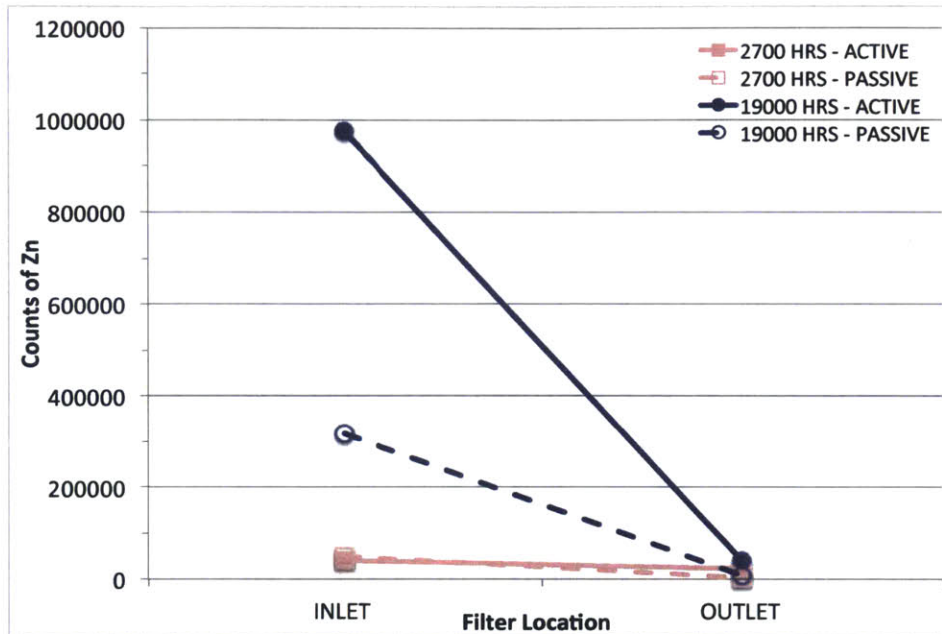


Figure 5.12. XRF Counts of Zn vs. Filter Depth Location.

Again, the XRF data shows a strong relationship between Zn ash and run-time. The 19000-hr active sample contains the most amount of Zn ash overall, with the passive case containing about 3 times less ash in the filter. It is also interesting to note that similar to the Ca analysis above, the Zn analysis shows the 2700-hr passive sample containing more top-layer ash and less bottom-layer ash than the active case. This phenomenon can be seen visually upon examination of the two 2700-hr samples, without any use of advanced instrumentation. The exact cause for this is unknown for now, but a detailed analysis into the statistical trends between all parameters may reveal clues.

Both the Ca and Zn studies also reveal similar reductions in total ash across the filter, independent of run-time or regeneration scheme. With the exception of the 2700-hr active case, the samples show an approximately 94-97% reduction in the total amount of Ca and Zn from the inlet side of the filter to the outlet side. This means that as ash fills in the top layers as has been shown in the previous charts, individual particles are still able to move toward the bottom layer

of the filter over time. The fact that both the 2700-hr case and the 19000-hr case have the same percent reduction in ash is evidence of continuous ash movement between the layers.

But, analyzing all the data so far shows many inconsistencies between respective data sets. It is important to understand the differences in each advanced diagnostic instrument. EDX images ash-fiber interactions on a microscopic scale, which necessitates having to complete a sampling analysis to generate meaningful data. Additionally, EDX is looking at the cross section of the filter, showing the extent of ash depth-penetration, whereas XRF is simply looking at the inlet and outlet side of the samples. To qualify the reliability of the different advanced diagnostic methods used, requires a detailed analysis of the forthcoming statistical model. Before statistical analysis occurs, though, a study of the effects of the previous regressors on filter porosity is necessary.

## **5.5 Porosity and Ash Bridging in SMF Pores Results**

Ash bridging is quantified by determining the porosities of the 4 aged samples and comparing them to the clean sample. 15 porosity core sections are measured at each level in the filter using VG Studio Max post-processing software. It is immensely difficult to accurately isolate the gray-scale values on a histogram pertaining to ash, therefore the isosurface of each sample is made to intersect with the maximum peak shown in Figure 3.11, and the porosities are then relatively determined. This method includes X-Ray noise particles, which are the product of low-resolution analysis and significantly reduce the porosity, but correction factors are applied to the filters to make the porosities more appropriate. The results of the ash bridging study are shown below in Figure 5.13:

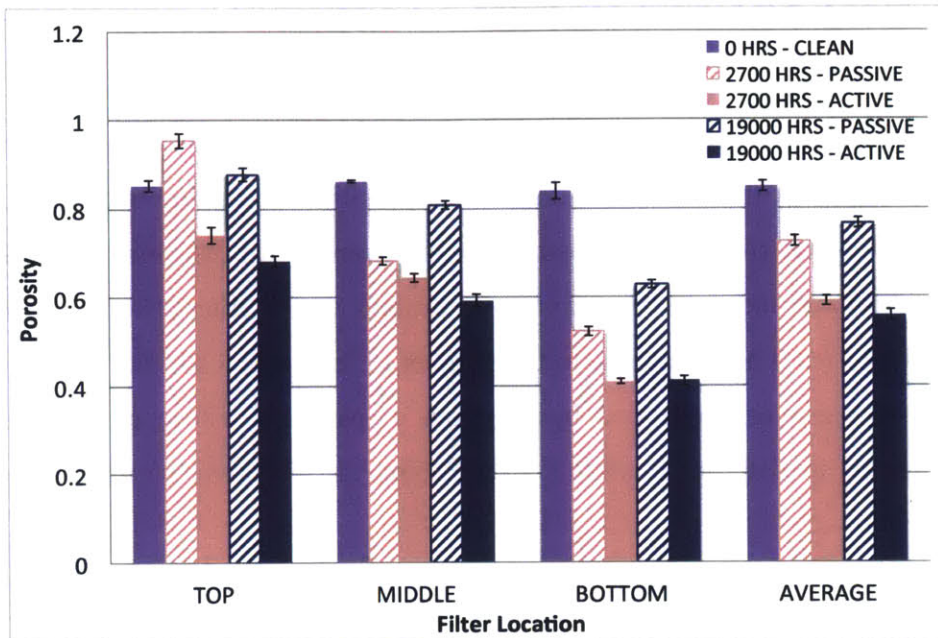


Figure 5.13. Porosity vs. Filter Depth Location.

For all 4 aged samples, the porosity decreases as a function of filter depth. This supports the hypothesis that argues the majority of ash agglomerates stay at the top of the filter, with the possibility of individual particles moving toward the bottom. Also in both cases, active regeneration results in a much larger reduction in porosity at each level of the filter. Knowing from EDX and XRF analysis that ash deposits are less prevalent in the bottom fibers of the filter, a drastically lower porosity in the bottom level of the active filter samples suggests that the high % Al readings may be indicative of filter clogging. The 2700-hr and 19000-hr passive sample's porosities are 72.5% and 76.5%, respectively. This suggests that independent of run-time, a passive sample can expect an approximately 10% reduction in porosity over its lifetime.

The low variability of filter porosities suggests that the method used to quantify porosity is reliable. It is possible to refine this method so that it provides porosity measurement without having to correct it for noise particles, but this time-intensive method requires more work.

Having all of the essential parameters and response variables studied and quantified, a statistical analysis will reveal the importance of each variable with regard to the overall reduction in filter porosity.

## 5.6 Statistical Analysis Results

Ash accumulation in SMF DPFs is such a complicated process with numerous variables having an effect on reducing filter porosity. It is difficult to analyze each individual variable as having an effect on porosity without understanding the possible interaction effects that multiple variables have between each other. For instance, it has been shown that primary particle number increases with run-time and active regeneration throughout the filter. But, the true effect on reducing porosity may not be solely due to the number of ash particles in the filter, rather it may be the number of particles multiplied by the area of particles. These inter-variable effects, though, are difficult to determine without establishing an objective, statistical model of the measured parameters.

The statistical software used to formulate the regression equation is JMP Pro 11. All of the measured parameters are input as regressors, with porosity being the sole response variable. The data-fitting personality used for the model is Standard Least Squares, which attempts to minimize the residuals, or differences between the measured values and model values [71]. Table 5.1 below shows the different measured parameters that are used to generate the regression model.

Response	Regressor
Porosity	Time
	Layer
	Number of Regenerations
	Regeneration Mode
	EDX - % Ca
	EDX - % Zn
	EDX - % Al
	XRF - Calcium
	XRF - Zinc
	Number of Primary Particles
	Number of Agglomerates
	Average Particle Size
	Average Agglomerate Size

Table 5.1. Response and regressor variables for statistical analysis.

The above data cannot be fitted into a multiple regression formula because of the two XRF data points, which do not have any measured values for the middle layers. Therefore, for now, these data points will be removed and the model will be fit again.

When the model is re-run the following output shows the P-values of each parameter. The P-value, shown by the term “Prob > |t|” in Figure 5.14 below, indicates the level at which the null hypothesis,  $H_0$ , can be rejected. For multiple regression equations, the null hypothesis is  $H_0: \beta_1 = \beta_2 = \dots = \beta_k = 0$ , and the alternative hypothesis is  $H_1$ : At least one  $\beta_j \neq 0$  [71]. The  $\beta$  terms describe the partial regression coefficients of each variable, and failure to reject null hypothesis indicates there is no statistical relationship between any of the regressors and the response variable. If the P-value is less than the significance value of the regression, in this case  $\alpha = 0.05$ , then  $H_0$  can be rejected in favor of the alternative hypothesis,  $H_1$ , which shows that at least one of the regressors is statistically significant to the model. Thus, we can accept the model with 95% confidence.

Parameter Estimates				
Term	Estimate	Std Error	t Ratio	Prob> t
Intercept	50.295472	0.674497	74.57	0.0085*
TIME (HRS)	0.0010301	1.762e-5	58.48	0.0109*
LAYER[BOT]	-18.53324	0.116491	-159.1	0.0040*
LAYER[MID]	6.322618	0.10972	57.63	0.0110*
REGENERATION[ACTIVE]	-16.81528	0.452923	-37.13	0.0171*
REGENERATION[NONE]	28.327496	0.674753	41.98	0.0152*
% Ca	-0.021087	0.08586	-0.25	0.8467
% Zn	2.5959443	0.172057	15.09	0.0421*
# PARTICLES	-0.126707	0.009126	-13.88	0.0458*
AGGLOMERATES	5.3105487	0.176676	30.06	0.0212*
AVERAGE PARTICLE SIZE	23.054257	0.81291	28.36	0.0224*
AVG AGGLOM SIZE	0.0222444	0.001547	14.38	0.0442*
# REGEN	-0.005364	0.000178	-30.08	0.0212*
% AL	1.4554063	0.062208	23.40	0.0272*

Figure 5.14. P-values for regression variables.

However, the % Ca parameter shown above has a P-value of 0.8467, which is well above the  $\alpha = 0.05$  level. Referencing the EDX results of % Ca shown in Figure 5.14, this makes sense, as the amount of Ca in the 2700-hr active sample was not much less than the 19000-hr sample. To adjust the model, the % Ca is removed from the regression and re-evaluated. The results of removing % Ca from the model are shown below in Figure 5.15:

<b>Parameter Estimates</b>				
<b>Term</b>	<b>Estimate</b>	<b>Std Error</b>	<b>t Ratio</b>	<b>Prob&gt; t </b>
Intercept	50.25944	0.479358	104.85	<.0001*
TIME (HRS)	0.0010288	1.224e-5	84.06	0.0001*
LAYER[BOT]	-18.52967	0.084155	-220.2	<.0001*
LAYER[MID]	6.3295816	0.077176	82.02	0.0001*
REGENERATION[ACTIVE]	-16.81897	0.329601	-51.03	0.0004*
REGENERATION[NONE]	28.402858	0.437562	64.91	0.0002*
% Zn	2.5660971	0.088684	28.94	0.0012*
# PARTICLES	-0.125503	0.005604	-22.39	0.0020*
AGGLOMERATES	5.2913624	0.115383	45.86	0.0005*
AVERAGE PARTICLE SIZE	23.13897	0.535974	43.17	0.0005*
AVG AGGLOM SIZE	0.022078	0.001013	21.80	0.0021*
# REGEN	-0.005351	0.000123	-43.42	0.0005*
% AL	1.4475403	0.038831	37.28	0.0007*

Figure 5.15. Adjusted P-values after removing % Ca.

As can be seen, each parameter listed above is statistically significant to the model. In fact all parameters are an order of magnitude less than the  $\alpha = 0.05$  significance level. It is probabilistically near impossible for this data to represent a coincidence of measurements, however, to apply another factor of safety, the P-values can be rank ordered to determine which ones have the greatest effect on porosity. The smallest P-values of the parameter estimate that are two orders of magnitude less than the significance level (in increasing order) are: intercept, run-time, layer, regeneration mode, number of agglomerates, particle size, number of regenerations, and % Al. For example, it is evident that all parameters are significant to the effect on porosity, but based on the relative P-values, the run-time is 5 times more significant to porosity than the number of regenerations (0.0001 vs. 0.0005). This data is important in learning which parameters can be manipulated to try and mitigate the effects of porosity reduction in the filter.

The shortcoming in the model is that it does not account for the amount of Ca ash, which has been qualitatively shown in XRF analysis to increase with time. To include the XRF analysis data, it must be assumed that the relative amounts of Ca and Zn ash decrease linearly with depth into the filter. As previously mentioned, XRF data had to be removed from the analysis as it did not contain a middle layer term and thus could not be fit into a model. Including the estimated middle layer terms for ash amount in the filter, returns the XRF Ca ash amount to be the least significant term to the model again, this time with a P-value of 0.8401. Therefore, two independent experimental instruments both indicate that the amount of Ca ash is insignificant to

the overall porosity response variable. For this reason, the parameter estimates listed above in Figure 5.15 will be accepted as the best fit of all of the data. The regression formula of the data is shown below in Equation 5.1 and the summary of fit for the regression formula is shown in Figure 5.16:

$$\begin{aligned}
 \text{Porosity} = \varepsilon = & 50.259 + (0.00103 * \text{Time (hrs)}) + \text{Match [Layer]} \left\{ \begin{array}{l} \text{"BOT"} \rightarrow -18.530 \\ \text{"MID"} \rightarrow 6.330 \\ \text{"TOP"} \rightarrow 12.200 \end{array} \right\} + \\
 & \text{Match [Regen]} \left\{ \begin{array}{l} \text{"ACTIVE"} \rightarrow -16.819 \\ \text{"NONE"} \rightarrow 28.403 \\ \text{"PASSIVE"} \rightarrow -11.584 \end{array} \right\} + (2.567 * \% \text{ Zn}) - (0.126 * \# \text{ Particles}) + \\
 & (23.139 * \text{Avg Particle Diam}) + (5.291 * \# \text{ Agglom}) + (0.0221 * \text{Avg Agglom Area}) - \\
 & (0.00535 * \# \text{ Regens}) + (1.448 * \% \text{ Al}) \qquad \qquad \qquad \text{(Eqn. 5.1)}
 \end{aligned}$$

Summary of Fit				
RSquare				0.999993
RSquare Adj				0.999954
Root Mean Square Error				0.11973
Mean of Response				77.48667
Observations (or Sum Wgts)				15

Analysis of Variance				
Source	DF	Sum of Squares	Mean Square	F Ratio
Model	12	4332.0887	361.007	25183.16
Error	2	0.0287	0.014	<b>Prob &gt; F</b>
C. Total	14	4332.1173		<.0001*

Figure 5.16. Summary of Fit and ANOVA of statistical model.

Although the above regression formula represents a first attempt at quantifying the individual contributions of each parameter to reducing porosity in SMF DPFs, more work still needs to be done to refine the model. Intermediate aged samples of 8000 to 10000 hours would help create a smoother transition between data points, instead of relying on two extreme times. Also, additional investigation needs to be done with regard to the other variables. For example, % Zn was used as a regressor in the model, but it can be studied as a response variable as well, with the amount of Zn ash likely depending on time, regeneration, and filter layer. Lastly, the regression formula includes the ash agglomerate area data, which was subject to high variability. This

variability is likely due to the high-magnification scans not depicting the true amounts of ash agglomerates in the filter. More work is needed to identify and more accurately quantify how ash contributes to a reduction in porosity.

The preceding results show how certain variables contribute to changing the porosity in SMF DPFs. Through statistical analysis, it has been shown that there are many variables that help influence the porosity of the filter, some more than others. Using this information in tandem with the results generated for each study, conclusions and recommendations can be made that will help mitigate the effects of porosity reduction in SMF DPFs and will help hone in on future research efforts to solve this problem.

## **6 CONCLUSIONS AND RECOMMENDATIONS**

There were two motivations behind this work: (1) to develop a standard and repeatable advanced diagnostic approach to researching ash and substrate properties in SMF DPFs, and (2) to determine how the ash and substrate properties affect the filter performance, specifically porosity reduction, in SMF DPFs. The ultimate goal of this research was to help establish knowledge with regard to the general effects of ash on SMF DPFs, in hopes of optimizing the design and use of the system.

The research was an enumerative analysis, relying on statistical sampling principles to make conclusions about SMF DPFs. The 4 samples studied were field specimens aged at 2700 and 19000 hours, in both the active and passive regeneration schemes. These samples were then compared to the baseline clean sample to draw qualitative conclusions about the nature of porosity reduction in SMF DPFs. Although more research is needed to fully understand the interaction between ash and the substrate across different regeneration modes, various conclusions can be made to elucidate some of the significant findings of the study.

### **6.1 Advanced Diagnostic Methods**

Some of the advanced diagnostic tools generated statistically significant results, which supported the hypotheses, whereas other instruments did not yield any pertinent information. Specifically, the EDX analysis showed no trends in the amount of Ca ash in the filter as a function of the run-time when XRF did. The EDX analysis was a high magnification study, which consequently identified pockets of ash instead of quantifying the broader distribution of ash. Future EDX analyses of the relative amounts of filter ash should be conducted at a lower magnification, such as 100x – 200x, instead of 800x. This setting would show the general trends of ash deposition in SMF DPFs, and possibly be more comparable to XRF results.

ImageJ analysis was used to determine the size and number of primary particles and agglomerates in SMF DPFs. With similarities between expected and measured ash particle sizes, it is evident that a post-mortem attempt at quantifying primary particles is possible. However, it

is very difficult to make conclusions about the ash formation process without having data on the specific exhaust conditions the samples were subject to. Although the particles analyzed were not truly “primary particles,” but rather small clusters and agglomerates of particles, ImageJ still provided statistical trends relating particle size to run-time and regeneration. However, this tool was not very useful for examining agglomerates, as there was excessive variance in the measurements. Agglomerates are of more interest when understanding the global effects of how ash restricts flow in an SMF DPF, because they simply occupy more filter space. To provide more accurate agglomerate data, a smaller magnification level like 100x-200x, instead of 2000x should be used.

The FIB ended up not being utilized in understanding the ash-fiber interface, however, the main principles have been outlined and will provide future researchers with a basic understanding of the tool [65]. The main reason for this is due to the long sputtering times necessary to mill through the metallic fiber and ash cross section. It would not have been practical to conduct an analysis of  $n = 40$  samples for each layer of the filter for each aged sample. That is not to say that this tool should not be used in future studies, though. Studying the ash-fiber interface is essential to understanding how ash adheres to the metallic fibers of the filter [65]. This research has provided a scope for future FIB research, that is, it outlined basic principles of ash deposition mechanisms in the filter. It is evident that the active regeneration case exposes the ash and fibers to high temperatures, which likely causes the ash to permanently sinter to the fiber, as Figure 3.8 illustrates. Conversely, the passive case is not subject to nearly as high temperatures, so the ash likely rests on top of the fiber, instead of becoming affixed to it. It is the task of future research to help develop this theory by understanding how the various ash-fiber interface affects filter properties like electrical conductivity and regeneration.

XRF was a tool discovered later in the research, which provided fast and valid results of ash amounts in each filter. The difficulty with including the XRF data in the research was its failure to include middle layer ash deposits, as only the inlet and outlet sides were examined. It would be too difficult and time-consuming to try and cut the filter cross section in half to scan the middle portion for ash amounts, so more work is needed to relate the amounts of ash found in EDX scans to the quantities found in XRF. Once a strong correlation is developed between

percent by weight of ash and the number of X-Ray counts of ash taken under the same XRF settings, then it will be possible to fully understand the ash deposition characteristics in the middle layer of the filter.

X-Ray CT and VG Studio Max represent the future of this research. The capabilities of both tools can help answer many of the questions that the other advanced diagnostic techniques cannot. With additional development, VG Studio Max should be able to accurately identify each ash particle, agglomerate, and fiber oxide layer deposit, in addition to providing the resultant porosity at each level in the filter. This method will save time and experimental cost immensely, while providing more accurate results. To do this, more emphasis has to be placed on scanning individual volumes of soot, ash, and aluminum oxide at identical X-Ray settings to properly threshold the SMF DPF histogram. When this method is fully developed, it will provide quantitative, absolute data on many ash and filter properties, and will help focus future SMF DPF research efforts.

## **6.2 Summary of Results**

In determining the effect of regeneration mode on increasing the fiber diameter, two different tools were used: the Ruler function on ESEM and the Wall Thickness Module of VG Studio Max. While the data collected provided no consistent trend in fiber diameter growth as a function of regeneration scheme, the variability of fiber diameter was consistently lowest in the outlet side of the filter. Additionally, the porosity was the lowest in each sample at the outlet side of the filter. Having more control over the diameter of the fiber at each level in the filter may help to distribute the effects of porosity reduction across all layers of the filter, instead of compounding them downstream at the outlet level. Thus, in the inlet and middle layers where there is still a relatively higher porosity, the fiber diameter could be altered to ensure a more uniform ash distribution. This would possibly cause the average filter porosity to increase, which would reduce flow restriction and pressure drop.

Active regeneration in SMF DPFs consists of stopping exhaust flow to a specific filter cartridge, and heating the cartridge through electrical conduction to oxidize the dormant soot. This process also promotes scaling of the aluminum oxide layer of the fiber, and in some cases can detach the

aluminum oxide layer from the fiber. The amount of aluminum at each level in the filter is measured using EDX, which gives the percent by weight of each element in the ESEM image. Qualitative analyses of the active regeneration samples (Figure 4.2) has indicated that oxide layer separation does occur in active samples, with the aluminum oxide becoming caught downstream in the lower levels of the filter.

The migration of Al is negligible when comparing the clean sample to both the 2700-hr passive and 19000-hr passive sample. This suggests that the lower exhaust temperature in the passive regeneration case causes no significant Al oxide growth or detachment. The % Al increased by 244% in the 2700-hr active sample (5000 regenerations) from the clean sample. The % Al increased by 675% in the 19000-hr active sample (12000+ regenerations) from the clean sample. Therefore, the % Al found in SMF DPFs depends on the run-time, regeneration mode, and number of regenerations. Additionally, the amount of Al increases as a function of depth into the filter in the 19000-hr active sample. The outlet side of the 19000-hr active sample contains 219% more Al than the inlet side. In attempting to reduce the pressure drop across the filter, the mechanisms of regeneration are just as significant as the amount of ash.

Without knowing specific exhaust conditions like molar ratio and temperature, it is difficult to make definitive statements relating the primary particle size to the age of the filter. The individual ash particle diameter is 21% larger in the 2700-hr active case than the 19000-hr active case. The individual ash particle diameter in the 2700-hr passive case is 11% larger than the 19000-hr passive sample. This data was collected from historical, field-aged samples, without knowing the operational characteristics. Consequently, studying ash particle size and evolution as a function of filter aging and soot oxidation is difficult with a post-mortem analysis, but not impossible. With more field data such as the specific fuel and lube oil used, as well as details on the frequency and timing of regeneration, it will be easier to determine possible reasons for particle size differences between samples. Once the mechanisms of ash particle formation are understood, they can be manipulated through engine operations like regeneration, to decrease the overall effects of ash and filter porosity and pressure drop.

The mechanics of ash particle growth and formation throughout the life of the filter, ultimately lead to the creation of ash agglomerates that significantly reduce the porosity of the filter. These ash agglomerates were measured using ImageJ post-processing software as well as XRF. The ImageJ results may have included Al oxide fragments, which would not effectively isolate the individual contributions of ash to reducing porosity. However, there is a consistent decrease in the average agglomerate area as a function of depth into the filter for each sample. Additionally, the 2700-hr active sample has on average 68% larger agglomerates than the passive sample, and approximately 116% larger agglomerates than the 19000-hr active sample. The average number of agglomerates is essentially the same when comparing active samples versus passive samples. It is likely that again the 2000x magnification was too high on the ESEM to accurately shows trends in the ash agglomerate size and number. Future analyses should be conducted at lower magnification, or rely entirely on XRF to generate agglomerate data.

XRF operates on a broader scale of magnification and is better suited for the analysis of general trends in ash deposits in SMF DPFs. The XRF data shows for both Ca and Zn, the two main constituent elements in lubricant-derived ash, that run-time and the regeneration strategy influence the amount of ash in the filter. In the 19000-hr active sample there is 30 times more Ca ash in the inlet fibers than in the outlet fibers, and in the 19000-hr passive sample that number reduces to approximately 15. There is 139 times more Zn ash in the inlet side of the 19000-hr active sample than the outlet side, and about 45 times more for the 19000-hr passive sample. This data corresponds well with Figure 5.5, which shows the “stickiness” of Zn ash and its proclivity for remaining on the top, inlet fibers of the filter. Although SMF DPFs primarily operate in the depth filtration regime, it may be possible to use this preferential filtration mechanism of Zn ash to form a partial cake layer at the filter inlet. This could act as an additional filtration device, and possibly mitigate the downstream flow restriction in SMF DPFs.

The motivation behind studying the aforementioned ash and substrate parameters is to determine how they individually contribute to reducing porosity in SMF DPFs. As such, porosity is the most critical variable to understand because it has a direct effect on filter performance. In all 4 aged samples, the porosity decreases with depth into the filter. The average porosity for the 2700-hr and 19000-hr passive samples is 71.4% and 76.5%, respectively. The average porosity

for the 2700-hr and 19000-hr active samples is 59.2% and 55.7%, respectively. It has been shown that the aluminum content in active samples is greater than passive samples. Therefore, the scaling and detachment of the oxide layer in active SMF DPFs contributes a significant amount to the reduction in porosity.

Also, It is important to note how drastic the reductions in porosity are for the 2700-hr samples compared to the 19000-hr samples. Although they have not been loaded nearly as much as the 19000-hr samples, they have significant reductions in porosity. It is possible that this is due to the differences in drive cycle between a stationary power source and a vehicle. Whereas a generator typically remains constantly loaded, a mining vehicle has a very irregular load cycle and is possibly introducing more PM into the filter. Again, being able to generate a partial cake layer on the top fibers may help mitigate the effects of ash occupying pore space in the SMF DPF.

A statistical analysis of the parameters reveals that the measured quantities most influential to porosity are: run-time, layer, regeneration mode, number of regenerations, % Al, % Zn, number of particles, average particle diameter, number of agglomerates, and average agglomerate area. Further analysis of the P-values shows that of the statistically significant variables, run-time, layer, regeneration mode, number of agglomerates, average particle diameter, number of regenerations, and percent aluminum are the most significant to porosity. Knowing that the P-value of the active regeneration mode is 0.0004, it can be concluded that the regeneration scheme is more influential on the filter porosity than the number of agglomerates or average particle diameter (P-value = 0.0005). Therefore, active regeneration is one of the most critical aspects of reducing filter porosity. Equation 5.1 above shows that an active sample will have an absolute porosity reduction of 16.819 while a passive sample will have a porosity reduction of 11.584.

The significance of creating parametric models is that it can unveil trends in the data that were not previously seen by analyzing each individual parameter. The benefit of this framework is that in addition to ash properties, substrate properties like fiber diameter can be analyzed to see the effect they have on filter porosity. Essentially, this means that statistical modeling can be used as an objective means to manipulate filter properties, in order to optimize the design and use of the

SMF DPF system. More samples are still needed to refine the basic model shown in Equation 5.1, but eventually the model will be able to incorporate substrate properties that can be changed to increase filter performance.

### **6.3 Recommendations**

Future research should attempt to further understand many of the sub-parameters outlined in this study. It is clear that both ash and fiber degradation have a large effect on reducing porosity and thus increasing pressure drop across the filter. The effects of different electrical regeneration powers and temperatures could be studied on a 20-mm diameter Fecralloy rod placed perpendicular to the exhaust stream of the current ash-loading system. This would hardly affect the flow characteristics of the exhaust stream and could even be studied while the ash-loading system is being used for cordierite DPF loading. The testing apparatus would be relatively easy to construct and would help answer the question of how much the fiber diameter grows during oxidation. Although ESEM had difficulty providing absolute measurements of fiber growth, it would still be used, as oxide layer growth on a larger Fecralloy rod would be more visible and less susceptible to error. This could then be qualified with an optical microscope to determine any discrepancies between data sets.

An external consortium member provided independent CFD analyses of clean SMF DPFs, but the results of those analyses did not come to fruition until later in the research. More emphasis should be placed on SMF DPF flow simulations, especially if an experimental testing apparatus is not to be constructed. By extracting a geometrically accurate finite-element mesh of the SMF DPF through high-resolution X-Ray CT and associated post-processing software, CFD analysis can precisely determine substrate properties such as porosity, permeability, and pressure drop. The experience and body of knowledge surrounding X-Ray CT and analysis software is developing rapidly, and with it comes higher quality filter meshes for CFD simulation. These simulations can quickly and effectively identify certain areas of the SMF DPF that can be improved to help reduce the pressure drop across the filter. An experimental framework that relies on these substantive results allows the researcher to iterate on multiple filter designs to identify the optimal candidates for implementation.

Some work is still required in the porosity calculations for aged samples using VG Studio Max. As this parameter is the direct link to pressure drop, it is essential to keep honing in on higher resolution X-Ray CT scans, as well as better settings for which to threshold the SMF DPFs gray-scale histograms. It is an easy task for clean samples, as the histogram can be adjusted to reflect 85% porosity. Without knowing the exact porosity of aged samples, it is much harder, though. A potential solution to this problem involves developing a sample holder that includes a portion of the filter ash outside of the filter. This means that each sample would effectively have “calibration ash” in its X-Ray scan, which would simplify the gray-scale threshold process, and ensure more reliable porosity measurements.

Lastly, it is imperative to keep instrument settings similar when conducting qualitative analyses. This work has relied on measuring the differences between clean and aged samples and the data would have been skewed if the instrument settings were constantly changing. If future research again depends on enumerative sampling studies in lieu of experimental measurements, statistical analysis should be adopted to best understand the effects of the studied parameters on filter performance. With the analysis of two samples at extreme run-times, the statistical framework provided informative data and trends with regard to ash and substrate properties in SMF DPFs. It is apparent that an analysis of more samples will help refine the model as well as provide more details about how to optimize the use and design of the SMF DPF after-treatment assembly.

## 7 REFERENCES

- [1] Charles River Associates. "Diesel Technology and the American Economy." Rep. no. D02378-00. Diesel Technology Forum, Oct. 2000. Web. 3 Mar. 2015. PDF File. <<http://www.dieselforum.org/files/dmfile/ImpactOnAmericanEconomy.pdf>>.
- [2] Majewski, W. Addy. "Diesel Particulate Filters." *DieselNet Technology Guide*. Ecopoint Inc., 18 Jan. 2013. Web. 11 Mar. 2015. <<https://www.dieselnet.com/tech/dpf.php>>.
- [3] Heywood, John B. *Internal Combustion Engine Fundamentals*. New York: McGraw-Hill, 1988. Print.
- [4] Jääskeläinen, Hannu, and Magdi K. Khair. "Engine Fundamentals." *DieselNet Technology Guide*. Ecopoint Inc., 08 May 2014. Web. 3 Mar. 2015. <[http://www.dieselnet.com/tech/diesel\\_fundamentals.php](http://www.dieselnet.com/tech/diesel_fundamentals.php)>.
- [5] Garthwaite, Josie. "The Two-Stroke Engine, Reconsidered." *MIT Technology Review*, 16 Sept. 2010. Web. 25 Mar. 2015. <<http://www.technologyreview.com/news/420818/the-two-stroke-engine-reconsidered/page/2/>>.
- [6] Çengel, Yunus A., and Michael A. Boles. "The Second Law of Thermodynamics." *Thermodynamics: An Engineering Approach*. 6th ed. Boston: McGraw-Hill Higher Education, 2008. 287-88. Print.
- [7] Jääskeläinen, Hannu, and Magdi K. Khair. "Diesel Engines." *DieselNet Technology Guide*. Ecopoint Inc., 10 December 2013. Web. 3 Mar. 2015. <[https://www.dieselnet.com/tech/diesel\\_engines.php](https://www.dieselnet.com/tech/diesel_engines.php)>.
- [8] "Automobile Emissions: An Overview." *EPA*. United States Environmental Protection Agency, 26 Oct. 2011. Web. 5 Mar. 2015. <[http://www.epa.gov/region5/air/mobile/auto\\_emis.html](http://www.epa.gov/region5/air/mobile/auto_emis.html)>.
- [9] *Material Safety Data Sheet No. 9950: Gasoline, All Grades*. Woodbridge, NJ: Amanda Hess Corporation, 08 Jan 2004. Web. 16 Mar. 2015. PDF File. <[http://www.mcoho.org/services/risk/docs/MSDS\\_for\\_Gasoline.pdf](http://www.mcoho.org/services/risk/docs/MSDS_for_Gasoline.pdf)>.
- [10] *Material Safety Data Sheet No. 102: Diesel Fuels*. n.p.: 3E Company, 25 June 2013. Web. 16 Mar. 2015. PDF File. <[http://www.valero.com/v\\_msds/102%20-%20diesel%20fuels%20rev2.pdf](http://www.valero.com/v_msds/102%20-%20diesel%20fuels%20rev2.pdf)>.
- [11] "Fire Protection Equipment." 46 C.F.R. § 181 (1996). Web. <[www.ecfr.gov](http://www.ecfr.gov)>.
- [12] 42 USC. Sec. 4901 – 4918. 1978. Web. <<http://www.gpo.gov/fdsys/granule/USCODE-2010-title42/USCODE-2010-title42-chap65-sec4901>>.

- [13] "What Are the Six Common Air Pollutants?" *EPA*. United States Environmental Protection Agency, 22 Dec. 2014. Web. 05 Mar. 2015. <<http://www.epa.gov/airquality/urbanair/>>.
- [14] Clean Air Technology Center. *Nitrogen Oxides (NOx), Why and How They Are Controlled*. Tech. no. EPA 456/F-99-006R. Research Triangle Park, NC: Office of Air Quality Planning and Standards, United States Environmental Protection Agency, 1999. Web. 7 Mar. 2015. PDF File. <<http://www.epa.gov/ttn/catc1/dir1/fnoxdoc.pdf>>.
- [15] Xing Qiao, et al. "Research Progress On Control Technology Of Diesel Engine Nox And PM Emissions." *Advanced Materials Research* 1008-1009 (2014): 1016-1021. *Applied Science & Technology Source*. Web. 5 Mar. 2015.
- [16] "Nitrogen Dioxide." *EPA*. United States Environmental Protection Agency, 15 Aug. 2014. Web. 07 Mar. 2015. <<http://www.epa.gov/air/nitrogenoxides/>>.
- [17] "Nitrogen Oxides." *Tox Town*. U.S. National Library of Medicine, 29 Oct. 2014. Web. 05 Mar. 2015. <[http://toxtown.nlm.nih.gov/text\\_version/chemicals.php?id=19](http://toxtown.nlm.nih.gov/text_version/chemicals.php?id=19)>
- [18] Majewski, W.A. "Diesel Particulate Matter." *DieselNet Technology Guide*. Ecopoint Inc., 25 Mar. 2014. Web. 11 Mar. 2015. <<https://www.dieselnet.com/tech/dpm.php>>.
- [19] Majewski, W.A. "Diesel Emission Control." *DieselNet Technology Guide*. Ecopoint Inc., 17 Oct. 2014. Web. 03 May 2015. <[https://www.dieselnet.com/tech/engine\\_control.php](https://www.dieselnet.com/tech/engine_control.php)>.
- [20] Majewski, W.A. "Diesel Filter Regeneration." *DieselNet Technology Guide*. Ecopoint Inc., 09 Nov. 2011. Web. 03 May 2015. <[https://www.dieselnet.com/tech/dpf\\_regen.php](https://www.dieselnet.com/tech/dpf_regen.php)>.
- [21] 42 USC. Sec. 7401 – 7514a. 1977. Web. <<http://uscode.house.gov/browse/prelim@title42/chapter85/subchapter1&edition=prelim>>
- [22] "About the CFR." *National Archives*. National Archives and Records Administration, n.d. Web. 12 Mar. 2015. <<http://www.archives.gov/federal-register/cfr/about.html>>.
- [23] "United States." *DieselNet Emission Standards: United States*. Ecopoint Inc., June 2010. Web. 07 Mar. 2015. <<https://www.dieselnet.com/standards/us/>>.
- [24] "Heavy-duty engines" Defined, 40 C.F.R. § 85.502 (2011). Web. <[www.ecfr.gov](http://www.ecfr.gov)>.
- [25] "Heavy-Duty Onroad Engines." *DieselNet Emission Standards: United States*. Ecopoint Inc., Nov. 2014. Web. 15 Mar. 2015. <<https://www.dieselnet.com/standards/us/hd.php>>.

- [26] Jääskeläinen, Hannu, and W. Addy Majewski. "Engine Design for Low Emissions." *DieselNet Technology Guide*. Ecopoint Inc., 10 Feb. 2015. Web. 24 Mar. 2015. <[https://www.dieselnet.com/tech/engine\\_design.php](https://www.dieselnet.com/tech/engine_design.php)>.
- [27] "Nonroad engine" Defined, 40 CFR § 1068.30 (2008). Web. <[www.ecfr.gov](http://www.ecfr.gov)>.
- [28] "Nonroad Diesel Engines." *DieselNet Emission Standards: United States*. Ecopoint Inc., Apr. 2013. Web. 15 Mar. 2015. <<http://www.dieselnet.com/standards/us/nonroad.php>>.
- [29] "Does this part apply for my engines?" 40 CFR §1039.1 (2006). Web. <[www.ecfr.gov](http://www.ecfr.gov)>.
- [30] "Understanding Emission Regulations." *John Deere*. Deere & Company, 2015. Web. 16 Mar. 2015. <[https://www.deere.com/en\\_US/services\\_and\\_support/engine-information/understanding-emission-regulations/understanding-emission-regulations.page](https://www.deere.com/en_US/services_and_support/engine-information/understanding-emission-regulations/understanding-emission-regulations.page)>
- [31] "Technology - Diesel Retrofit Devices." *EPA*. United States Environmental Protection Agency, 23 Jan. 2013. Web. 10 Mar. 2015. <<http://www.epa.gov/cleandiesel/technologies/retrofits.htm>>.
- [32] Majewski, W. Addy. "Diesel Oxidation Catalyst." *DieselNet Technology Guide*. Ecopoint Inc., 28 May 2012. Web. 10 Mar. 2015. <[http://www.dieselnet.com/tech/cat\\_doc.php](http://www.dieselnet.com/tech/cat_doc.php)>.
- [33] Majewski, W. Addy. "Selective Catalytic Reduction." *DieselNet Technology Guide*. Ecopoint Inc., 19 Jun. 2013. Web. 11 Mar. 2015. <[https://www.dieselnet.com/tech/cat\\_scr.php](https://www.dieselnet.com/tech/cat_scr.php)>.
- [34] Majewski, W. Addy. "SCR Systems for Mobile Engines." *DieselNet Technology Guide*. Ecopoint Inc., 07 May 2013. Web. 24 Mar. 2015. <[https://www.dieselnet.com/tech/cat\\_scr\\_mobile.php](https://www.dieselnet.com/tech/cat_scr_mobile.php)>.
- [35] "Cars and Light-Duty Trucks-Tier 3." *DieselNet Emission Standards: United States*. Ecopoint Inc., Mar. 2014. Web. 11 Mar. 2015. <[https://www.dieselnet.com/standards/us/ld\\_t3.php](https://www.dieselnet.com/standards/us/ld_t3.php)>.
- [36] Majewski, W. Addy. "Diesel Filter Materials." *DieselNet Technology Guide*. Ecopoint Inc., Mar. 2011. Web. 12 Mar. 2015. <[https://www.dieselnet.com/tech/dpf\\_mat.php](https://www.dieselnet.com/tech/dpf_mat.php)>.
- [37] Majewski, W. Addy. "Wall-Flow Monoliths." *DieselNet Technology Guide*. Ecopoint Inc., 26 Oct. 2012. Web. 12 Mar. 2015. <[https://www.dieselnet.com/tech/dpf\\_wall-flow.php](https://www.dieselnet.com/tech/dpf_wall-flow.php)>.
- [38] Sappok, Alexander G. "The Nature Of Lubricant-Derived Ash-Related Emissions And Their Impact On Diesel Aftertreatment System Performance." n.p.: c2009., 2009. *MIT Barton Catalog*. Web. 12 Mar. 2015.

- [39] Sappok, Alexander G. "Ash Accumulation in Diesel Particulate Filters." *DieselNet Technology Guide*. Ecopoint Inc., 28 Jan. 2013. Web. 12 Mar. 2015. <[http://www.dieselnet.com/tech/dpf\\_ash.php](http://www.dieselnet.com/tech/dpf_ash.php)>.
- [40] Sappok, Alexander, and Victor W. Wong. "Lubricant-derived Ash Properties and Their Effects on Diesel Particulate Filter Pressure-Drop Performance." *Journal of Engineering for Gas Turbines and Power*. 133.3 (2011): 32805. Print.
- [41] Sappok, A., Govani, I., Kamp, C., Wang, Y. et al. "In-Situ Optical Analysis of Ash Formation and Transport in Diesel Particulate Filters During Active and Passive DPF Regeneration Processes." Tech. no. SAE 2013-01-0519. n.p.: SAE International, 2013. Web. DOI: 10.4271/2013-01-0519.
- [42] Jääskeläinen, Hannu. "Engine Exhaust Back Pressure." *DieselNet Technology Guide*. Ecopoint Inc., 26 May 2009. Web. 12 Mar. 2015. <[https://www.dieselnet.com/tech/diesel\\_exh\\_pres.php](https://www.dieselnet.com/tech/diesel_exh_pres.php)>.
- [43] Hield, Peter. "The Effect of Back Pressure on the Operation of a Diesel Engine." Rep. no. DSTO- TR-2531. Victoria, Australia: Maritime Platforms Division, 2011. Web. 12 Mar. 2015. PDF File. <<http://www.dtic.mil/dtic/tr/fulltext/u2/a542327.pdf>>.
- [44] Whitaker, Stephen. "Flow in Porous Media I: A Theoretical Derivation of Darcy's Law." *Springer*. Kluwer Academic Publishers, n.d. Web. 16 Mar. 2015. PDF File. <[http://link.springer.com/article/10.1007%2F978-1-4020-2848-2\\_1](http://link.springer.com/article/10.1007%2F978-1-4020-2848-2_1)>.
- [45] Harris, Gary L. "1: Basic Physical Properties." *Properties of Silicon Carbide*. London: Institution of Engineering and Technology, 1995. 2-3. *Knovel*. Web. 28 Apr. 2015.
- [46] "Fecralloy® - Iron/Chromium (Fe72.8/Cr22/Al 5/Y 0.1/Zr 0.1): Material Information." *GoodFellow*. GoodFellow, 2015 Web. 16 Mar. 2015. <<http://www.goodfellow.com/E/Fecralloy-Iron-Chromium.html>>.
- [47] Kamp, C., Folino, P., Wang, Y., Sappok, A. et al. "Ash Accumulation and Impact on Sintered Metal Fiber Diesel Particulate Filters." Tech. no. SAE 2015-01-1012. n.p.: SAE International, 2015. Web. DOI: 10.4271/2015-01-1012.
- [48] "Active Diesel Emissions Control Systems: Overview Summary." Rypos, Inc., 2010. Web. 20 Mar 2015. PDF File. <<http://www.arb.ca.gov/diesel/showcase/files/products/9-rypos-hdpf-c.pdf>>
- [49] DePetrillo, F., et al. "Rypos Trap Active Diesel Particulate Filter System: Field Demonstration", US DOE, 8th Diesel Emissions Reduction Conference (DEER), San Diego, CA, August 2002. Web. 15 Mar. 2015. PDF File. <[http://www.eere.energy.gov/vehiclesandfuels/pdfs/deer\\_2002/session11/2002\\_deer\\_depetrillo1.pdf](http://www.eere.energy.gov/vehiclesandfuels/pdfs/deer_2002/session11/2002_deer_depetrillo1.pdf)>.

- [50] D. Thomas, et al. "Clogging of fibrous filters by solid aerosol particles: Experimental and modeling study." *Chemical Engineering Science* 56 (2001): 3549-3561. *ScienceDirect*. Web. 03 May 2015.
- [51] Nabovati, A, E. Llewellyn, and A. Sousa. "A General Model For The Permeability Of Fibrous Porous Media Based On Fluid Flow Simulations Using The Lattice Boltzmann Method." *Composites Part A* 40 (2009): 860-869. *ScienceDirect*. Web. 23 Apr. 2015.
- [52] Yazdchi, K., S. Srivastava, and S. Luding. "Microstructural Effects On The Permeability Of Periodic Fibrous Porous Media." *International Journal Of Multiphase Flow* 37 (2011): 956-966. *ScienceDirect*. Web. 23 Apr. 2015.
- [53] Swapp, Susan. "Scanning Electron Microscopy (SEM)." *Integrating Research and Education*. Science Education Research Center, 14 Dec. 2013. Web. 22 Feb. 2015. <[http://serc.carleton.edu/research\\_education/geochemsheets/techniques/SEM.html](http://serc.carleton.edu/research_education/geochemsheets/techniques/SEM.html)>.
- [54] "Scanning Electron Microscopy (SEM)." *Materials Evaluation and Engineering, Inc.*, Materials Evaluation and Engineering, Inc. 2014. Web. 03 May 2015. <<http://www.mee-inc.com/hamm/scanning-electron-microscopy-sem/>>.
- [55] Fu-Yun, Zhu, et al. "3D Nanostructure Reconstruction Based On The SEM Imaging Principle, And Applications." *Nanotechnology* 25.18 (2014): 185705. *Inspec*. Web. 22 Feb. 2015.
- [56] "Electron Microscopy." *CMSE*. MIT Center for Materials Science and Engineering, n.d. Web. 25 Mar. 2015. <<http://web.mit.edu/cmse/facilities/electron.shtml#>>.
- [57] "Generating an Image." *Australian Microscopy & Microanalysis Research Facility*. Office for Learning and Teaching, 12 May 2014. Web. 22 Feb. 2015. <<http://www.ammrf.org.au/myscope/sem/practice/principles/imagegeneration.php>>.
- [58] "Basic Procedures for the Environmental Scanning Electron Microscope." *Prism*. MIT Center for Materials Science and Engineering, 24 Sep. 2008. Web. 28 Mar. 2015. <<http://prism.mit.edu/xl30/operating/instruction2.html#1>>.
- [59] Hafner, Bob. "Scanning Electron Microscopy Primer." Characterization Facility, University of Minnesota - Twin Cities, 16 Apr. 2007. Web. 28 Mar. 2015. PDF File. <[http://www.charfac.umn.edu/sem\\_primer.pdf](http://www.charfac.umn.edu/sem_primer.pdf)>.
- [60] Goldstein, Joseph I., et al. *Scanning Electron Microscopy And X-Ray Microanalysis*. Boston: Springer US, 2003. *MIT Barton Catalog*. Web. 22 Feb. 2015.
- [61] Hafner, Bob. *Energy Dispersive Spectroscopy on the SEM: A Primer*. Characterization Facility, University of Minnesota - Twin Cities. n.d. Web. 28 Mar. 2015. PDF File. <[http://www.charfac.umn.edu/instruments/eds\\_on\\_sem\\_primer.pdf](http://www.charfac.umn.edu/instruments/eds_on_sem_primer.pdf)>

- [62] EDAX, Inc. "Help Menu: Texture and Elemental Analytical Microscopy (TEAM) Version 4.1" 23 April 2015.
- [63] "Comparison between EDXRF and WDXRF." *Horiba Scientific*. Horiba, Ltd., 2015. Web. 16 Apr. 2015. <<http://www.horiba.com/scientific/products/x-ray-fluorescence-analysis/tutorial/comparison-between-edxrf-and-wdxrf/>>.
- [64] Speakman, Scott. "Using The Bruker Tracer III-SD Handheld X-Ray Fluorescence Spectrometer Using PC Software For Data Collection." *Prism*. MIT Center for Materials Science and Engineering, n.d. Web. 17 Apr. 2015. PDF File. <<http://prism.mit.edu/xray/oldsite/Bruker%20XRF%20SOP.pdf>>
- [65] Kamp, C., Sappok, A., and Wong, V. "Soot and Ash Deposition Characteristics at the Catalyst-Substrate Interface and Intra-Layer Interactions in Aged Diesel Particulate Filters Illustrated using Focused Ion Beam (FIB) Milling." Tech. no. SAE 2012-01-0836. n.p.: SAE International, 2012. Web. DOI: 10.4271/2012-01-0836.
- [66] "Focused Ion Beam Technology, Capabilities And Applications." *KTH Section for Nanostructure Physics*. n.p., n.d. Web. 28 Mar. 2015. PDF File. <<http://www.nanophys.kth.se/nanophys/facilities/nfl/fei-nova200/FejFIB1.pdf>>
- [67] Kosar, T. Fettah. *X-ray MicroCT - Training Presentation*. Cambridge, MA: Center for Nanoscale Systems - Harvard University, 19 Mar. 2013. PPT File.
- [68] "3D Computed Tomography (Cone beam)." *Phoenix|X-Ray*. GE Measurement and Control, n.d. Web. 01 Apr. 2015. <[http://www.phoenix-xray.com/en/company/technology/principles\\_of\\_operation/principle\\_060.html](http://www.phoenix-xray.com/en/company/technology/principles_of_operation/principle_060.html)>.
- [69] Ketcham, R.A., and W.D. Carlson. "Acquisition, Optimization And Interpretation Of X-Ray Computed Tomographic Imagery: Applications To The Geosciences." *Computers & Geosciences* 27.3D (2001): 381-400. *ScienceDirect*. Web. 16 Apr. 2015.
- [70] *VG Studio Max 2.2 Reference Manual*. Germany: Volume Graphics GmbH, May 2012. PDF File.
- [71] Montgomery, Douglas C., George C. Runger, and Norma Faris Hubele. *Engineering Statistics*. 5th ed. Hoboken, NJ: John Wiley, 2011. Print.
- [72] Ferreira, Tiago, and Wayne Rasband. "ImageJ User Guide." National Institutes of Health, 02 Oct. 2012. Web. 05 Apr. 2015. <<http://rsbweb.nih.gov/ij/docs/guide/>>.
- [73] Konstandopoulos, A., Kostoglou, M., Skaperdas, E., Papaioannou, E. et al. "Fundamental Studies of Diesel Particulate Filters: Transient Loading, Regeneration and Aging," Tech no. 2000-01-1016. n.p.: SAE International, 2000. Web. DOI:10.4271/2000-01-1016.

- [74] Merkel, A., Cutter, W., and Warren, C. "Thermal Durability of Wall-Flow Ceramic Diesel Particulate Filters." Tech. no. SAE 2001-01-0190. n.p.: SAE International, 2001. Web. DOI: 10.4271/2001-01-0190.
- [75] Young, D., Hickman, D., Bhatia, G., and Gunasekaran, N. "Ash Storage Concept for Diesel Particulate Filters." Tech. no. SAE 2004-01-0948. n.p.: SAE International, 2004. Web. DOI: 10.4271/2004-01-0948.
- [76] Manufacturers of Emission Controls Association (MECA). "Diesel Particulate Filter Maintenance: Current Practices and Experience." Washington, DC: n.p., June 2005. Web. PDF File.  
<[http://www.meca.org/galleries/files/filter\\_maintenance\\_white\\_paper\\_605\\_final.pdf](http://www.meca.org/galleries/files/filter_maintenance_white_paper_605_final.pdf)>.
- [77] McGeehan, J., Yeh, S., Couch, M., Hinz, A., Otterholm, B., Walker, A., and Blakeman, P. "On the Road to 2010 Emissions: Field Test Results and Analysis with DPF-SCR System and Ultra-Low-Sulfur Diesel Fuel." Tech. no. SAE 2005-01-3716. n.p.: SAE International, 2005. Web. DOI: 10.4271/2005-01-3716.
- [78] Konstandopoulos, A., Zarvalis, D., Kladopoulou, E., and Dolios, I. "A Multi-Reactor Assembly for Screening of Diesel Particulate Filters." Tech. no. SAE 2006-01-0874. n.p.: SAE International, 2006. Web. DOI:10.4271/2006-01-0874.
- [79] Liu, M., S. Niu, and C. Lu. "The Study On The Transesterification Catalyzed By Sodium Compound Loaded On Carbide Slag." *Applied Mechanics & Materials* 733 (2015): 195-198. *Applied Science & Technology Source*. Web. 3 May 2015.